NASA Technical Paper 3478

Navier-Stokes, Flight, and Wind Tunnel Flow Analysis for the F/A-18 Aircraft

Farhad Ghaffari
Langley Research Center • Hampton, Virginia

National Aeronautics and Space Administration
Langley Research Center • Hampton, Virginia 23681-0001

December 1994

The use of trademarks or names of manufacturers in this report is for accurate reporting and does not constitute an official endorsement, either expressed or implied, of such products or manufacturers by the National Aeronautics and Space Administration.

Acknowledgments

Robert M. Hall of the Langley Research Center assisted with the wind tunnel testing of the F/A-18 aircraft configuration. James M. Luckring and James L. Thomas of the Langley Research Center, Robert T. Biedron of Analytical Services and Materials, Inc., David F. Fisher of the Dryden Flight Research Center, and Brent L. Bates of ViGYAN, Inc., contributed to various aspects of this investigation.

This publication is available from the following sources:

NASA Center for AeroSpace Information
800 Elkridge Landing Road
Linthicum Heights, MD 21090-2934
(301) 621-0390

National Technical Information Service (NTIS)
5285 Port Royal Road
Springfield, VA 22161-2171
(703) 487-4650

Contents

Summary

Computational analysis of flow over the F/A-18 aircraft is presented along with complementary data from both flight and wind tunnel experiments. The computational results are based on the three-dimensional thin-layer Navier-Stokes formulation and are obtained from an accurate numerical model of the fuselage, the leading-edge extension (LEX), and the wing geometry. However, the constraints imposed by the flow solver and/or the complexity associated with the flow-field grid generation required certain geometrical approximations to be implemented in the present numerical model. In particular, such constraints from the flow solver inspired the blocking (fairing) of the inlet face, which then precluded the propulsion effects. The grid generation complexity required the removal of the empennage.

The results are computed for three different free-stream flow conditions and compared with flight test data for surface pressure coefficients, surface tuft flow, and off-surface vortical flow characteristics that included breakdown phenomena. Excellent surface pressure correlations, both in terms of magnitude and overall trend, are obtained on the forebody throughout the examined range of flow conditions. Reasonable pressure agreement was found over the LEX; the general correlation tends to improve at higher angles of attack. The surface tuft flow and the off-surface vortex flow structures compared qualitatively well with the flight test results.

To evaluate the computational results, a wind tunnel investigation was conducted to determine the aerodynamic effects of existing configurational differences between the flight vehicle and the numerical model. This study revealed that in most cases, the geometrical approximations made to the numerical model had very little effect on overall aerodynamic characteristics. Furthermore, to validate the latter wind tunnel results at flight flow conditions, a computational study was conducted to determine the aerodynamic influence of differences in the Reynolds number. This computational study, which was performed on exactly the same grid, showed that an order-of-magnitude difference between the flight and wind tunnel Reynolds numbers produces negligible effects on the forebody and the LEX surface pressures as well as the longitudinal aerodynamic characteristics. Very good surface pressure correlation between wind tunnel and flight data was obtained on the LEX; however, the wind tunnel pressure data appear to be slightly below those of the flight measurement on the forebody, particularly at high angles of attack.

Introduction

Combat aircraft are often assessed on their high-angle-of-attack aerodynamic performance for achieving superior levels of sustained maneuverability and agility. At high attitude, the flow characteristics over these often geometrically complex aircraft configurations generally become very complicated and difficult to predict and control. One such flow characteristic is the inevitable vortical flow precipitated by flow separation that occurs when the aircraft operate at high angles of attack. In general, the presence of such vortical flow over an aircraft surface can be advantageous as long as it remains organized and stable; this flow produces vortex lift, which can enhance maneuverability. However, with increasing angle of attack, such a coherent vortex system is susceptible to instabilities such as breakdown or flow asymmetry, which cause undesirable pitching, yawing, and/or rolling moment characteristics. As a result, the flight-handling quality and controllability of these aircraft are adversely affected by such flow phenomena; the ability of the aircraft to maneuver with high agility is often limited. The fundamental understanding and predictability of flow phenomena for a wide range of flow conditions are of paramount interest from both research and real aircraft design perspectives.

The vortical flow formation or, in a more general form, the initial flow separation can be classified into two types. The first type is a flow separation that primarily occurs over a smooth surface geometry because of an adverse pressure gradient interacting with the boundary layer. Fluid viscosity provides the essential mechanism for this type of flow separation to occur; this suggests that its formation is highly sensitive to the local flow Reynolds number. A typical flow separation of this type occurs over a conic forebody at high angles of attack. Unlike the first, the second type of flow separation occurs at, and is primarily induced by, a surface discontinuity such as the sharp leading edges of a delta wing. Because of diminished sensitivity to the fluid viscosity, the latter type of flow separation, fixed at the surface discontinuity, is generally considered to be insensitive to the local flow Reynolds number. In this paper, the first and second type of flow separation is referred to as boundary layer and sharp edge flow separation, respectively. In recent years, various numerical (refs. 1 and 2) as well as experimental (refs. 3 6) research efforts have been made to quantify the effects of Reynolds number on different types of flow separation. The results from these studies are particularly important in providing insight into the flow physics and the triggering mechanisms

responsible for the subject flow separations. Specifically, the basic knowledge learned from these investigations may lead to the development of new computational and/or experimental techniques applicable to a conventional wind tunnel environment for simulating the high Reynolds number flow encountered by the flight vehicle.

Unique research is presently being conducted by NASA within the High-Angle-of-Attack Technology Program (HATP) (ref. 7), which has as its major objective the exploration of high-attitude flow characteristics over a typical fighter aircraft during maneuvering situations. At the outset, the F/A-18 aircraft was chosen to be the baseline configuration primarily because of its high-angle-of-attack (i.e., high-α) capability. Subsequently, an F/A-18 aircraft, designated as the High-Alpha Research Vehicle (HARV) (ref. 8), was highly instrumented for surface pressure measurements as well as in-flight flow visualization. (See refs. 9 and 10.) On- and off-surface flow visualizations have been conducted on the HARV; different techniques have been used and include one innovative approach to document surface flow patterns. (See ref. 9.) In addition to the flight experimentation, HATP is utilizing ground-based facilities to acquire experimental data from various wind tunnel scale models (refs. 11–15) as well as a full-size configuration, which has been tested in the Ames 80- by 120-Foot Wind Tunnel. (See ref. 16.) The results of these experiments have provided the database needed for the development and validation of the present computational fluid dynamics (CFD) methodologies.

In the past few years, significant progress has been made to fulfill the HATP objectives by providing detailed analyses of high-angle-of-attack flow over the F/A-18 aircraft. In particular, the numerical analyses based on the thin-layer Navier-Stokes formulation have made important contributions. Initial computational activities started in parallel at the Langley and Ames Research Centers. Two different approaches were taken to solve the flow over the isolated F/A-18 aircraft forebody which included the leading-edge extension (LEX) geometry. Although both approaches were based on multiblock structured grid strategies, one method used a nonoverlapping grid-block approach (refs. 17 and 18), and the other method was based on an overset grid or Chimera (ref. 19) approach. (See ref. 20.) Subsequently, both computational methods were expanded to include more of the F/A-18 aircraft geometrical components such as the wing, aft portion of the fuselage, and empennage (i.e., vertical and horizontal tails). These efforts were very successful and the computational results with both the multiblock overset (refs. 21–23) and nonoverlapping grids (ref. 24) are documented.

The primary objectives of the present investigation are summarized into the following five categories:

1. Expand prior thin-layer Navier-Stokes computations (ref. 24) for the F/A-18 aircraft configuration to include a wider range of flight flow conditions
2. Correlate computational results with flight test data for both on- and off-surface flow characteristics and surface pressure coefficients
3. Evaluate aerodynamic effects which result from the geometrical differences between the flight vehicle and the numerical model through wind tunnel experimentation
4. Correlate wind tunnel data with flight test results to assess the scale model simulation of high Reynolds number flow; in addition, numerically assess the effects of Reynolds number on the aerodynamic characteristics of the configuration
5. Correlate computational results with appropriate wind tunnel data obtained on a configuration that is more representative of the numerical model

Symbols

b_{ref}	reference wing span, 37.42 ft
C_D	drag coefficient, $\dfrac{\text{Drag}}{q_\infty S_{\text{ref}}}$
C_L	lift coefficient, $\dfrac{\text{Lift}}{q_\infty S_{\text{ref}}}$
C_m	pitching moment coefficient referenced to $0.25\bar{c}$, $\dfrac{\text{Pitching moment}}{q_\infty S_{\text{ref}} \bar{c}}$
C_p	pressure coefficient, $\dfrac{p - p_\infty}{q_\infty}$
$\bar{c}$	wing mean aerodynamic chord, 11.52 ft
c.g.	center of gravity
E_o	total energy per unit volume
$\hat{\mathbf{F}}, \hat{\mathbf{G}}, \hat{\mathbf{H}}$	flux vectors
$\hat{\mathbf{f}}$	net flux
J	Jacobian of coordinate transformation
l	configuration body length measured from nose to exhaust nozzle exit plane, full scale, 54.4 ft
M_o	Mach number
M_∞	free-stream Mach number

p	static pressure
p_o	free-stream total pressure
$p_{o,l}$	local total pressure
$p_{o,l}/p_o$	normalized total pressure
p_∞	free-stream static pressure
$\widehat{\mathbf{Q}}$	state vector, $J^{-1}[\rho, \rho u, \rho v, \rho w, E_o]^T$
q_∞	free-stream dynamic pressure, lb/ft^2
$R_{\bar{c}}$	Reynolds number based on $\bar{c}$
S_{ref}	reference area of wing planform, 400 ft^2
s	LEX local-exposed semispan, in.
t	time, sec
u, v, w	body-axis Cartesian velocity components, ft/sec
v^*	wall friction velocity, $\sqrt{\frac{\tau_w}{\rho}}$, ft/sec
x	axial distance from nose apex, in.
x/l	fraction of configuration body length
y	distance along LEX local-exposed semispan, in.
y/s	fraction of LEX-exposed semispan
y^+	inner-law variable, $\frac{yv^*}{\nu}$
α	angle of attack, deg
δ_f	flap deflection angle, deg
μ	viscosity, lb-sec/ft^2
ν	kinematic viscosity, $\frac{\mu}{\rho}$, ft^2/sec
θ	azimuthal angle measured clockwise viewed from front, deg (0° located at bottom dead center)
ξ, η, ζ	body-fitted coordinates
ρ	density, slug/ft^3
τ_w	wall shear stress, lb/ft^2

Abbreviations:

CAD	computer-aided design
CFD	computational fluid dynamics
C-O	grid topology, C streamwise and O circumferential
FS	fuselage station, full-scale, in.
HARV	High-Alpha Research Vehicle
HATP	High-Angle-of-Attack Technology Program
H-H	grid topology, H streamwise and circumferential
H-O	grid topology, H streamwise and O circumferential
HST	High-Speed Tunnel
IGES	Initial Graphics Exchange Specification
LEX	leading-edge extension
MUSCL	monotone upstream-centered scheme for conservation laws
NAS	numerical aerodynamic simulation
NASA	National Aeronautics and Space Administration
WT	wind tunnel

A caret (ˆ) over a symbol indicates scaling with respect to the Jacobian J of the coordinate transformation.

Sources of Data

Flight Experiment

The F/A-18 aircraft was chosen as a baseline configuration for the HATP, primarily because of its high-α capabilities. The aircraft (fig. 1), designated the High-Alpha Research Vehicle (HARV), is instrumented to measure surface static pressures over the forebody and on both starboard and port sides of the LEX. The three views of the F/A-18 aircraft configuration are shown in figure 2. The figure also provides the full-scale reference dimensions in feet. Figure 3 presents the planform of an F/A-18 aircraft configuration and the corresponding cross-sectional geometry of the forebody and LEX fuselage stations (FS) where the surface pressures are measured. The forebody surface pressure orifices were distributed as a function of θ at longitudinal FS 70, 85, 107, 142, and 184. These full-scale dimensions are in inches; for reference, the nose apex starts at FS $\approx$ 60. When the cross section is viewed by looking aft, the azimuthal angle θ is measured clockwise from the windward plane of symmetry of $\theta = 0°$; the LEX surface pressures were measured as a function of LEX-exposed semispan y/s on both the upper and lower surfaces at FS 253, 296, and 357. The semispan parameter $y/s = 0$ corresponds to the LEX-fuselage juncture and $y/s = 1$ corresponds to the LEX leading edge.

Negative values of the parameter y/s correspond to the starboard side and positive values to the port side of the configuration.

The aircraft is also equipped with a smoke-generating system (refs. 9 and 10) designed to emit smoke at appropriate locations along the forebody and the LEX apex for visualization of the off-surface vortical flows as well as their interactions with one another and/or with the neighboring aerodynamic surfaces. In conjunction with the off-surface flow visualization, surface tufts are used on the wing, LEX, fuselage, and tails to assist in correlation of the off-surface flow interactions with the surface flow. These in-flight flow visualization images are recorded by a camera located either onboard the aircraft or a chase plane. Furthermore, a unique approach has also been successfully used to capture the in-flight surface flow pattern on the forebody and the LEX. (See ref. 9.) The data gathered from the flight experiments have been instrumental in helping researchers understand the subject flow phenomena. All the HARV flight experiments were conducted by NASA at the Dryden Flight Research Center. The flight data are obtained for a wide range of angle of attack, Mach number, and sideslip. (See ref. 10.)

Computational Fluid Dynamics

The primary objective of the present computational analysis is to expand the earlier computations (ref. 24) to include a wider range of flow conditions and a more comprehensive flow analysis. Various HARV flight test results (e.g., on- and off-surface flow visualization photographs, surface pressure data) were initially examined to identify those flow conditions which exhibited the most challenging flow characteristics to be simulated numerically. Several flow conditions (table I) were identified which clearly demonstrate the complexity associated with the overall flow structures (e.g., LEX vortices with subsequent breakdown at high-α conditions, forebody vortices, forebody-LEX vortex interactions, and/or stalled flow over the wing).

Table I. Selected Flow Conditions

α, deg	M_∞	R_c	δ_f, deg
19	0.34	13.5×10^6	25
25.8	.25	10.8	34
30.3	.24	10.2	34

Surface grid. The surface patch definition of the complete F/A-18 aircraft was obtained from a detailed computer-aided design (CAD) description in a format known as Initial Graphics Exchange Specification (IGES). (See ref. 25.) These data were then used to extract a high-density surface grid definition in the form of cross sections. The CFD database grid consisted of approximately 30 000 points on the fuselage defined at 60 cross sections and 16 000 points on the wing defined at 20 streamwise cuts. Although not used in the present computations, accurate surface definitions of both horizontal and vertical tails were also included in this database.

This database was subsequently used to generate a suitable surface grid for Navier-Stokes computations by using an Overhauser function (ref. 26) for the interpolation. This function has been shown to alleviate the oscillatory behavior inherent in other widely used functions (e.g., splines) in the region where grid point distributions are not uniform. The final computational surface grid was composed of approximately 18 000 points. The geometrical simplifications made to the configuration included the fairing over of the inlet, splitter plate, diverter, and the LEX slot. Figure 4(a) shows a body cross section at FS 401 and illustrates the simplifications made to the splitter plate and the diverter cavity region. Similarly, figure 4(b) shows a body cross section at FS 441 and illustrates the closing of the LEX slot as well as the fairing of the cavity region between the inlet and the LEX lower surface. The latter simplification is made to a limited region to facilitate the flow-field grid generation in that area. Except for the simplified regions, the two typical cross sections shown in figures 4(a) and 4(b) demonstrate the accuracy with which the computational grid ($\approx$100 grid points/station) represents the surface geometry of the much finer initial CAD cross-sectional definition ($\approx$500 grid points/station) despite the use of only about a fifth as many grid points. Two orthographic views of the final F/A-18 aircraft CFD surface grid definition are shown in figures 5(a) and 5(b) to illustrate the overall grid resolution. Furthermore, the wing geometry is modeled with two different leading-edge flaps: the undeflected and the blended flap. The latter will be discussed in the next paragraph.

The F/A-18 aircraft wing leading-edge flap deflection angle varies as a function of angle of attack and Mach number. For free-stream subsonic Mach numbers ($M_\infty \leq 0.76$), the aircraft control system is programmed to vary the flap deflection angle linearly as a function of angle of attack according to the relationship $\delta_f = 34\alpha/25.6$. The maximum flap deflection angle of 34° is reached when $\alpha = 25.6°$ and the flap angle remains constant for $\alpha \geq 25.6°$.

As a result, the flap deflection angles, which correspond to the flow conditions (table I) of this investigation are as follow: $\delta_f = 25°$ for $\alpha = 19°$ and $\delta_f = 34°$ for $\alpha = 25.8°$ and 30.3°. To simplify the flow-field grid generation, the surface geometry of the wing deflected leading-edge flap was approximated in this computation and is designated as a blended flap. The principle behind the deflected flap geometry modification was the preservation of the wing-body intersection with the undeflected flap, which permitted the same overall blocking strategy to be used for both undeflected and blended flap configurations. This modification smoothly blended the inboard 15-percent semispan of the flap between the deflected flap and the undeflected flap wing-body intersection. A nose-down front view of the F/A-18 aircraft CFD surface grid definition with both the blended flap (starboard) and undeflected flap (port) is shown in figure 6. In addition, a closeup view of the CFD surface definition is shown in figure 7 with shading to highlight the surfaces of the baseline F/A-18 aircraft that are simplified, blended, and/or modified (e.g., inlet, diverter, splitter plate, and the inboard section of the deflected wing leading-edge flap).

Flow-field grid. The selection of the flow-field grid strategy is primarily dictated by the two distinct types of aerodynamic shapes of the F/A-18 aircraft configuration: a slender type, which consists of the front forebody-LEX geometry, and a high-aspect-ratio type, which contains the wing component. An H-O grid topology is selected for the slender part, whereas a C-O grid is chosen for the high-aspect-ratio wing configuration. A unique global grid strategy is then devised which appropriately links various grid topologies while maintaining the grid quality. To illustrate the selected global grid strategy, isometric far-field (fig. 8(a)) and near-field (fig. 8(b)) views of the shaded F/A-18 aircraft surface are shown for the configuration maximum half-breadth plane along with the field grids in the plane of symmetry. For clarity, the grid density shown in the figures has been reduced in both longitudinal and radial directions. The flow-field domain, which consists of about 1.24 million grid points, is divided into five regions with each composed of one or more topologically similar blocks. In figures 8(a) and 8(b), the region boundary edges are highlighted with thick, solid lines and the corresponding block interfaces within each region are denoted by thick, dashed lines.

A side view of the flow-field grid for selected surfaces is shown in figure 9 to illustrate the various regions from a different perspective. The figure depicts the overall three-dimensional far-field boundaries with the wing wedge-shaped region sectioned out of the field domain. Again, the boundaries of the various regions and the corresponding block interfaces are highlighted with thick, solid and dashed lines, respectively. Three factors contributed to the selection of the grid topology for each region: the consideration of local geometry, the proper resolution of the expected flow structure, and the appropriate grid connectivity between regions. The selected topologies should provide good resolution (refs. 17 and 18) of all edge flows (e.g., LEX and wing leading edges and wingtip) and juncture flows (e.g., LEX-body, wing-body, and canopy-body).

The volume grid is generated with established transfinite interpolation techniques (refs. 17, 24, and 27) with sufficient normal clustering near the surface to adequately resolve the laminar sublayer of the turbulent-boundary-layer flow for a typical flight free-stream condition of $\alpha = 19°$, $M_\infty = 0.34$, and $R_{\bar{c}} = 13.5 \times 10^6$. This grid produced an average normal cell size next to the wall of approximately $7.2 \times 10^{-6}\bar{c}$, which corresponds to $y^+ \approx 3$ for turbulent computations; a laminar sublayer generally extends out to $y^+ \approx 8.5$. The radial far-field boundary extends to about $7.6\bar{c}$. A downstream grid extension is created by repeating the grids generated about the base cross section aft to about $4.7\bar{c}$. No grid is generated for the face of the base geometry (i.e., open), nor is the flow simulated between the interior surfaces of the model geometry and the exterior flow-field domain. Note that the flow-field grid structure is generally designed to be consistent with those of previous computational studies (refs. 17 and 28) on the isolated F/A-18 aircraft forebody-LEX configuration where the structures had been found to have adequate cell size next to the wall, radial grid stretching, circumferential grid resolution, and far-field boundary locations.

Computational methodology. The computational results have been obtained from an algorithm that has been successfully applied to a variety of aerodynamic problems with both simple and complex configurations for a wide range of flow conditions. (See refs. 2, 17, 18, 24, and 27.) The algorithm (refs. 1, 17, 18, and 29 31) is based on the compressible, time-dependent, Reynolds-averaged, Navier-Stokes equations, which are written in a curvilinear coordinate system. The equations are solved with a finite volume approach and are composed in a conservative form as

$$\hat{\mathbf{Q}}_{,t} + (\hat{\mathbf{F}} - \hat{\mathbf{F}}_v)_{,\xi} + (\hat{\mathbf{G}} - \hat{\mathbf{G}}_v)_{,\eta} + (\hat{\mathbf{H}} - \hat{\mathbf{H}}_v)_{,\zeta} = 0$$

The subscripts with a comma denote partial differentiation, the subscript v identifies the viscous

terms, and the caret ($\hat{}$) over the vectors indicates scaling with respect to the Jacobian J of the coordinate transformation. Details of these terms are included in reference 17. In addition to the ideal gas assumption in the present study, the thin-layer approximation of the governing equations is invoked (i.e., $\hat{\mathbf{F}}_v = \hat{\mathbf{G}}_v = 0$) and thus accounts for viscous flux terms only in the direction ζ normal to the body. Turbulence effects are accounted for by the notion of eddy viscosity and conductivity. The algebraic turbulence model developed by Baldwin and Lomax (ref. 32) is used to evaluate the required turbulence quantities. For separated vortical flow regions, the method introduced by Degani and Schiff (ref. 33) is used to ensure that the proper turbulence length scales are used.

The integral form of the conservation equations is represented by

$$\frac{\partial}{\partial t}\int\int\int \hat{\mathbf{Q}}\, dV + \int\int \hat{\mathbf{f}} \cdot \hat{\mathbf{n}}\, dS = 0$$

where the time rate of change ∂t of the state vector $\hat{\mathbf{Q}}$ within a cell volume dV is balanced by the net flux $\hat{\mathbf{f}}$ across the cell surface dS with the unit normal $\hat{\mathbf{n}}$. The convective and pressure flux quantities are represented by the upwind-biased, flux-difference-splitting approach of Roe (ref. 34), whereas the shear stress and heat transfer terms are centrally differenced. The monotone upstream-centered scheme for conservation laws (MUSCL) of Van Leer (ref. 35) is used to interpolate state variables at the cell interfaces. A detailed discussion on the algorithm development for interpolating the mass, momentum, and energy across the various planar and nonplanar interfaces that separate the grid blocks is presented by Biedron and Thomas in reference 31.

Method performance and convergence. All computations are performed on the numerical aerodynamic simulation (NAS) Cray-2* computer, located at Ames Research Center. On this machine, the algorithm requires approximately 20 μsec per iteration per grid point and about 100 million words of memory. Starting from the free-stream flow condition, a typical solution converged in about 3000 iterations, which consumed about 20 hr of computer time. The 3000 iterations were sufficient to reduce the residuals by a little more than 2 orders of magnitude and to reduce oscillations in C_L to a negligible level as shown in figures 10(a) and 10(b), respectively. Subsequent solutions for different angles of attack were obtained by starting the computations from an existing solution, which then generally reduced the computational time for a converged result by as much as a half. Similar convergence rates are achieved for the computations at higher angles of attack despite the presence of vortex breakdown in the solutions. The computations are performed without the use of mesh sequencing or multigrid iteration. (See ref. 29.)

*Trademark of Cray Research, Inc., Minneapolis, MN 55402.

Wind Tunnel Experiment

The wind tunnel experiment was conducted in the Langley 7- by 10-Foot High-Speed Tunnel (HST). (See refs. 36 and 37.) This is a closed-circuit, continuous-flow, atmospheric tunnel with a solid wall test section 6.6 ft high, 9.6 ft wide, and 10 ft long. The tunnel has an operational Mach number range of 0 to 0.9 with a maximum Reynolds number of about 4×10^6 ft^{-1}.

The wind tunnel testing was conducted with a 0.06-scale model of the F/A-18 aircraft configuration. This wind tunnel model had been used in a previous experimental investigation, and the results are published in reference 12. The model was instrumented for surface static pressure measurements at four stations on the forebody and three stations on the LEX upper surface; LEX lower surface measurements were taken only at the last station FS 357. The surface pressures were measured on both starboard and port sides of the aircraft to assess flow asymmetry. The fuselage stations on the model at which the surface pressures are measured are identical to those of the flight vehicle with the exception of the first forebody station FS 70 where no model data were acquired. The sting-mounted wind tunnel model (fig. 11) was equipped with an internally mounted strain gauge balance to measure the six component forces and moments. Furthermore, the forebody of the model was equipped with two transition grit strips positioned longitudinally across the windward plane of symmetry at $\theta = 45°$ and 315°. Based on the method of reference 38, the No. 180 grit was found to be adequate for tripping the laminar boundary layer to a turbulent flow to simulate the flight Reynolds number flow characteristics at the conditions listed in table I.

Two different configurations of the model were tested: the first was the baseline F/A-18 aircraft and the second incorporated modifications representative of the numerical model. The second configuration is referred to as the "CFD wind tunnel model" (CFD WT) from here on. The data obtained from the

CFD wind tunnel model are used to assess the aerodynamic effects of empennage removal, inlet fairing, and wing leading-edge flap deflection. Modifications of the baseline wind tunnel model were patterned after the numerical representation. Dental plaster was used for fairing over regions of the model such as the inlet and diverter. Figures 12(a) and 12(b) show the CFD wind tunnel model from two perspectives and illustrate the various modifications of the baseline F/A-18 aircraft wind tunnel model such as fairing over the inlet, splitter plate, and diverter; closing of the gap between the deflected flap and fuselage; and the removal of the empennage.

The CFD wind tunnel model was a good representation of the numerical model except in the regions of the blended flap and the splitter plate. Unlike the numerical model, where surface modifications were made to the inboard 15-percent semispan of the flap by a smooth blending of the deflected flap geometry to the undeflected flap wing-body intersection, the CFD wind tunnel model did not incorporate flap surface blending. However, the gap between the inboard face of the deflected flap and the fuselage was closed with a metal sheet (fig. 12(b)) that vertically joined the two edges. This gap remained closed for the deflected flap configurations of the present CFD wind tunnel model. Furthermore, dental plaster was also used to fair over the cavity region between the splitter plate and the fuselage but in a slightly different manner than the numerical model approach (fig. 4(a)) in which the lower part of the splitter plate was truncated. This difference between the numerical model and the CFD wind tunnel model in the geometric representation of the splitter plate and diverter cavity regions is illustrated for a typical cross section at FS 401 in the lower right corner of figure 12(b).

The measured wind tunnel data are corrected for the effects of angle of attack, wall interference, and model base drag. The model support system incorporated an accelerometer to measure the angle of attack and is subsequently corrected to account for the balance and sting deflection under load. The wall interference effects are accounted for by the principles of blockage (ref. 39) and jet boundary (ref. 40) corrections. The model base pressures are measured and subsequently integrated to obtain the resulting force acting normal to the base plane of the model. This normal force is then subtracted from the total axial force component measured by the internally mounted strain gauge balance to exclude the pressure drag caused by the local wake flow on the base of the model. As a result, the model base pressure drag contribution to the configuration total forces and moments is adjusted to correspond to the free-stream static pressure p_∞. Surface pressure measurements are obtained with electronically scanned pressure (ESP) transducers; the overall accuracy of this system is about ± 0.1 percent of the full-load range, which is approximately equal to ± 0.03 lb/in^2.

Results and Discussion

CFD Versus Flight Data

General flow features. The normalized total pressure $p_{o,l}/p_o$ contours in various cross-flow planes as well as the LEX and forebody vortex core streamlines (where applicable) computed at the selected flow conditions (table I) are shown in figures 13(a) 13(c). The magnitude associated with each normalized total pressure contour is displayed with the appropriate color bar. The normalized total pressure function is used to highlight the viscous losses within a separated flow structure such as a vortex. For the same purpose, this function has also been successfully used in an experimental investigation reported in reference 41. The results shown in figures 13(a)–13(c) are all obtained with a fully turbulent boundary layer model at flight flow conditions with the blended flap configuration. The computations are performed for half the configuration, but the results are presented for the full configuration by using the mirror-image principle of symmetry. Although both Mach and Reynolds numbers vary slightly, the computational results presented in figures 13(a) 13(c) reveal the effects of angle of attack on the flow characteristics. These figures, discussed in the subsequent paragraphs, highlight the following three general flow features and their interactions: LEX vortex system, wing flow field, and forebody flow field.

The normalized total pressure contours in figures 13(a) 13(c) clearly indicate the presence of a well-organized LEX vortex flow structure up to the LEX-wing leading-edge juncture. Over this longitudinal extent, the overall LEX vortical flow structure generally remains similar even as the angle of attack is increased. At $\alpha = 19°$, the LEX primary vortex system appears to remain coherent and maintain its tight core structure over the entire configuration body length. However, with increasing angle of attack, figures 13(b) and 13(c) illustrate that the LEX vortex core region (highlighted by the lower levels of the normalized total pressure, which signify higher levels of viscous loss) expands dramatically aft of about the wing root midchord. This sudden core expansion in the LEX vortical flow system is generally associated with a phenomenon referred to as vortex burst or breakdown. The vortex breakdown is

often characterized by an abrupt reduction in velocity (particularly the axial component) and the loss of cohesiveness within the vortical flow structure. The latter effect is clearly demonstrated by the LEX vortex core streamlines at $\alpha = 25.8°$ and 30.3°. The predicted location of the LEX vortex breakdown is discussed later in conjunction with flight and wind tunnel test results.

The normalized total pressure contours at $\alpha = 19°$ clearly illustrate the separated flow region over the wing upper surface. This massive flow separation over the wing is essentially a confined region of retarded airflow with a chaotic behavior which is discussed in reference 24. When the angles of attack are increased to 25.8° and 30.3°, the separated flow region over the wing appears to move outboard and exhibits lower levels of viscous loss as indicated by the higher levels of the normalized total pressure. One contributor to this flow change is the expansion of the LEX vortex flow which extends spanwise onto the wing with increasing angle of attack.

With increasing angle of attack, the flow within the boundary layer over the smooth leeward side of the forebody separates and leads to a well-organized vortical flow structure as shown in figures 13(b) and 13(c). At about the middle (fig. 13(b)) or immediately aft (fig. 13(c)) of the canopy, the forebody vortex migrates downstream into a region where its trajectory becomes affected by the much stronger neighboring LEX vortex system. The forebody vortex flow is initially drawn into the LEX-fuselage juncture from which it is entrained outboard by the LEX vortex system. Note that just aft of the wing LEX leading-edge juncture, the streamlines originating from the forebody vortex core split; some wrap around the LEX vortical flow and the rest interact with the wing flow field.

The HARV in-flight photographs (ref. 9) of the tufts as well as the LEX primary vortex core smoke visualization are presented in figures 14(a), 14(b), and 14(c) for $\alpha \approx 20°$, 25°, and 30°, respectively. The photographs clearly illustrate the LEX vortex breakdown just ahead of the vertical tail at $\alpha \approx 20°$ and its upstream progression with increasing angle of attack. In addition, the tufts show the surface flow patterns over the wing, LEX, fuselage aft of the canopy, and the vertical tail. In general, for this range of angle of attack, the tufts reveal a fairly orderly flow pattern over the LEX up to the LEX-wing leading-edge juncture. However, the tufts clearly indicate a chaotic flow pattern over the wing and the vertical tail with some tufts standing up off the surface; these disordered flow structures are directly attributed to stalled flow over the wing because of a massive flow separation and the LEX vortex breakdown, respectively.

Computational results for LEX vortex core streamlines superimposed on surface tuft flow patterns are presented in figures 15(a) 15(c) for the flow conditions listed in table I. For the higher angles of attack (i.e., $\alpha = 25.8°$ and 30.3°), the forebody vortex core streamlines are also shown to highlight their paths and influence on the overall flow structures both on and off the surface. Surface tuft flow patterns are simulated computationally with the method of unrestricted streamline tracing introduced and discussed in detail in reference 24. Unlike the conventional method of tracing the experimental surface oil flows and tuft patterns, this new approach does not impose the restriction that the streamline calculations lie in a particular grid plane near the surface. The method (ref. 24) has demonstrated the capability of simulating surface flow patterns in regions of attached as well as separated flows and is particularly applicable to a stalled flow environment. Because of the stalled flow characteristics over the wing, the method applied here initiated the particle tracing at a grid plane slightly off the surface ($\approx$0.02 in. full scale, which is $\approx 0.00014\bar{c}$) where the flow velocity magnitudes become sufficiently large to produce a visible tuft flow pattern within a reasonable number of time steps. Note that the number of time steps used in computing the unrestricted streamline traces is constant, which results in variable length traces because of the nonuniform distribution of the velocity magnitudes in a given flow region. The tuft flow patterns of the model shown in figures 15(a) 15(c) qualitatively simulate those patterns including the stalled flow region over the wing observed on the flight aircraft.

The simulated tuft flow patterns appear to have been influenced by the off-surface flow structures such as the LEX vortices. This effect is particularly evident over the wing in the aft inboard region where the tufts indicate a spanwise flow pattern caused by the flow expansion around the LEX vortex breakdown at $\alpha = 25.8°$ and 30.3°. This flow expansion around the LEX vortex breakdown and the resulting interaction with the wing flow field is also evident in the computational results shown earlier in figures 13(b) and 13(c). The accuracy of the predicted longitudinal location of the LEX vortex breakdown as a function of angle of attack is discussed in the next two paragraphs.

Several approaches, publically available in the scientific literature, have been devised to locate the vortex breakdown in a given flow structure. One such method that has been widely investigated and

is adopted here defines the onset of vortex breakdown at a point in the core where the axial velocity component becomes zero (i.e., $u = 0$) or reverses direction (i.e., $u \leq 0$) from that of the free-stream component. (See ref. 29.) The present numerical solutions are examined one cross-flow plane at a time to determine the magnitude of u within the LEX primary vortex core. By this analysis, no evidence exists that a vortex breakdown occurs at $\alpha = 19°$; however, at $\alpha = 25.8°$ and 30.3°, the LEX vortex breakdown develops longitudinally at $x/l \approx 0.72$ and 0.65, respectively.

The predicted LEX primary vortex breakdown locations are presented in figure 16 along with those obtained from different flight (ref. 42) and wind tunnel (refs. 12 and 15) experiments at subsonic conditions for various angles of attack. The experimental investigation of reference 15 was conducted in a low-speed tunnel with a 7- by 9-ft test section on a 1/9-scale model of the F/A-18 aircraft at $R_{\bar{c}} \approx 1 \times 10^6$. The wind tunnel data for the longitudinal location of the LEX vortex breakdown are presented over a range of $\alpha = 21.5°$ to 29° for the configuration with and without the empennage (i.e., vertical and horizontal tails). The data for the baseline configuration (i.e., with empennage) indicate that the vortex breakdown location moves upstream with increasing angle of attack and that the overall characteristics generally correlate well with the data gathered from other sources. However, the data (ref. 15) presented in figure 16 clearly indicate that the LEX vortex breakdown moves further aft without the empennage, particularly for the lower range of angle of attack (i.e., $21.5° \leq \alpha \leq 24°$). As expected, the empennage and, in particular, the vertical tails, which are located downstream in the path of the LEX vortical flow, induce a pressure-field disturbance that propagates upstream and precipitates vortex breakdown. The vortex breakdown location is predicted farther aft than those obtained experimentally at $\alpha \approx 26°$ and 30°. Although no data are presented in reference 15 for the LEX vortex breakdown location at $\alpha = 19°$, which corresponds to the angle of attack of interest in the present computation, the trend of the data reported for the tailless (i.e., without empennage) configuration indicates a strong possibility of a coherent vortex system over the entire length of the configuration. The absence of a LEX vortex breakdown at $\alpha = 19°$ is consistent with the present computational prediction as discussed in the previous paragraph.

Surface pressures. The static surface pressure coefficients computed for the F/A-18 aircraft configuration at the selected flow conditions (table I) with $\delta_f = 25°$ are shown in figures 17(a)–17(c). The surface pressure coefficients are contoured at constant values ranging from 1.0 to −3.0 for all three angles of attack. (See the color bar.) At high angles of attack, the suction peaks in two small regions of the LEX apex and over the blended flap exceed the lower contoured limit of −3.0; the pressure coefficients in these two regions are represented by solid white. Limitation of the pressure coefficient contours to a narrower range would allow more color variation, which would accentuate the pressure gradients. The following stations at which both flight and wind tunnel data have been measured are highlighted in white: FS 85, 107, 142, 184, 253, 296, and 357.

The effects of angle of attack on the computed surface pressure coefficients as presented in figures 17(a)–17(c) appear to be most pronounced in two regions. These regions over the LEX and the wing upper surface are directly influenced by the neighboring off-surface LEX vortex system and stalled flow over the wing, respectively. With increasing angle of attack, the LEX vortical flow appears to accumulate more strength as evidenced by the higher suction-peak footprint. At high angles of attack (i.e., $\alpha \geq 25.8°$), the increase in the LEX vortex strength not only affects the aerodynamic loads on the LEX surface, but it also has significant influence on the adjacent surfaces. For example, figure 17(c) clearly illustrates regions of low pressures acting on the fuselage aft of the canopy; these pressure levels are comparable in magnitude to those computed on the LEX upper surface.

At $\alpha = 19°$, figure 17(a) indicates that a major area of the wing upper surface, aft of the wing-flap hinge line, has pressure coefficient levels of about $-0.7 \leq C_p \leq 0.4$. As discussed earlier in conjunction with the tuft patterns (figs. 14(a)–14(c) for flight tests and figs. 15(a)–15(c) for numerical simulation), this portion of the wing exhibited chaotic flow characteristics attributed to stalled flow. With increasing angle of attack, the surface pressure coefficients computed on the wing upper surface show an extended region of lower C_p levels (i.e., $C_p \leq -0.7$) because of the localized flow expansion. Also evident was a suction-peak footprint associated with a leading-edge vortex flow, which developed over the blended flap region at $\alpha = 19°$ and intensified significantly with increasing angle of attack. At $\alpha = 19°$, the surface pressure coefficients indicate a small suction-peak footprint associated with the wingtip vortical flow, which does not appear in the solutions at higher angles of attack.

The surface pressure coefficients computed for the F/A-18 aircraft configuration at all three angles of attack are presented in figures 18(a) and 18(b). The pressure coefficients at the forebody stations are shown in figure 18(a) and are plotted as a function of θ. (See fig. 3.) In general, the forebody surface pressure distribution shows an increasing suction-peak level with increasing angle of attack. The computed surface pressures suggest an incipient flow separation at $\theta \approx 150°$ (starboard) and 210° (port side) between FS 142 and FS 184 for $\alpha = 25.8°$ and FS 107 and FS 142 for $\alpha = 30.3°$. These flow separations would subsequently form the leeward forebody vortices with clearly defined suction-peak footprints (i.e., $\theta \approx 155°$ and 205°) at FS 184 for both $\alpha = 25.8°$ and 30.3°. Because the forebody geometry is composed of a smooth curved surface with no discontinuities (or limited to within the numerical discretization error), the triggering mechanism for the resulting flow separation is an adverse pressure gradient within the boundary layer.

The computed LEX surface pressure coefficients are plotted in figure 18(b) as a function of LEX-exposed semispan y/s. The LEX pressure distributions are presented for the same range as in the previous color contour figures 17(a)–17(c). In general, the LEX upper surface pressure distribution can be characterized by a large suction-peak footprint, at $y/s \approx \pm 0.50$ associated with the primary vortex system. At $y/s \approx \pm 0.80$ just outboard of this large suction-peak footprint at FS 296 and FS 357, areas of smaller suction-peak footprints exist that correspond to the LEX secondary vortex system. Note that the sharp spikes in the LEX upper surface pressure distribution just inboard of the leading edge (i.e., $y/s \approx \pm 1$) result from numerical artifacts and have occurred previously in numerous computational studies of vortical flow separations from sharp-edged configurations. (See refs. 17, 20 24, and 43 44.) As with the forebody, the LEX pressure distributions also indicate higher suction peaks with increasing angle of attack, except at FS 357, where the lack of increase in the LEX primary suction peak for $\alpha > 25.8°$ can be attributed to the influence of vortex breakdown. However, this effect does not appear to impact the secondary vortex suction peak as evident from its consistent increase with increasing angle of attack. Note that the computed surface pressures at $\alpha = 30.3°$ clearly indicate a small low-pressure region over the upper surface LEX-fuselage juncture at FS 357 ($y/s \approx \pm 0.1$). This low-pressure region, which has also been seen both in wind tunnel and flight data, is chiefly attributed to the entrainment of the forebody vortices at the LEX-fuselage juncture. (See fig. 15(c).) The LEX lower surface pressure distribution shows increased compression at the higher angles of attack.

The correlations of the computed surface pressure coefficients with the flight data for the forebody and the LEX are presented in figures 19, 20, and 21 for $\alpha = 19°, 25.8°$, and 30.3°, respectively. Note that the flight data shown in figures 19(a) and 19(b) are obtained at slightly different flow conditions and with some geometrical differences between the numerical model and the flight vehicle. Experimental aerodynamic effects from the latter geometrical differences have been found to be small and are discussed in detail in the following section.

Computational and flight pressure coefficient data for the entire forebody length are in excellent agreement throughout the examined range of flow conditions. The computational results not only predict the overall pressures as well as the trends but accurately simulate the pressure distributions that correspond to small flow features such as the leeward forebody vortices. The pressure data disagreements at FS 142 ($\theta \approx 90°$ and 270°) are caused primarily by an antenna fairing on the HARV that was not modeled numerically. This antenna fairing can clearly be seen in the flight photograph of the HARV (fig. 14(a)) just ahead of FS 142 (highlighted in white). Note that for $\alpha = 30.3°$, the suction peak associated with the primary vortex flow at FS 142 ($\theta \approx 158°$ and 202°) is slightly underpredicted.

The computed upper and lower surface pressure coefficients for the LEX are generally in good agreement with the flight data at all three angles of attack. However, a more detail assessment of the pressure correlations reveals some differences and the possible causes. In general, the correlations tend to degrade in the outboard region, which is essentially dominated by the LEX secondary vortex flow. The LEX primary vortex suction peak is predicted to be slightly outboard at FS 253 and the magnitude is underestimated at FS 296 throughout the examined range of α. However, at the last LEX station FS 357, the magnitude of the primary vortex suction peak is predicted very well at the higher angles of attack of 25.8° and 30.3° but is underestimated at 19°.

Finally, the complete computational results are correlated with the corresponding flight data for the forebody and the LEX in figures 22(a) and 22(b). The results clearly demonstrate the accuracy with which the theoretical solutions predict the sensitivity of the surface pressures to changes in angle of attack. The incremental changes and trends of the computed surface pressure distributions as a function

of angle of attack appear to agree well with the corresponding flight data. In particular, note the fairly good prediction for the LEX primary vortex suction peak at FS 357, which reveals the upstream influence of the blockage precipitated by the vortex breakdown. A favorable correlation is also presented for the LEX lower surface pressure distributions, which clearly demonstrates pressure sensitivity to the angle of attack. As expected, the computed lower surface pressure distributions at FS 357 exhibit excess compression caused by fairing and closing off the inlet face and are discussed in the next section.

The present computational results are encouraging for simulating the overall flow features and the pressure distributions for the forebody and LEX configuration at various flight conditions. Nonetheless, a wind tunnel experiment was initiated to evaluate the aerodynamic effects of various configurational differences between the flight vehicle and the numerical model, such as inlet flow simulation, empennage, and the deflected flap geometry. As mentioned earlier, these simplifications of the numerical model were incorporated because of the limitations imposed by either the flow solver and/or the grid generation complexity.

Wind Tunnel Data

As discussed earlier, the experimental data presented here were obtained with a 0.06-scale F/A-18 aircraft model which was tested in the Langley 7- by 10-Foot High-Speed Tunnel. The primary objective of the test was to validate the present computational results by providing experimental data on a configuration that was more representative of the numerical model. The experimental data analysis was conducted to isolate the aerodynamic effects of the empennage (vertical and horizontal tails), inlet, and various flap deflection settings with and without the empennage by evaluating the surface pressure coefficients measured on the forebody and the LEX.

Effect of empennage. The forebody and LEX pressure coefficients measured on the CFD wind tunnel model, with and without empennage, are presented in figures 23(a) and 23(b) for $\delta_f = 0°$ at three angles of attack. In general, the removal of the empennage has minimal effect on measured pressure coefficients of the forebody as well as the LEX; at $\alpha = 19°$ the difference is almost indistinguishable. Also, note that at FS 357, the removal of the tails causes a very small increase in the suction level at $\alpha = 25.8°$.

These tail effects on the forebody and LEX pressures are presented in figures 24 and 25 for the same range of flow conditions at $\delta_f = 25°$ and $34°$, respectively. Generally, the forebody pressures remain insensitive to the empennage presence regardless of the flap deflection angle. However, the LEX pressures begin to be influenced by the presence of the tails, particularly in the aft LEX region. In general, the experimental data indicate that the augmentations of the vertical-horizontal tails result in the following:

1. Insignificant effect on the forebody pressures throughout the examined ranges of δ_f and α
2. Negligible effect on the LEX pressures measured at FS 253 and FS 296 throughout the examined ranges of δ_f and α
3. A slight decrease in the LEX vortex suction peak at FS 357; the effect is greater with increasing δ_f, particularly for $\alpha \geq 25.8°$

Effect of inlet fairing. The effect of the inlet fairing on the measured forebody and LEX surface pressure coefficients is presented in figures 26(a) and 26(b), respectively, for the flow conditions of interest. These aerodynamic data were obtained on the configuration that included the empennage and $\delta_f = 0°$. The results presented in the figure clearly demonstrate that fairing over the inlet face has very little effect on the measured forebody surface pressure coefficients throughout the examined range of α. However, the fairing over the inlet appears to slightly decrease (i.e., more negative) the measured pressure coefficients associated with the LEX primary and the secondary vortex suction peak, particularly at the adjacent aft stations. Note that the latter effects seem to diminish at higher angles of attack. As expected, the fairing over the inlet causes only slight flow compression under the LEX as reflected in the lower surface pressure coefficient measurements at FS 357.

Effect of flap deflection. The effect of the wing leading-edge flap deflection on the forebody and LEX pressure coefficients measured on the CFD wind tunnel model is presented in figures 27, 28, and 29 for $\alpha \approx 19°$, $26°$, and $30°$, respectively. The results clearly indicate that the flap deflection angle has negligible influence on the forebody and the LEX pressure coefficients throughout the examined range of α except at FS 357 for $\alpha \approx 30°$. (See fig. 29(b).) At this LEX station, the data reveal only a slight increase in both the primary as well as the secondary vortex suction peaks (i.e., more negative) with increasing flap deflection. Because of these small effects, the approximation (figs. 20 and 21) made in computing the flow over the configuration with $\delta_f = 25°$ (instead of $\delta_f = 34°$) for $\alpha \geq 25.6°$ is considered reasonable.

One of the objectives of this study was to ascertain whether the tails of the F/A-18 aircraft CFD

wind tunnel model would alter the previous conclusion with regard to the effect of flap deflection on the forebody and LEX pressures. Figures 30–32 show the experimental data obtained from the F/A-18 aircraft CFD wind tunnel model with the empennage. The aerodynamic effect of wing leading-edge flap deflection on the forebody and LEX pressure measurements appears to be insignificant over the examined range of α except at FS 357. The pressure distribution at the last LEX station shows a small sensitivity to the flap deflection at all three angles of attack. Unlike the results (fig. 29(b) for FS 357) discussed in the previous paragraph, the slight increase in both the primary and the secondary vortex suction peaks at FS 357 for $\alpha \approx 30°$ is no longer achieved with the empennage installed. Actually, at this angle of attack, the pressure distribution over the last LEX station (fig. 31(b)) indicates a slight drop in the primary and secondary vortex suction peak when increasing δ_f from 25° to 34°. The reduction in the LEX vortical flow suction peak at $\alpha \approx 30°$ with $\delta_f = 34°$ can be attributed to the nearby LEX primary vortex breakdown at $x/l \approx 0.45$ (fig. 16) precipitated by the empennage. In general, the effect of wing leading-edge flap deflection on the forebody and LEX surface pressure distribution over the F/A-18 aircraft CFD wind tunnel model with and without the empennage is small.

Flight Versus Wind Tunnel Data

As discussed in the previous section, the wind tunnel data are primarily used to determine the aerodynamic effects of the various geometrical differences between the numerical model and the HARV. Because the ultimate objective is to validate the computational results with the flight data, the accuracy with which the wind tunnel data simulated the flight Reynolds number flow characteristics is important. As mentioned earlier, the forebody of the scale model had grit strips that were positioned longitudinally across the windward plane of symmetry at azimuthal angles $\theta = 45°$ and 315° to trip the expected laminar boundary layer to a turbulent flow and thus simulate the assumed flight flow characteristics.

The forebody and LEX surface pressure coefficients measured on the CFD wind tunnel model with empennage are presented in figures 33, 34, and 35, for $\alpha \approx 19°$, 26°, and 30°, respectively. As discussed earlier (figs. 26(a) and 26(b)), the aerodynamic effects on the forebody and LEX pressures from the fairing of the inlet face when compared with the flow-through inlet were experimentally very small, confined only to the last LEX station, and diminished quickly at higher angles of attack. The wind tunnel pressure measurements on the forebody (figs. 33–35) reveal pressures that are slightly higher (i.e., more positive) than the flight data with the correlation for the aft stations FS 142 and FS 184 degrading with increasing angles of attack ($\alpha = 25.8°$ and 30.3°). The degradation in the surface pressure correlations is also apparent in the suction-peak regions of leeward forebody vortices at $\theta \approx 158°$ and 202°. As compared earlier (figs. 19–21), the pressure disagreements at FS 142 ($\theta \approx 90°$ and 270°) are primarily caused by an antenna fairing on the HARV that was not incorporated on the CFD wind tunnel model.

Figures 33–35 clearly indicate excellent correlation between the wind tunnel and flight data for all LEX stations in terms of both magnitude and general trends throughout the examined range of α. These favorable correlations are attributed to the inviscid flow characteristic of the LEX primary vortex separation line (i.e., fixed at the sharp leading edges), which leads to the development of the leeward vortical flows. As a result, the pressure distribution of the LEX primary vortex flow indicates only a small sensitivity to the difference between the flight and wind tunnel Reynolds numbers. The excellent correlation also extends to the LEX outboard region where the flow separation that leads to the formation of the secondary vortex structure is generally considered to be a boundary-layer phenomenon. Note that the slight pressure data disagreement on the lower surface of the last LEX station is primarily from additional compression caused by the fairing of the inlet face of the experimental wind tunnel model.

CFD Versus Wind Tunnel Data

The computational solutions were all obtained at flight Reynolds numbers which were generally about an order of magnitude higher than those achieved experimentally in the wind tunnel investigation. As a result, a computational study was performed to examine the effect of Reynolds number on the solutions. After assessing the Reynolds number effect, the measured surface pressure coefficients are correlated with the computational results for the forebody and the LEX configuration. In addition, the aerodynamic effects of the wing leading-edge flap deflections are evaluated experimentally as well as computationally. Finally, the measured forces and moments are correlated with the computational results.

Reynolds number effect. The primary objective of this section is to determine if the results of a typical existing solution computed at flight flow conditions are sensitive to an order-of-magnitude reduction in Reynolds number. A new solution with a fully turbulent flow assumption was computed with the same

flow-field grid by continuing the solutions from the results that had been obtained earlier at flight flow conditions. As expected, the new converged solutions at the wind tunnel Reynolds numbers indicate that the flow-field grid provides finer resolution of the boundary layer than that obtained earlier at flight Reynolds numbers. This finer grid resolution of the turbulent boundary layer flow is naturally extended onto the laminar sublayer region where it was resolved with $y^+ \approx 1$ instead of $y^+ \approx 3$ for the earlier computations at flight Reynolds number. On the basis of the prior solutions (ref. 17) obtained on the isolated F/A-18 aircraft forebody-LEX configuration, this order of grid refinement is not expected to have any significant effect on the present computational results.

The effect of Reynolds number on the computed forebody and the LEX surface pressure coefficients is shown in figures 36(a) and 36(b). The results clearly indicate that the computed surface pressure coefficients are insensitive to the change in Reynolds number at $\alpha = 19°$ and $M_\infty = 0.34$. At this flow condition, the Reynolds number effect on the computed forces and pitching moment was also small and is discussed later in conjunction with the measured wind tunnel data. To assess the sensitivity of the computational results to changes in Reynolds number at the higher angles of attack, a similar computational study was performed at $\alpha = 30.3°$ and $M_\infty = 0.24$. At this flow condition, the results also indicated that the surface pressure coefficients, forces, and pitching moment were generally insensitive to the change in Reynolds number. Note that the small sensitivity of the surface pressure distribution to the change in Reynolds number for a comparable range and magnitude has also been reported in reference 45 for a tangent ogive configuration at $\alpha = 30°$ and $M_\infty = 0.2$. These findings justify the surface pressure correlations between the present wind tunnel data and the computational results that have been obtained at flight Reynolds number flow conditions.

Surface pressures. The computed forebody and the LEX surface pressure coefficients are compared with the experimental data obtained on the CFD wind tunnel model (figs. 37–39) for the range of α of interest. The computed results are the same as those correlated earlier with the flight test data. Also, note the consistency of the configuration geometrical representation used for both sets of data such as the flap deflection angle, empennage, and inlet.

The pressure coefficients for the forebody indicate that the wind tunnel data measurements are slightly higher (i.e., more positive) than the computational predictions, which were shown earlier to be in excellent agreement with the flight data throughout the examined range of α. (See figs. 19–21.) In addition, measured surface pressure distributions at FS 184 do not indicate the expected suction-peak footprints associated with the presence of the vortical flows at higher angles of attack (i.e., $\alpha \geq 25.8°$).

The primary and secondary vortex suction-peak footprints in the measured LEX upper surface pressure distributions indicate that the expected overall flow physics of the LEX configuration has been experimentally simulated. The computed pressure coefficients on the LEX upper surface appear to be in reasonable agreement with the corresponding wind tunnel data for the examined range of α. As expected, the subject correlations reveal some existing differences that are generally very similar both in trend and magnitude to those discussed earlier in conjunction with the computational-flight data comparison. (See figs. 19–21.) The computed lower surface pressure distribution at FS 357 is clearly in good agreement with the measured wind tunnel data at all three angles of attack. This favorable correlation on the LEX lower surface can be attributed mainly to the similarity of the geometry representation for the inlet fairing in both the numerical and the CFD wind tunnel models.

Finally, the complete computational results are correlated with the corresponding wind tunnel data over the forebody and the LEX in figures 40(a) and 40(b), respectively. The results clearly show the sensitivity of the forebody and the LEX surface pressure distribution to the changes in angle of attack for both the computed and the measured wind tunnel data. Similar to the earlier comparisons between the computed and the flight test results (figs. 22(a) and 22(b)), the present wind tunnel data correlate reasonably well with the computational results in trends and incremental changes of the surface pressures as a function of angle of attack except for the vortex flow simulation at the aft forebody stations for the range of higher α. As discussed earlier, the discrepancies of surface pressures for the forebody, which had a smooth surface geometry with no discontinuities, are attributed chiefly to the lack of scale simulation of the high Reynolds number flow, particularly in the separated flow regions where the viscous effects dominate the ensuing flow characteristics.

Effect of flap deflection. The primary objective in this section is to investigate the capability of the present computational method to predict the aerodynamic effect resulting from different wing leading-edge flap deflections. The computational results as well as the experimentally measured surface pressure coefficients for the forebody and the LEX

configuration are presented for both $\delta = 0°$ and 25° in figures 41(a) and 41(b). The experimental data were obtained at flow conditions that were very close to those of the computations with the exception of the Reynolds number. However, at these flow conditions discussed earlier (figs. 36(a) and 36(b)), the computed surface pressure coefficients for the forebody and the LEX configuration were insensitive to the Reynolds number.

The aerodynamic effect of wing leading-edge flap deflection on the computed surface pressure coefficients on the forebody appears to be very small and nearly constant. Similarly, this insensitivity of the forebody pressures to the flap deflection is also evident from the experimental wind tunnel data presented in figure 41(a). However, the aerodynamic influence of flap deflection on the computed surface pressure coefficients for the LEX configuration appears to be slightly more pronounced, particularly at the aft stations where they become physically closer to the flap configuration. In general, the computed results show that the flap deflection causes an increase in the LEX suction-peak level in a region which essentially lies below the primary vortex flow. However, the experimental wind tunnel data indicate only a minimal change in the LEX-measured pressure distribution resulting from the flap deflection. The effects of flap deflection on the LEX lower surface pressures also appear to be small, as indicated by both the computational results and the measured data.

Forces and moments. In this section, the computed longitudinal aerodynamic characteristics are correlated with those experimentally measured on the CFD wind tunnel model. Because all the computational results were obtained initially at flight Reynolds numbers, which were generally about an order of magnitude greater than those achieved in the experiment, the effect of Reynolds number on the computed forces and moments for a typical case is evaluated. Note that a similar analysis on the surface pressure distributions, discussed earlier, indicated that an order-of-magnitude reduction in the Reynolds number had negligible effects on the computed surface pressures on the forebody and the LEX configuration.

The longitudinal aerodynamic characteristics, computed at both the flight and the wind tunnel Reynolds numbers, are presented in figure 42 for $\alpha = 19°$. Figure 42 also includes the corresponding experimental data point obtained for the wind tunnel model that matched the geometry of the numerical representation. To be consistent with the subsequent data analysis, plotting scales are selected for a range that bounds the overall available longitudinal aerodynamic characteristics. Among others, two specific conclusions can be drawn from the results with respect to the effects of Reynolds number on the computed forces and moments and the correlation between predicted and measured data. Similar to the earlier findings in conjunction with the surface pressures, the effect of Reynolds number on the computed total forces and moments also appears to be very small. However, note the slight increase in the drag coefficient, which is attributed directly to the reduction of the Reynolds number to match that achieved in the wind tunnel experiment. Furthermore, the computed results presented in figure 42 agree reasonably well with the measured wind tunnel data except for the total lift coefficient, which appears to have been slightly underpredicted. The lift underprediction at $\alpha = 19°$ is not surprising because as shown earlier with regard to the surface pressure coefficients (fig. 37(b)), the computational results also underpredicted the measured LEX primary vortex suction peak in the aft stations. As a result, the LEX vortex lift contribution to the total lift has probably been compromised.

Experimental and computational longitudinal aerodynamic characteristics for the entire range of flow conditions are presented in figure 43. The experimental data are presented for the CFD wind tunnel model and for the baseline F/A-18 aircraft configuration without geometrical alteration, which provided the necessary datum for the force and moment data analysis. Similarly, figure 43 shows corresponding computational results that have been obtained with the numerical model. Although the latter two sets of data are consistent with one another as a function of Mach number (i.e., $M_o \approx 0.34$, 0.25, and 0.24 for $\alpha \approx 19°$, 25.8°, and 30.3°, respectively), they differ slightly from the constant $M_\infty = 0.30$ at which the data for the baseline F/A-18 aircraft configuration were obtained. However, previous experimental data (ref. 12) obtained from the same 0.06-scale F/A-18 aircraft wind tunnel model clearly indicate that small variations (i.e., ± 0.05) in Mach number, particularly in the low subsonic range, do not have significant influence on overall longitudinal aerodynamic characteristics. The latter effect as well as the earlier finding of the influence of Reynolds number on the computed longitudinal aerodynamic characteristics validates the data correlations presented in figure 43 despite the inconsistencies in Mach and Reynolds numbers. The data analysis of the forces and moments is presented in the following three categories: the experimental aerodynamic characteristics for the baseline configuration,

the experimental aerodynamic characteristics for the CFD wind tunnel model, and the correlations between the computational results and the corresponding wind tunnel data.

The experimentally measured lift, drag, and pitching moment coefficients for the baseline F/A-18 aircraft configuration indicate essentially stable aerodynamic characteristics throughout the examined range of α. However, some degradation in aerodynamic characteristics is apparent, particularly in the reduced rate of increase in lift coefficient with increased angle of attack beyond $\approx 18°$, which can be attributed to the LEX vortex breakdown (fig. 16) and/or the stalled flow over the wing. (See figs. 14(a) and 15(a).) The pitching moment characteristics for the baseline configuration remain fairly stable (i.e., $dC_m/d\alpha < 0$) even at the range of higher α despite the loss of lift caused by the LEX vortex breakdown and stalled flow over the wing.

The experimentally determined effects of configuration geometrical simplifications on the longitudinal aerodynamic characteristics are evident in figure 43 by the difference between the data presented with open and solid circular symbols. The fairing of the inlet face and the removal of the empennage cause a slight decrease in lift and an increase in drag coefficients only at the higher angles of attack of 25.8° and 30.3°. These geometrical simplifications also result in a reversal of the pitching moment characteristics (i.e., $dC_m/d\alpha > 0$). Note that the latter change in the pitching moment characteristics can be attributed directly to the absence of the horizontal tail.

The computed longitudinal aerodynamic characteristics (i.e., solid square symbol) for the geometrically simplified F/A-18 aircraft configuration compare favorably with the corresponding wind tunnel data (i.e., solid circular symbol). The computed lift, drag, and pitching moment coefficients correlate reasonably well with experimental data throughout the examined range of α.

Concluding Remarks

Flow analyses of results from a variety of flight tests, wind tunnel experiments, and thin-layer Navier-Stokes flow simulations are presented for the F/A-18 aircraft configuration. The computational results are compared with flight test data of off-surface flow features, surface tuft flow patterns, and surface pressure distributions for three angles of attack. In general, the computational results correctly predict the major flow characteristics such as the forebody flow structures, the wing leading-edge extension (LEX) vortex system, and the subsequent vortex breakdown with increasing angle of attack, forebody and LEX vortex interactions, and deflected flap leading-edge flow separation leading to a stalled flow over the wing upper surface.

A wind tunnel experiment was conducted with a 0.06-scale F/A-18 aircraft model to ascertain the aerodynamic effects of the geometrical differences between the flight aircraft and the numerical model. The wind tunnel data revealed isolated aerodynamic effects of the empennage, fairing of the inlet face, and wing leading-edge flap deflection angles. In general, analyses indicated that the geometrical differences have only minimal influence on the surface pressure distributions on the forebody throughout the examined angle of attack range. However, the LEX surface pressures are affected slightly by the geometrical changes, particularly in the aft region and with increasing angle of attack.

The experimental wind tunnel data are also compared with the flight test results to determine the capability of the ground-based facility to simulate the flight Reynolds number flow characteristics. This study revealed that the LEX surface pressure coefficients measured on the wind tunnel scale model correlate very well with the flight test data. However, data analysis of the surface pressures on the forebody indicates some disagreement between the flight and wind tunnel data, particularly in the aft stations where the flow is separating at the higher angles of attack.

The wind tunnel data are presented for the longitudinal aerodynamic characteristics measured on the baseline F/A-18 aircraft configuration as well as the CFD wind tunnel model. These data reveal that the fairing of the inlet face and the removal of the empennage cause a slight decrease in lift and an increase in drag coefficients only at higher angles of attack. As expected, the experimental wind tunnel data also indicate that these geometrical simplifications resulted in a pitch-up moment characteristic. Furthermore, the computed longitudinal aerodynamic characteristics correlate reasonably well with the experimental measurements obtained on the CFD wind tunnel model.

NASA Langley Research Center
Hampton, VA 23681-0001
August 30, 1994

References

1. Thomas, James L.; and Newsome, Richard W.: Navier-Stokes Computations of Lee-Side Flows Over Delta Wings. AIAA-86-1049, May 1986.

2. McMillin, S. Naomi; Thomas, James L.; and Murman, Earll M.: *Navier-Stokes and Euler Solutions for Lee-Side Flows Over Supersonic Delta Wings A Correlation With Experiment.* NASA TP-3035, 1990.

3. Polhamus, Edward C.: *A Review of Some Reynolds Number Effects Related to Bodies at High Angles of Attack.* NASA CR-3809, 1984.

4. Keener, Earl R.: *Flow-Separation Patterns on Symmetric Forebodies.* NASA TM-86016, 1986.

5. Fisher, David F.; Banks, Daniel W.; and Richwine, David M.: F-18 High Alpha Research Vehicle Surface Pressures: Initial In-Flight Results and Correlation With Flow Visualization and Wind-Tunnel Data. *A Collection of Technical Papers—AIAA 8th Applied Aerodynamics Conference,* Part 1, Aug. 1990, pp. 421 451. (Available as AIAA-90-3018-CP.)

6. Hall, Robert M.: Influence of Reynolds Number on Forebody Side Forces for 3.5-Diameter Tangent-Ogive Bodies. AIAA-87-2274-CP, Aug. 1987.

7. Gilbert, William P.; and Gatlin, Donald H.: Review of the NASA High-Alpha Technology Program. *High-Angle-of-Attack Technology,* Volume I, Joseph R. Chambers, William P. Gilbert, and Luat T. Nguyen, eds., NASA CP-3149, Part 1, 1992, pp. 23 59.

8. Regenie, Victoria; Gatlin, Donald; Kempel, Robert; and Matheny, Neil: *The F-18 High Alpha Research Vehicle: A High Angle-of-Attack Testbed Aircraft.* NASA TM-104253, 1992.

9. Fisher, David F.; Del Frate, John H.; and Richwine, David M.: *In-Flight Flow Visualization Characteristics of the NASA F-18 High Alpha Research Vehicle at High Angles of Attack.* NASA TM-4193, 1990.

10. Fisher, David F.; Del Frate, John H.; and Zuniga, Fanny A.: *Summary of In-Flight Flow Visualization Obtained From the NASA High Alpha Research Vehicle.* NASA TM-101734, 1991.

11. Erickson, Gary E.: *Water Tunnel Flow Visualization and Wind Tunnel Data Analysis of the F/A-18.* NASA CR-165859, 1982.

12. Erickson, Gary E.: *Wind Tunnel Investigation of Vortex Flows on F/A-18 Configuration at Subsonic Through Transonic Speeds.* NASA TP-3111, 1991.

13. Banks, Daniel W.: Wind-Tunnel Investigation of the Forebody Aerodynamics of a Vortex-Lift Fighter Configuration at High Angles of Attack. Advanced Aerospace Aerodynamics, SP-757, SAE, Oct. 1988, pp. 101 123. (Available as SAE 881419.)

14. Hebbar, Sheshagiri K.; Platzer, Max F.; and Cavazos, Odilon V.: A Water Tunnel Investigation of the Effects of Pitch Rate and Yaw on LEX Generated Vortices of an F/A-18 Fighter Model. AIAA-91-0280, Jan. 1991.

15. Martin, C. A.; and Thompson, D. H.: Scale Model Measurements of Fin Buffet Due to Vortex Bursting on F/A-18. *Maneuvering Aerodynamics,* AGARD-CP-497, Nov. 1991, pp. 12-1 12-10.

16. Meyn, Larry A.; Lanser, Wendy R.; and James, Kevin D.: Full-Scale High Angle-of-Attack Tests of an F/A-18. AIAA-92-2676, June 1992.

17. Ghaffari, Farhad; Luckring, James M.; Thomas, James L.; and Bates, Brent L.: Navier-Stokes Solutions About the F/A-18 Forebody-LEX Configuration. AIAA-89-0338, Jan. 1989.

18. Thomas, James L.; Walters, Robert W.; Reu, Taekyu; Ghaffari, Farhad; Weston, Robert P.; and Luckring, James M.: A Patched-Grid Algorithm for Complex Configurations Directed Towards the F/A-18 Aircraft. AIAA-89-0121, Jan. 1989.

19. Benek, J. A.; Steger, J. L.; Dougherty, F. C.; and Buning, P. G.: *Chimera: A Grid-Embedding Technique.* NASA TM-89246, AEDC-TR-85-64, 1986. (Available from DTIC as AD A167 466.)

20. Schiff, Lewis B.; Cummings, Russell M.; Sorenson, Reese L.; and Rizk, Yehia M.: Numerical Simulation of High-Incidence Flow Over the F-18 Fuselage Forebody. AIAA-89-0339, Jan. 1989.

21. Cummings, Russell M.; Rizk, Yehia M.; Schiff, Lewis B.; and Chaderjian, Neal M.: Navier-Stokes Predictions of the Flowfield Around the F-18 (HARV) Wing and Fuselage at Large Incidence. AIAA-90-0099, Jan. 1990.

22. Rizk, Yehia M.; Schiff, Lewis B.; and Gee, Ken: Numerical Simulation of the Viscous Flow Around a Simplified F/A-18 at High Angles of Attack. AIAA-90-2999, 1990.

23. Rizk, Yehia M.; and Gee, Ken: Numerical Prediction of the Unsteady Flowfield Around the F-18 Aircraft at Large Incidence. AIAA-91-0020, Jan. 1991.

24. Ghaffari, Farhad; Luckring, James M.; Thomas, James L.; Bates, Brent L.; and Biedron, Robert T.: Multiblock Navier-Stokes Solutions About the F/A-18 Wing-LEX-Fuselage Configuration. *J. Aircr.,* vol. 30, no. 3, May–June 1993, pp. 293 303.

25. Smith, B. M.; Brauner, K. M.; Kennicott, P. R.; Liewald, M.; and Wellington, J.: *Initial Graphics Exchange Specification (IGES), Version 2.0.* NBSIR-82-2631-AF, Feb. 1983. (Available from NTIS as PB 83-137448.)

26. Brewer, J. A.; and Anderson, D. C.: Visual Interaction With Overhauser Curves and Surfaces. *Proceedings of the 4th Annual Conference on Computer Graphics and Interactive Techniques,* ASME, July 1977, pp. 132–137.

27. Ghaffari, Farhad; Luckring, James M.; Thomas, James L.; and Bates, Brent L.: Transonic Navier-Stokes Solutions About a Generic Hypersonic Configuration. *J. Aircr.,* vol. 28, no. 6, June 1991, pp. 381 388.

28. Luckring, James M.; Ghaffari, Farhad; and Bates, Brent L.: Status of Navier-Stokes Computations About the F/A-18 With Structured Grids. *High-Angle-of-Attack Technology*, Volume 1, Joseph R. Chambers, William P. Gilbert, and Luat T. Nguyen, eds., NASA CP-3149, Part 2, 1992, pp. 703–722.

29. Thomas, J. L.; Taylor, S. L.; and Anderson, W. K.: Navier-Stokes Computations of Vortical Flows Over Low Aspect Ratio Wings. AIAA-87-0207, Jan. 1987.

30. Vatsa, V. N.; Thomas, J. L.; and Wedan, B. W.: Navier-Stokes Computations of Prolate Spheroids at Angle of Attack. *Technical Papers—AIAA Atmospheric Flight Mechanics Conference*, Aug. 1987, pp. 488–506. (Available as AIAA-87-2627.)

31. Biedron, R. T.; and Thomas, J. L.: A Generalized Patched-Grid Algorithm With Application to the F-18 Forebody With Actuated Control Strake. *Comput. Sys. Eng.*, vol. 1, nos. 2–4, 1990, pp. 563–576.

32. Baldwin, Barrett; and Lomax, Harvard: Thin-Layer Approximation and Algebraic Model for Separated Turbulent Flows. AIAA-78-257, Jan. 1978.

33. Degani, David; and Schiff, Lewis B.: Computation of Supersonic Viscous Flows Around Pointed Bodies at Large Incidence. AIAA-83-0034, Jan. 1983.

34. Roe, P. L.: Characteristic-Based Schemes for the Euler Equations. *Annual Review of Fluid Mechanics*, Volume 18, Milton van Dyke, J. V. Wehausen, and John L. Lumley, eds., Annual Reviews Inc., 1986, pp. 337–365.

35. Van Leer, Bram: Upwind-Difference Methods for Aerodynamic Problems Governed by the Euler Equations. *Large-Scale Computations in Fluid Mechanics,* Bjorn E. Engquist, Stanley Osher, and Richard C. J. Somerville, eds., American Math. Soc., 1985, pp. 327–336.

36. Fox, Charles H., Jr.; and Huffman, Jarrett K.: *Calibration and Test Capabilities of the Langley 7- by 10-Foot High-Speed Tunnel.* NASA TM X-74027, 1977.

37. Fox, Charles H., Jr.: *Real Time Data Reduction Capabilities at the Langley 7- by 10-Foot High-Speed Tunnel.* NASA TM-78801, 1980.

38. Braslow, A. L.; and Knox, E. C.: *Simplified Method for Determination of Critical Height of Distributed Roughness Particles for Boundary-Layer Transition at Mach Numbers From 0 to 5.* NACA TN 4363, 1958.

39. Herriot, John G.: *Blockage Corrections for Three-Dimensional-Flow Closed-Throat Wind Tunnels, With Consideration of the Effect of Compressibility.* NACA Rep. 995, 1950. (Supersedes NACA RM A7B28.)

40. Gillis, Clarence L.; Polhamus, Edward C.; and Gary, Joseph L., Jr.: *Charts for Determining Jet-Boundary Corrections for Complete Models in 7- by 10-Foot Closed Rectangular Wind Tunnels.* NACA WR L-123, 1945. (Formerly NACA ARR L5G31.)

41. Sellers, William L., III; and Kjelgaard, Scott O.: The Basic Aerodynamics Research Tunnel—A Facility Dedicated to Code Validation. AIAA-88-1997, May 1988.

42. Fisher, David F.; and Meyer, Robert R., Jr.: *Flow Visualization Techniques for Flight Research.* NASA TM-100455, 1988.

43. Hartwich, Peter-M.; Hsu, C.-H.; Luckring, James M.; and Liu, C. H.: Numerical Study of the Vortex Burst Phenomenon for Delta Wings. AIAA-88-0505, Jan. 1988.

44. Vatsa, Veer N.; Sanetrik, Mark D.; and Parlette, Edward B.: Development of a Flexible and Efficient Multigrid-Based Multiblock Flow Solver. AIAA-93-0677, Jan. 1993.

45. Degani, David; Schiff, Lewis B.; and Levy, Yuval: Physical Considerations Governing Computation of Turbulent Flows Over Bodies at Large Incidence. AIAA-90-0096, Jan. 1990.

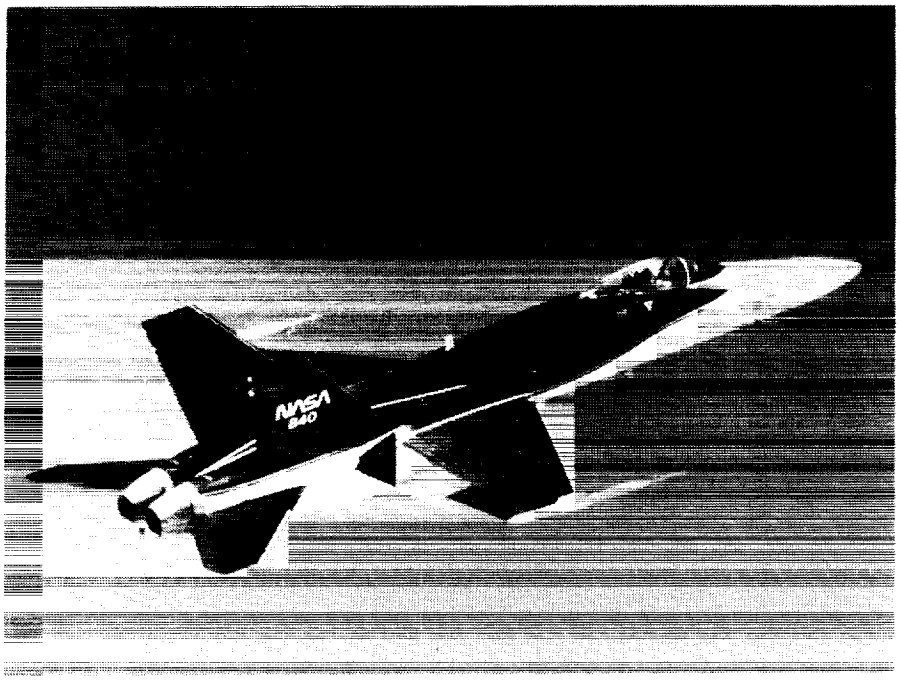

L-91-65

Figure 1. The F/A-18 High-Alpha Research Vehicle (HARV).

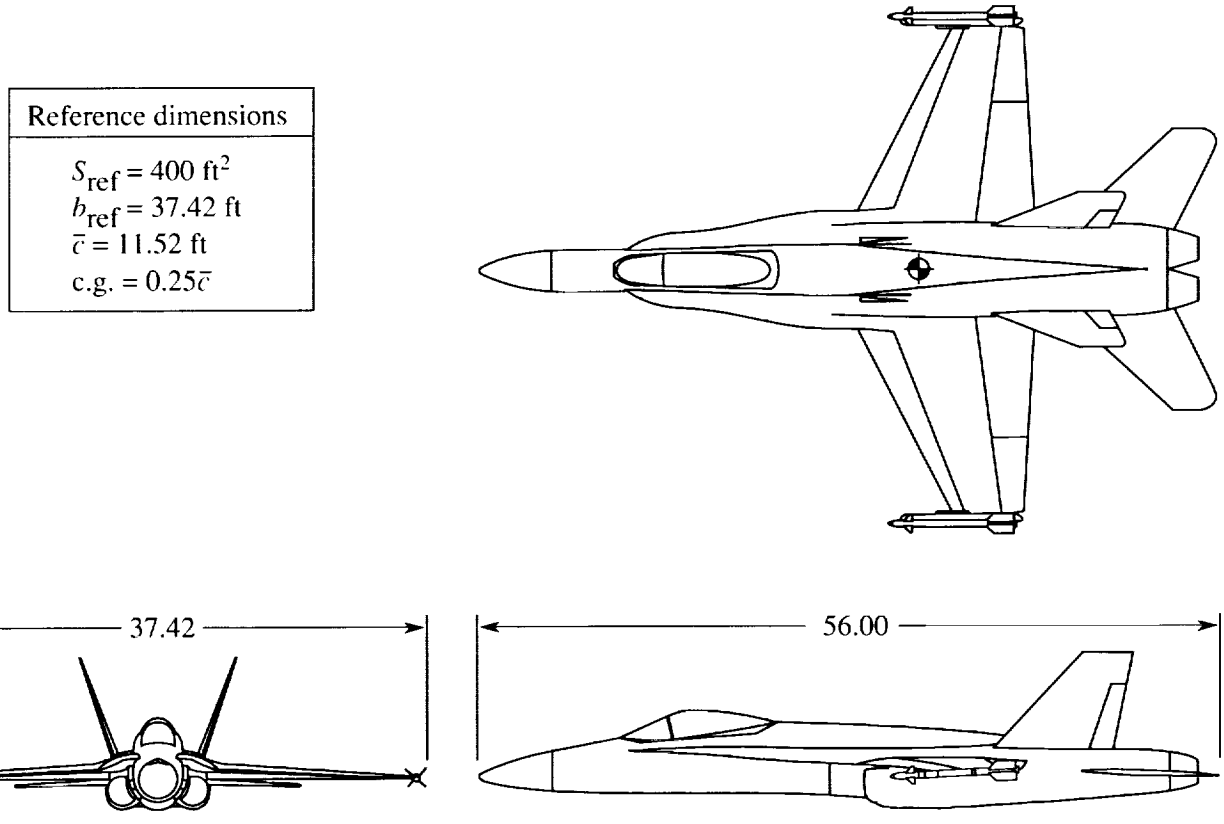

Figure 2. The F/A-18 aircraft geometry. All linear dimensions are in feet.

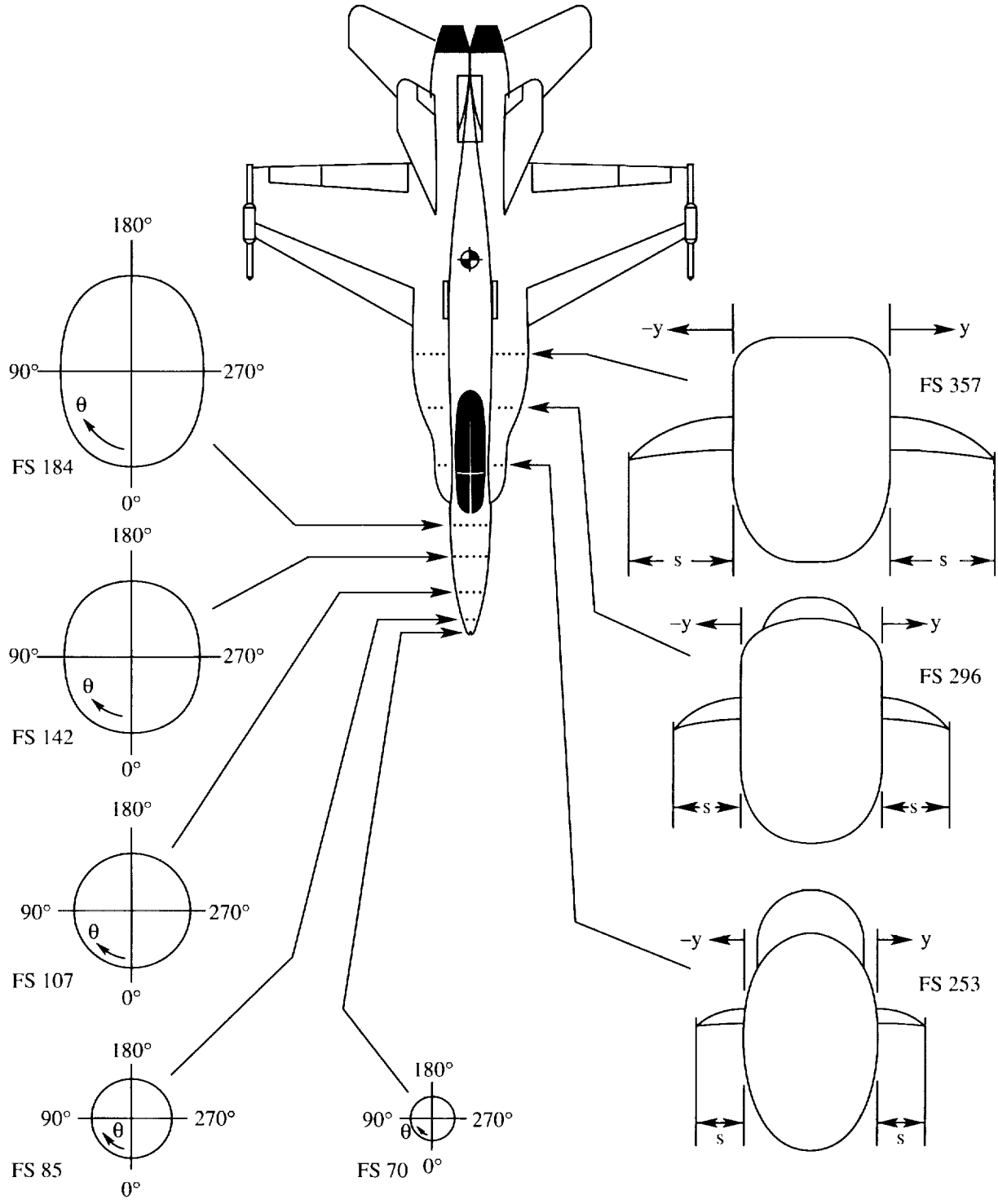

Figure 3. Planform of F/A-18 aircraft with forebody and LEX-fuselage cross-sectional pressure measurement stations.

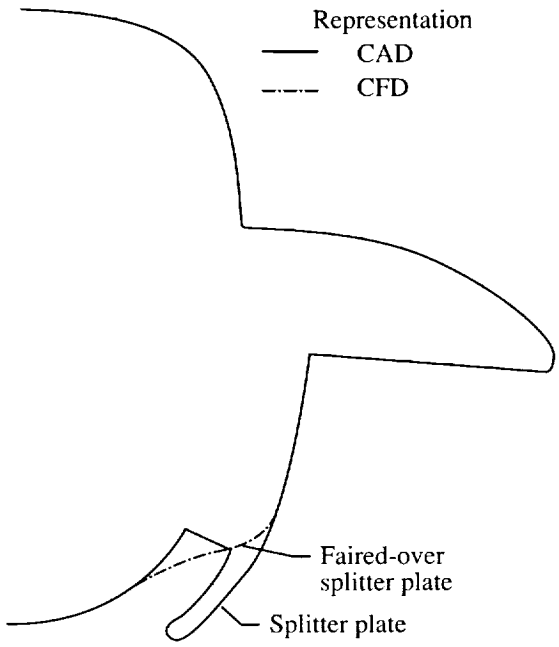

(a) FS 401.

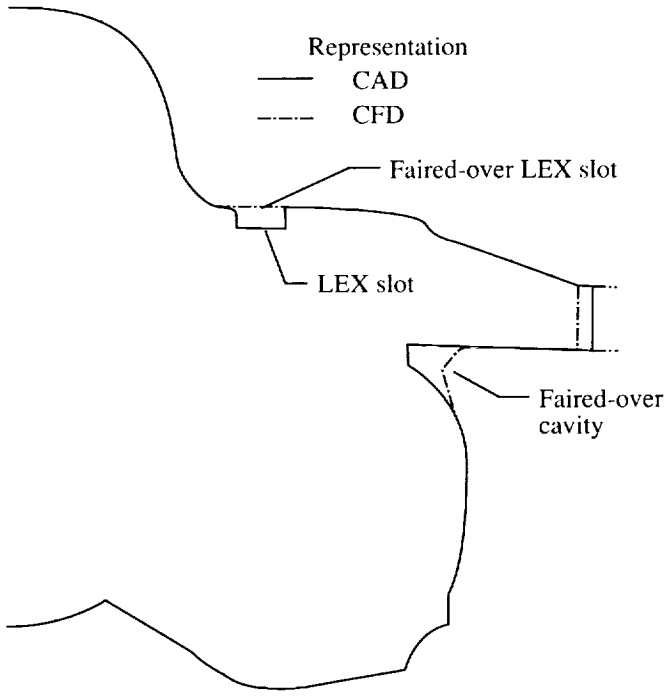

(b) FS 441.

Figure 4. Typical CAD and CFD cross-sectional grids.

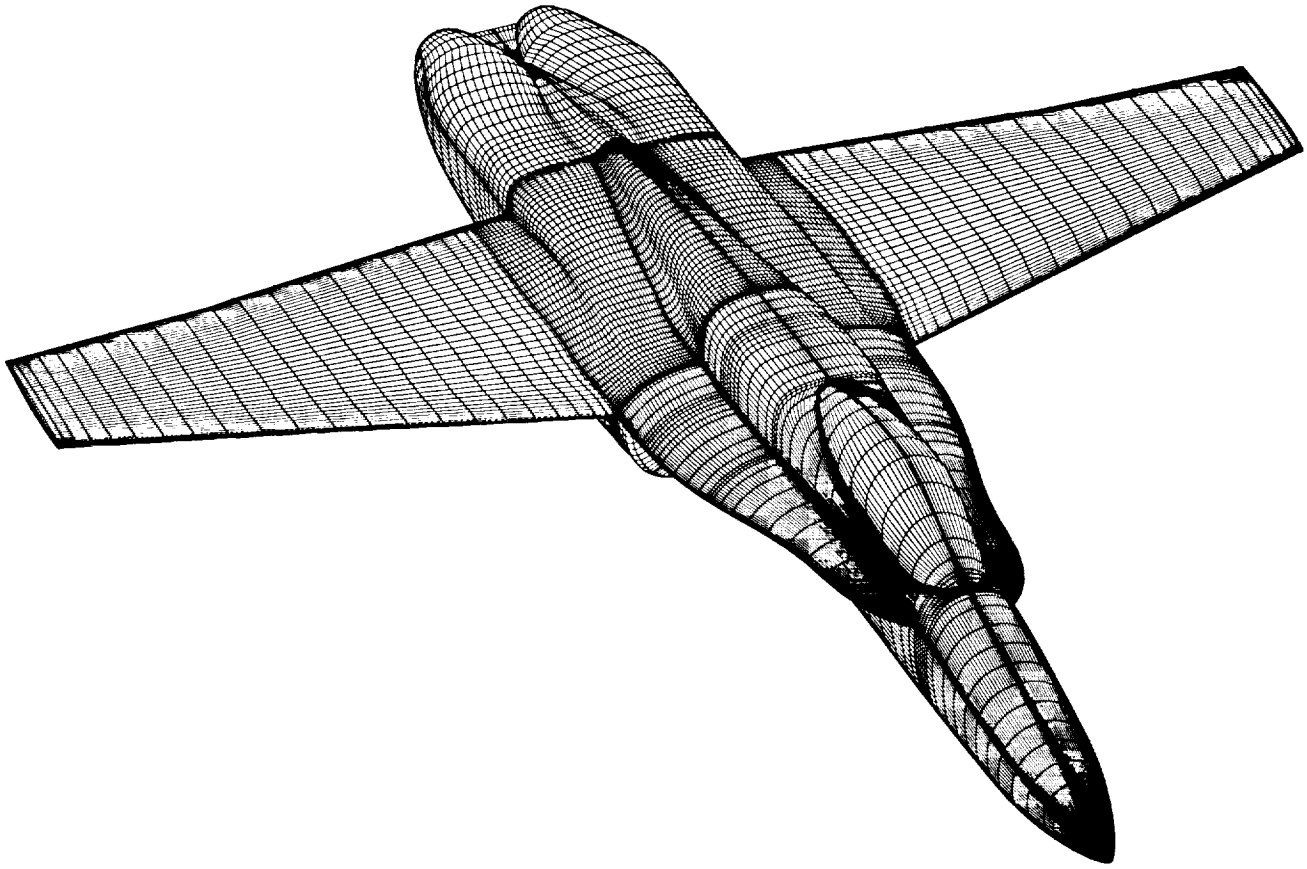

(a) Oblique top view.

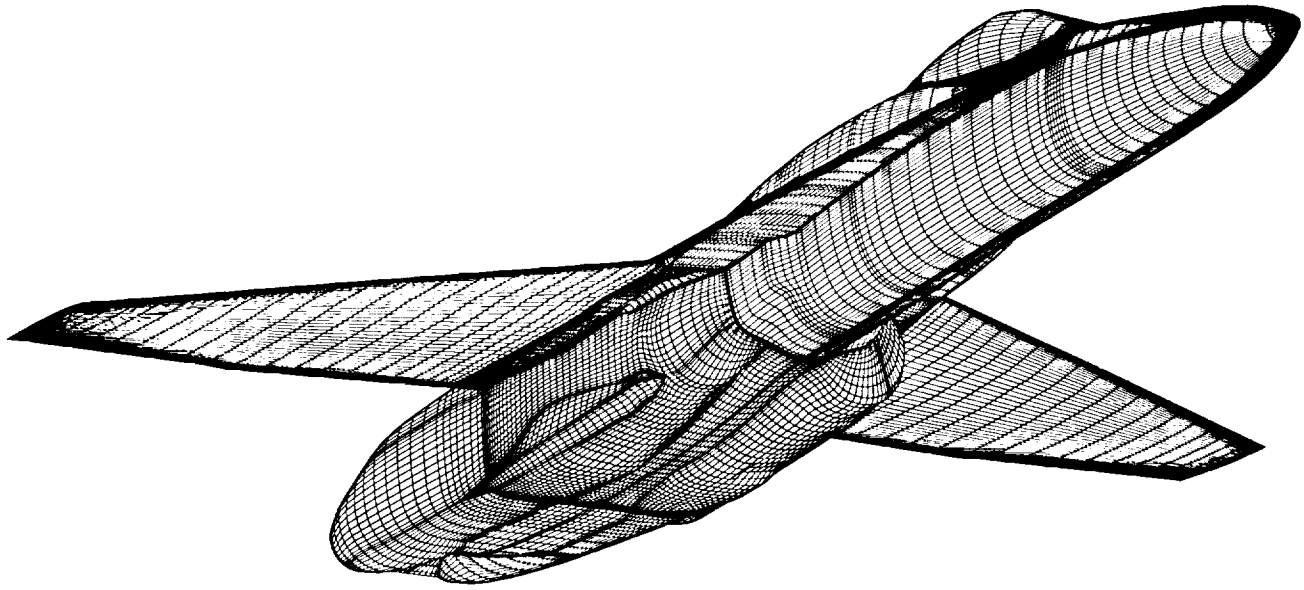

(b) Oblique bottom view.

Figure 5. The F/A-18 aircraft CFD surface grid representation.

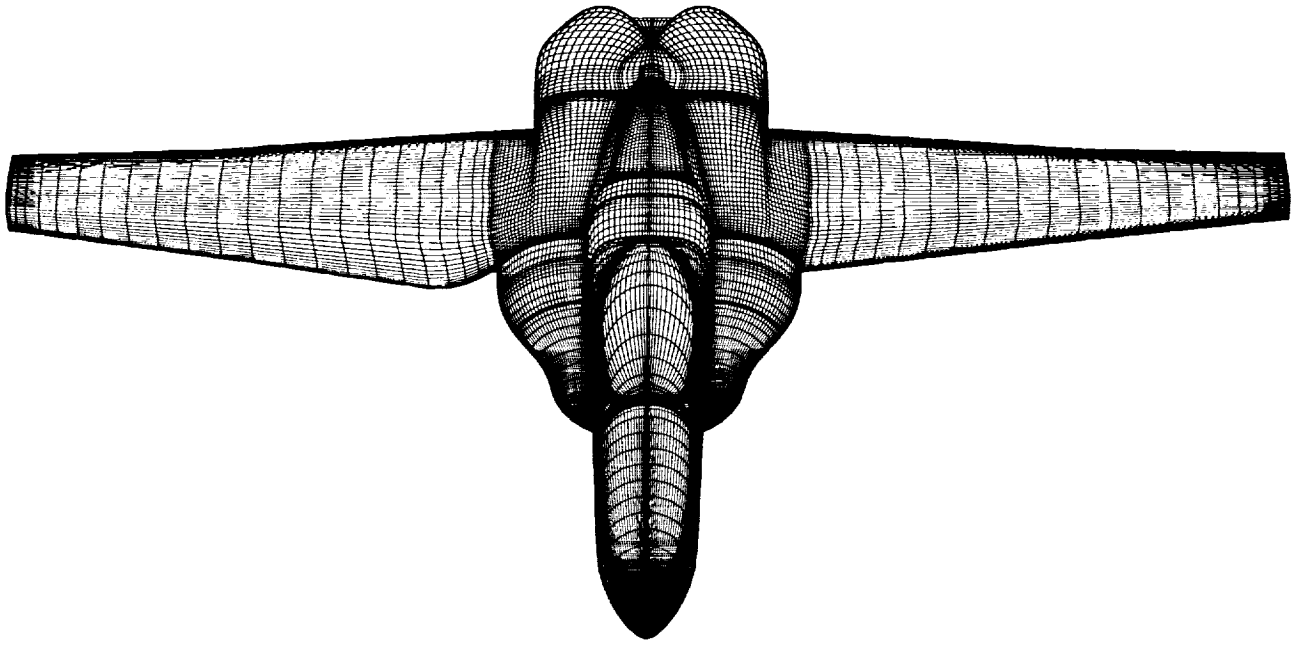

Figure 6. The F/A-18 aircraft CFD surface grid with undeflected (port) and blended (starboard) flaps.

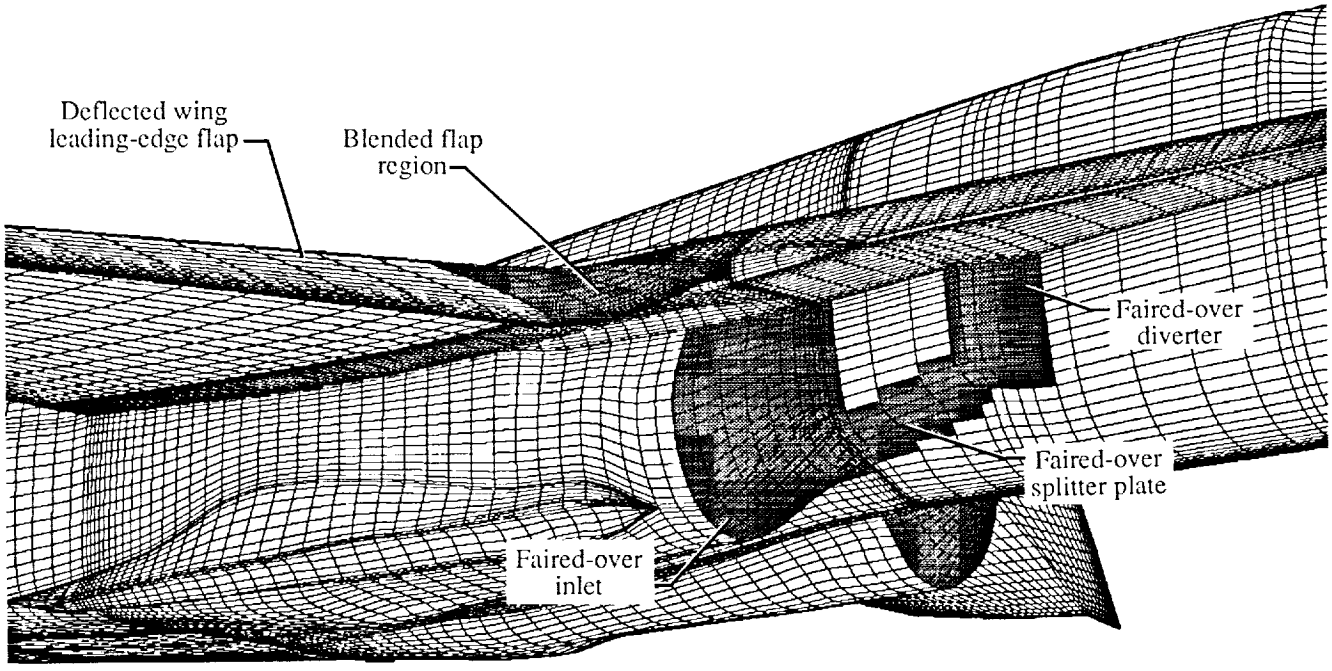

Figure 7. Close-up of F/A-18 aircraft CFD surface grid and highlighted surface modifications.

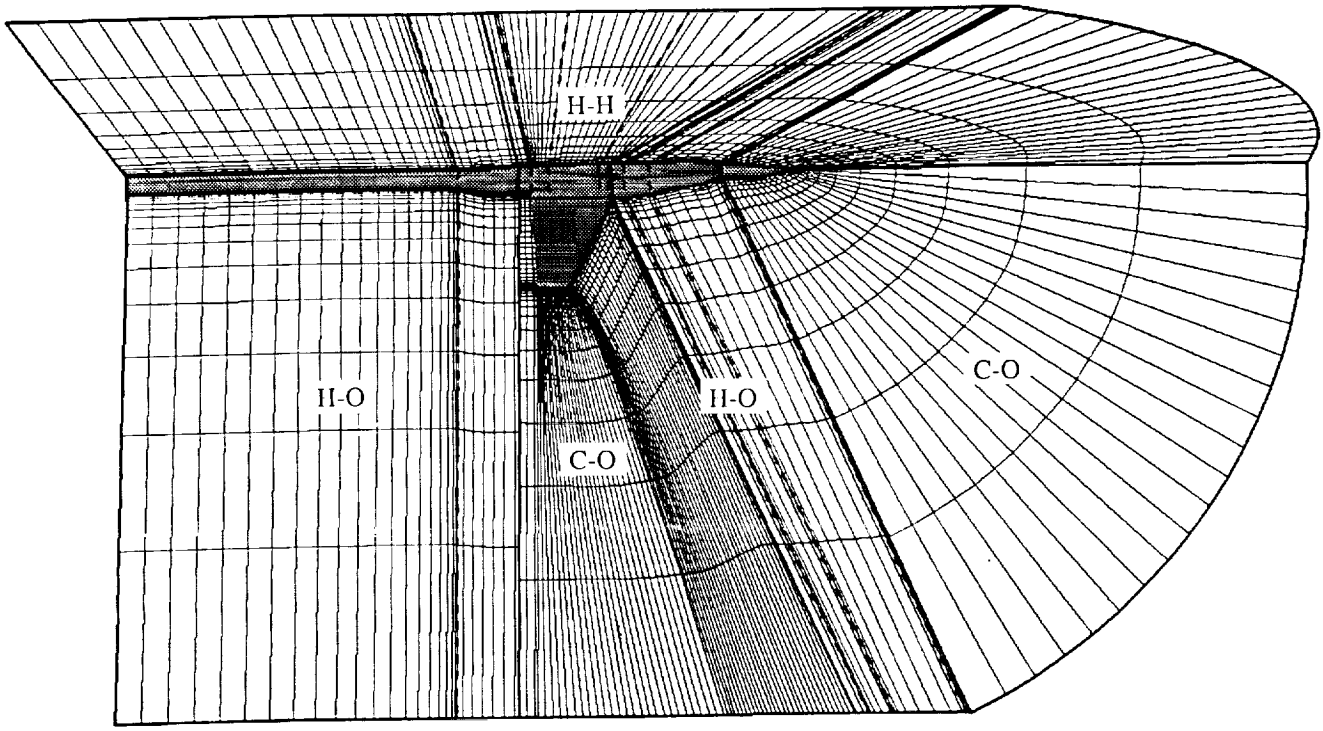

(a) Far field.

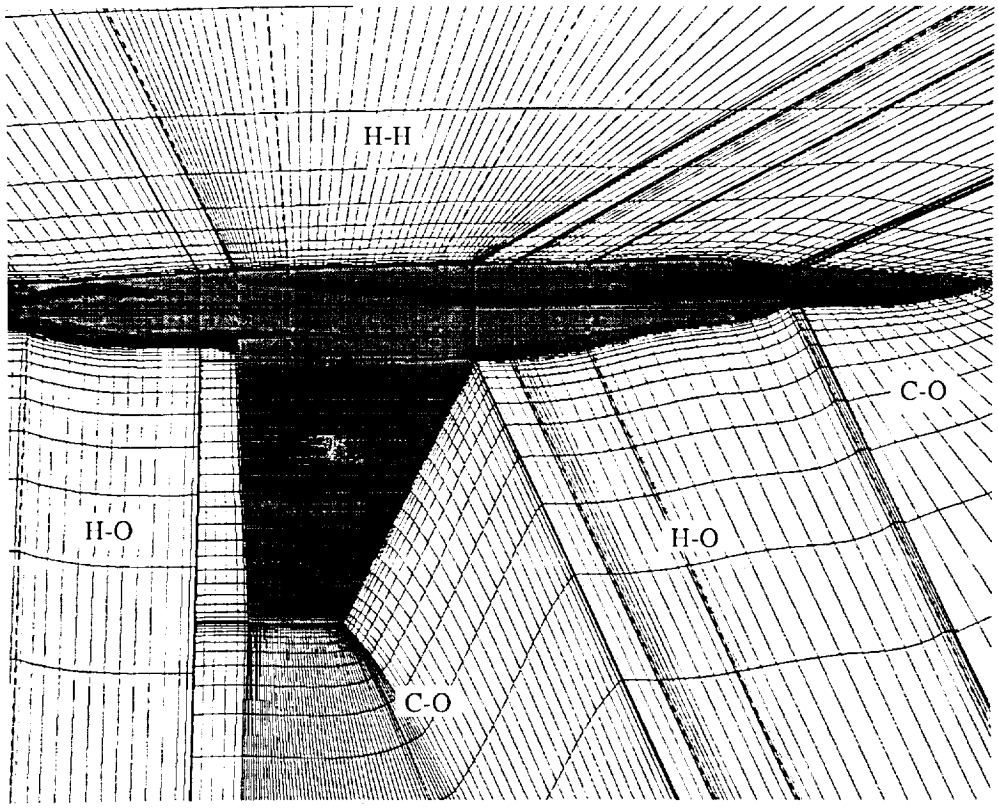

(b) Near field.

Figure 8. The F/A-18 aircraft flow-field blocking strategy.

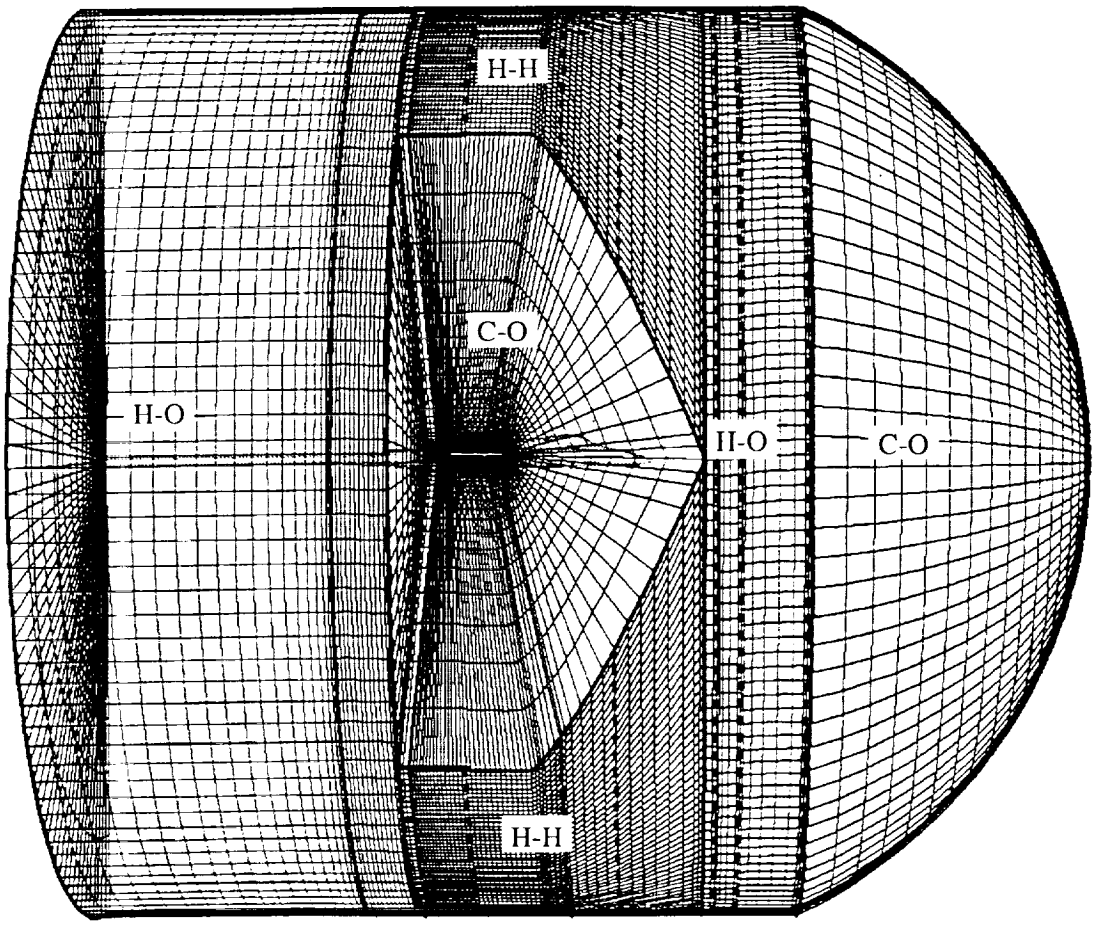

Figure 9. Far-field sideview of F/A-18 aircraft flow-field blocking strategy.

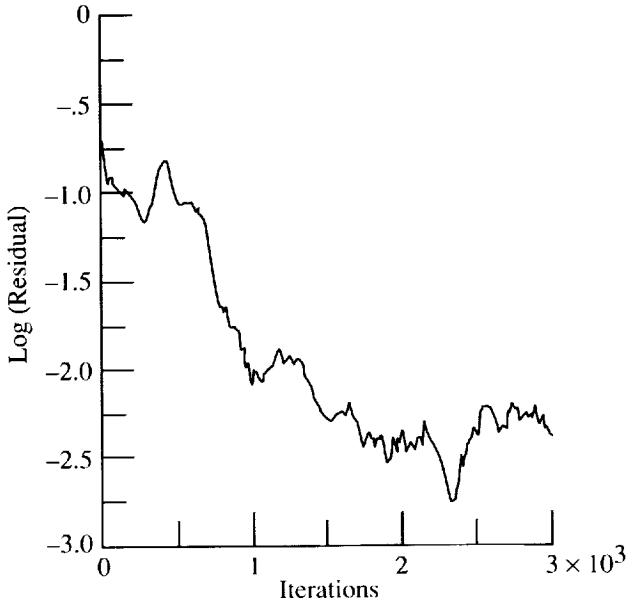

(a) Residual convergence.

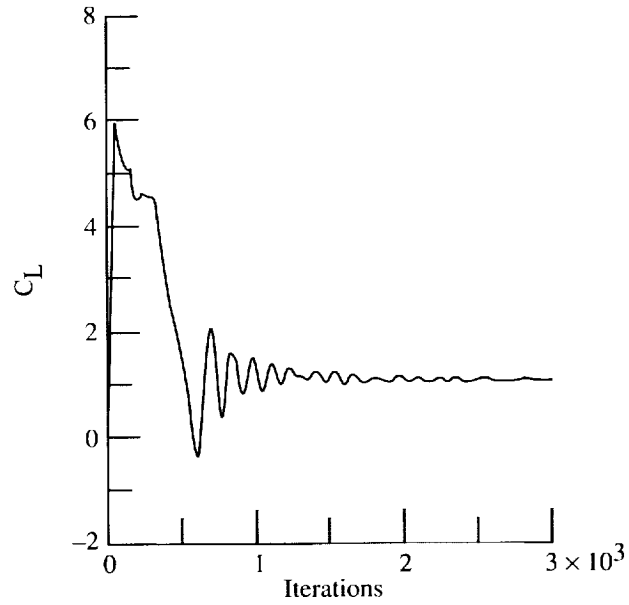

(b) C_L convergence.

Figure 10. Typical convergence characteristics. $\alpha = 19°$; $M_\infty = 0.34$; $R_c = 13.5 \times 10^6$; $\delta_f = 0°$.

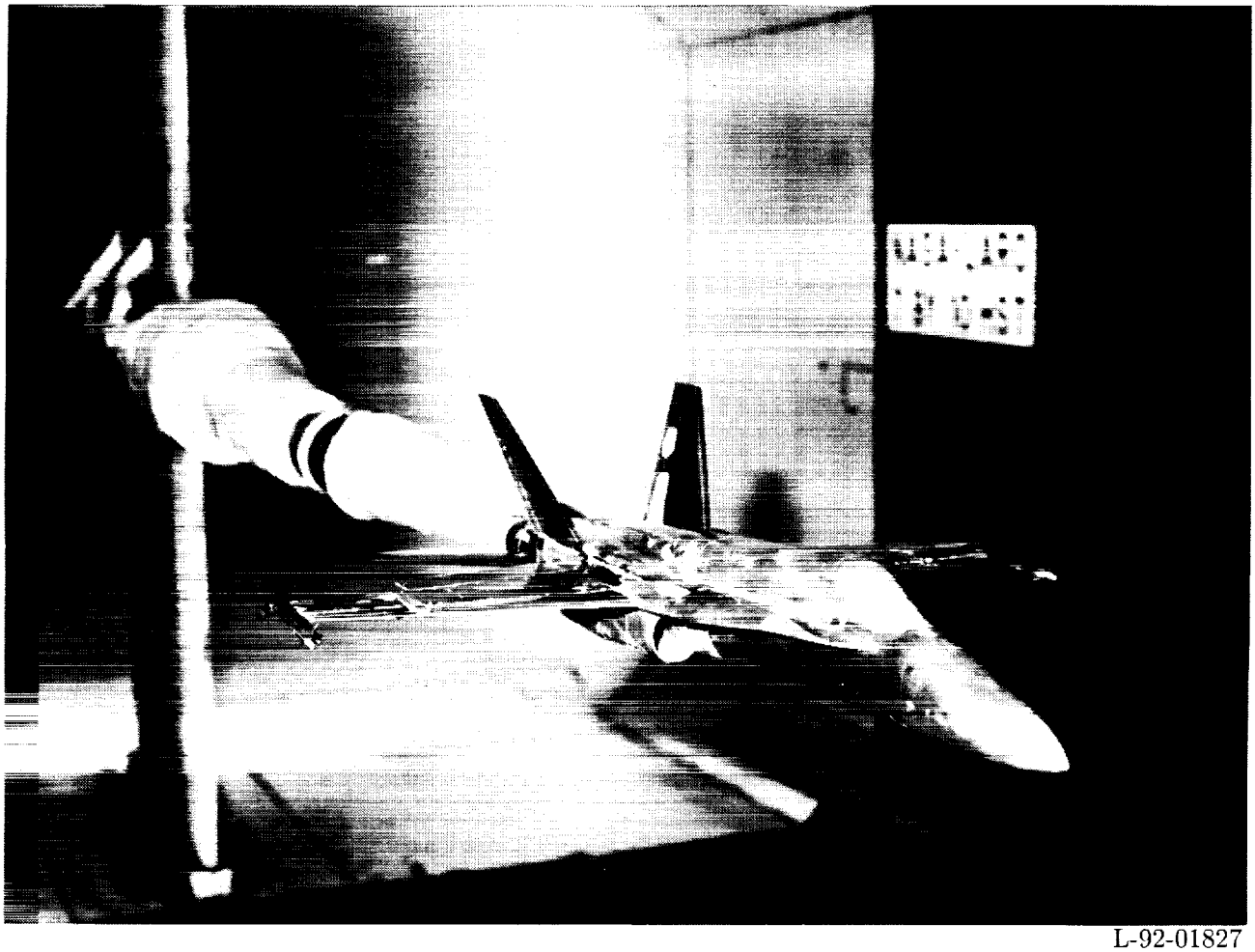

L-92-01827

Figure 11. Sting-mounted 0.06-scale F/A-18 aircraft wind tunnel model.

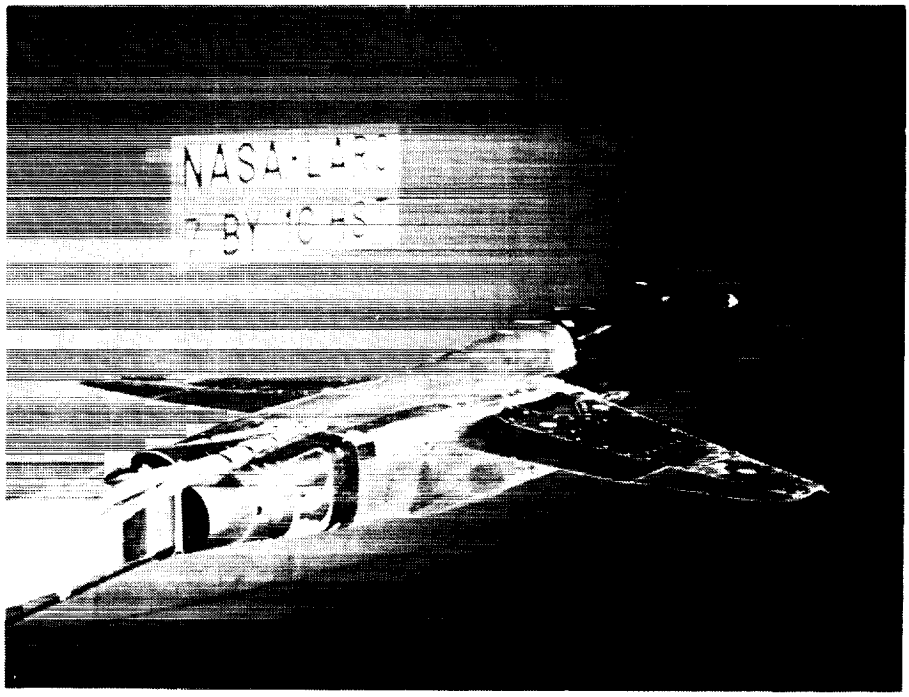

L-92-2805

(a) Oblique rear view.

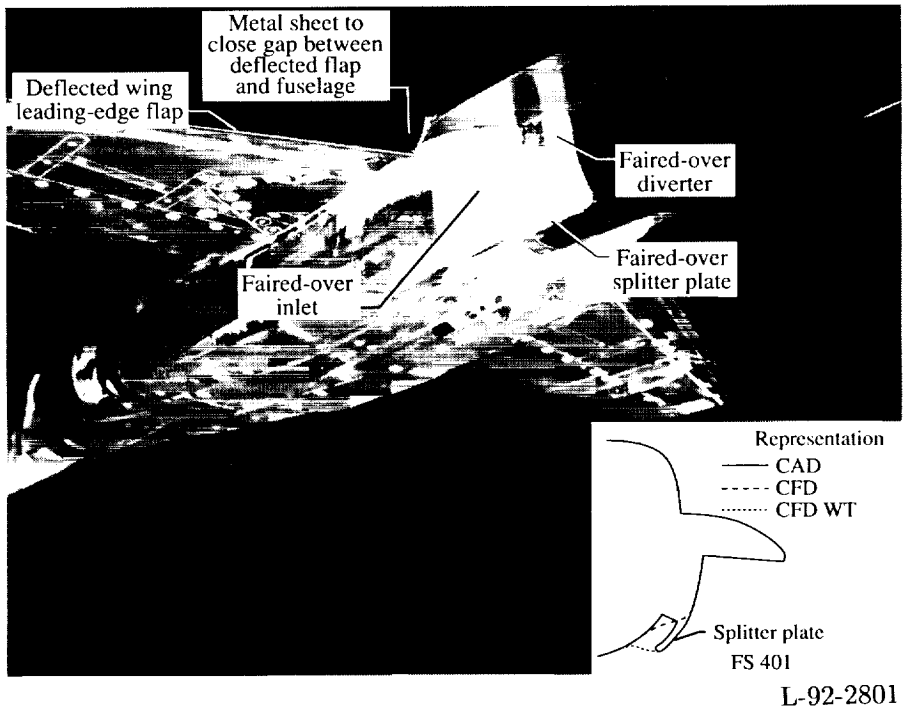

L-92-2801

(b) Close-up of geometrical modifications.

Figure 12. Sting-mounted 0.06-scale F/A-18 aircraft CFD wind tunnel model.

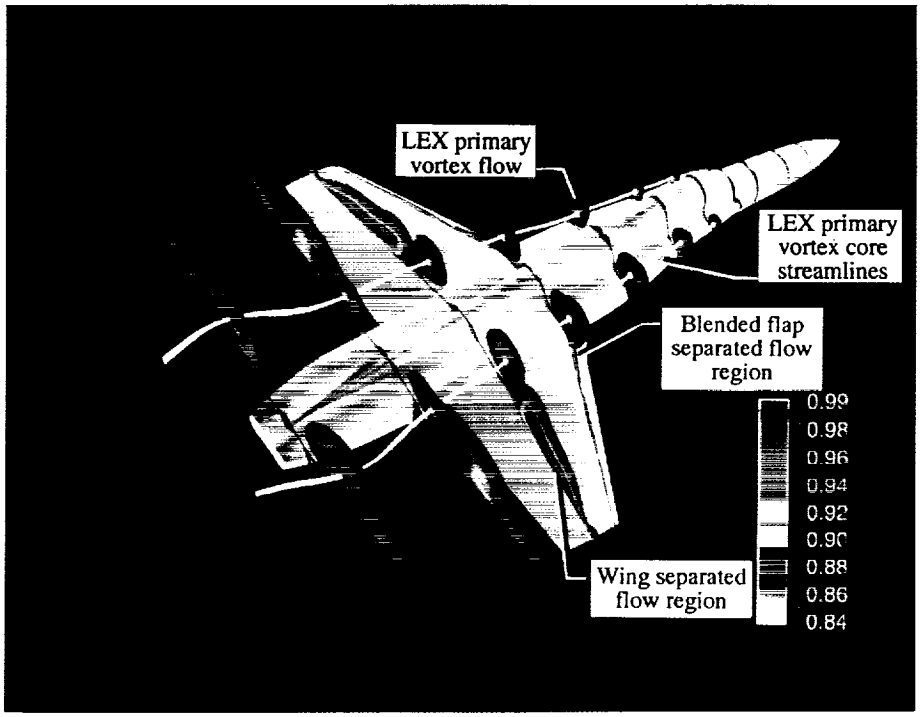

(a) $\alpha = 19°; M_\infty = 0.34; R_{\bar{c}} = 13.5 \times 10^6; \delta_f = 25°$.

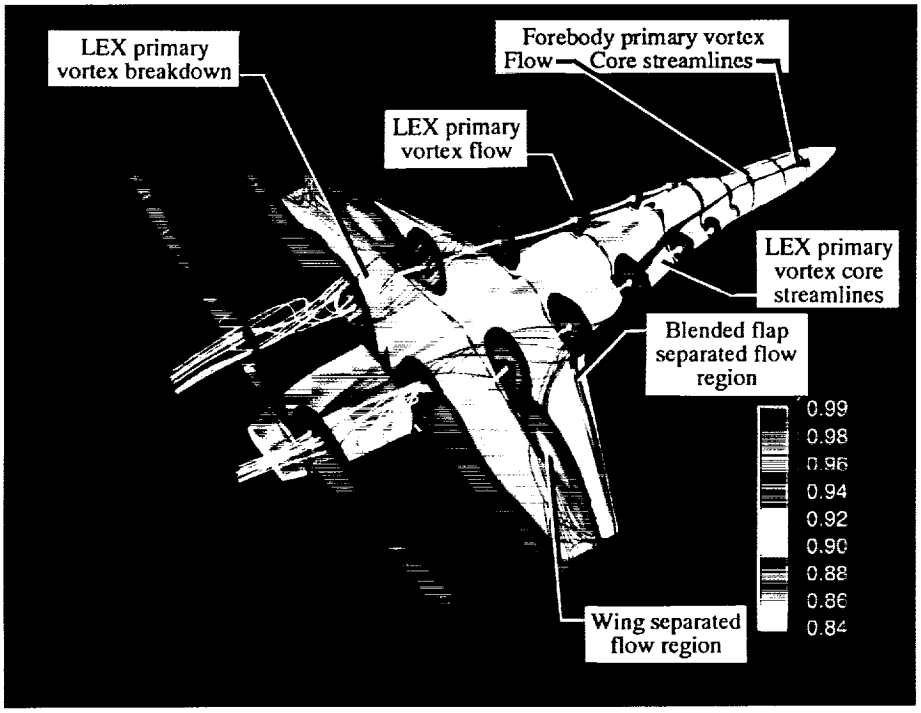

(b) $\alpha = 25.8°; M_\infty = 0.25; R_{\bar{c}} = 10.8 \times 10^6; \delta_f = 25°$.

Figure 13. Cross-flow normalized total pressure contours with vortex core particle traces.

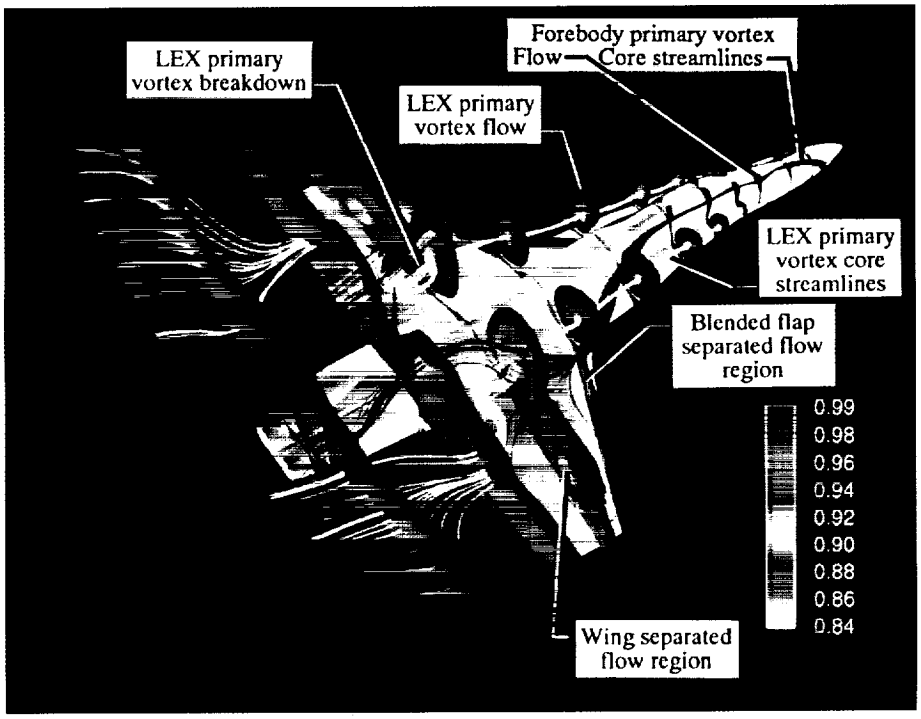

(c) $\alpha = 30.3°$; $M_\infty = 0.24$; $R_{\bar{c}} = 10.2 \times 10^6$; $\delta_f = 25°$.

Figure 13. Concluded.

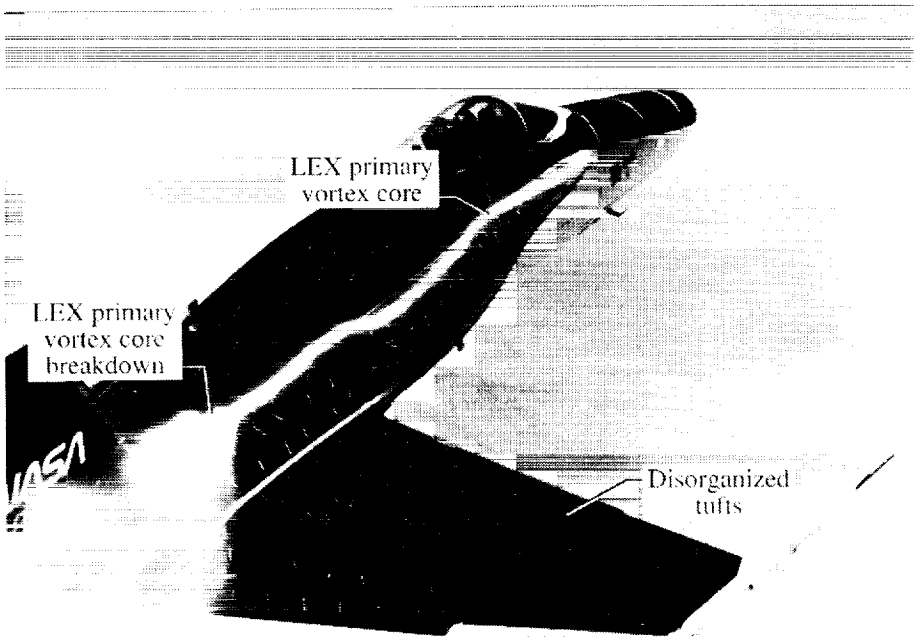

(a) $\alpha \approx 20°; M_\infty \approx 0.3; R_{\bar{c}} \approx 10 \times 10^6; \delta_f \approx 25°$.

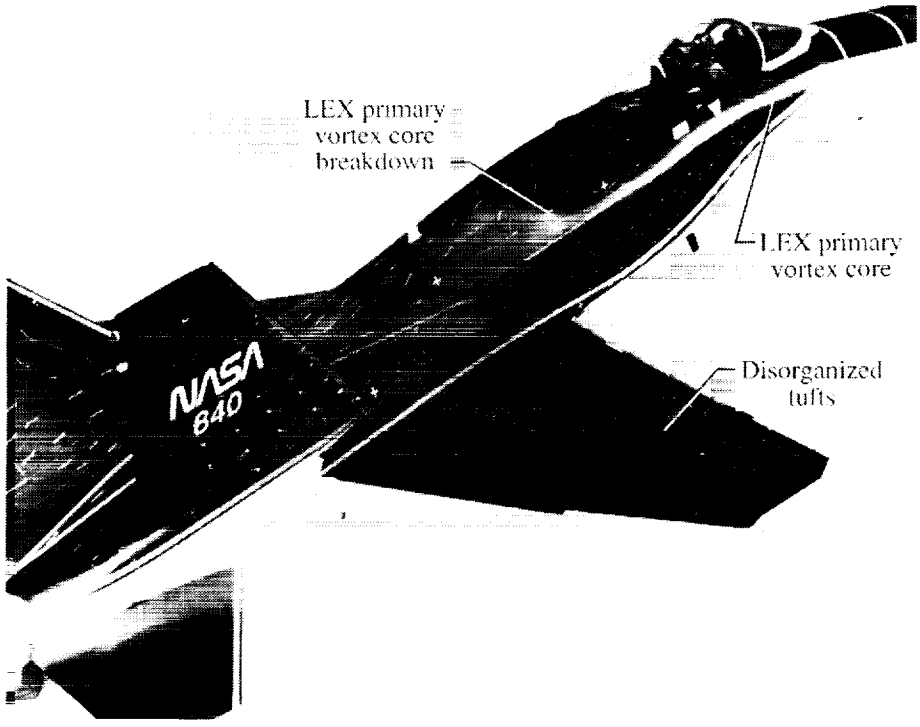

(b) $\alpha \approx 25°; M_\infty \approx 0.3; R_{\bar{c}} \approx 10 \times 10^6; \delta_f \approx 34°$.

Figure 14. The HARV in-flight surface and off-surface flow visualization.

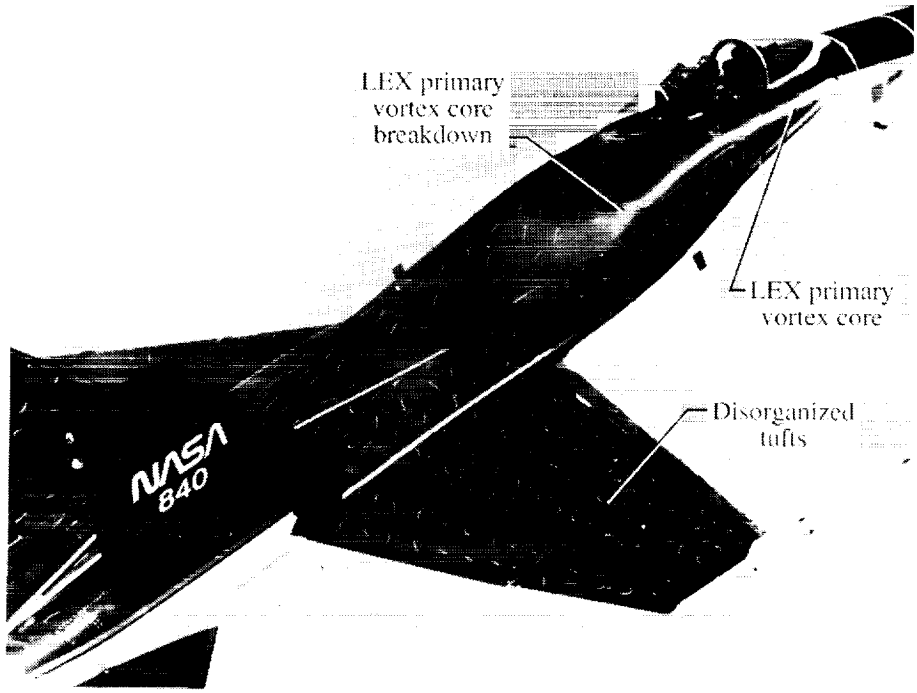

(c) $\alpha \approx 30°$; $M_\infty \approx 0.3$; $R_{\bar{c}} \approx 10 \times 10^6$; $\delta_f \approx 34°$.

Figure 14. Concluded.

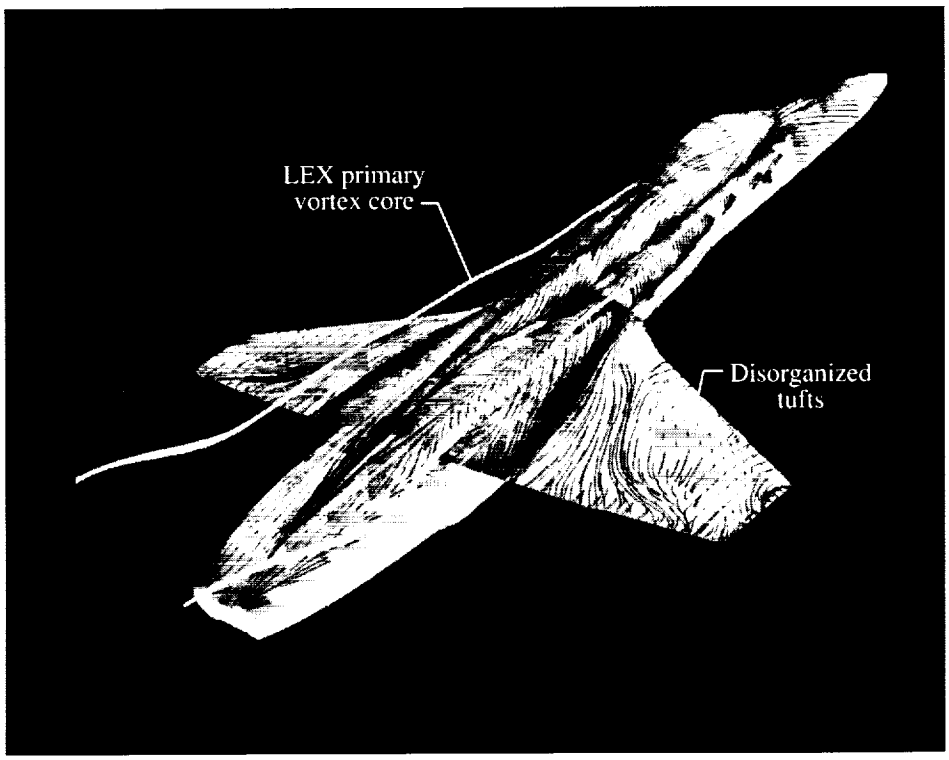

(a) $\alpha = 19°; M_\infty = 0.34; R_{\bar{c}} = 13.5 \times 10^6; \delta_f = 25°$.

Figure 15. Unrestricted surface flow pattern with vortex core particle traces.

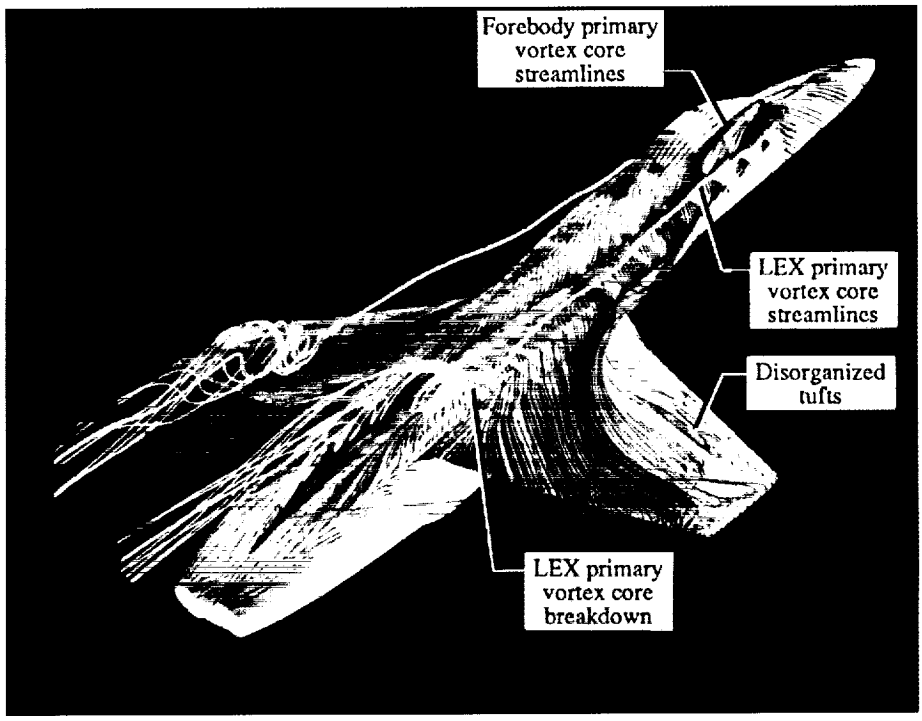

(b) $\alpha = 25.8°; M_\infty = 0.25; R_{\bar{c}} = 10.8 \times 10^6; \delta_f = 25°$.

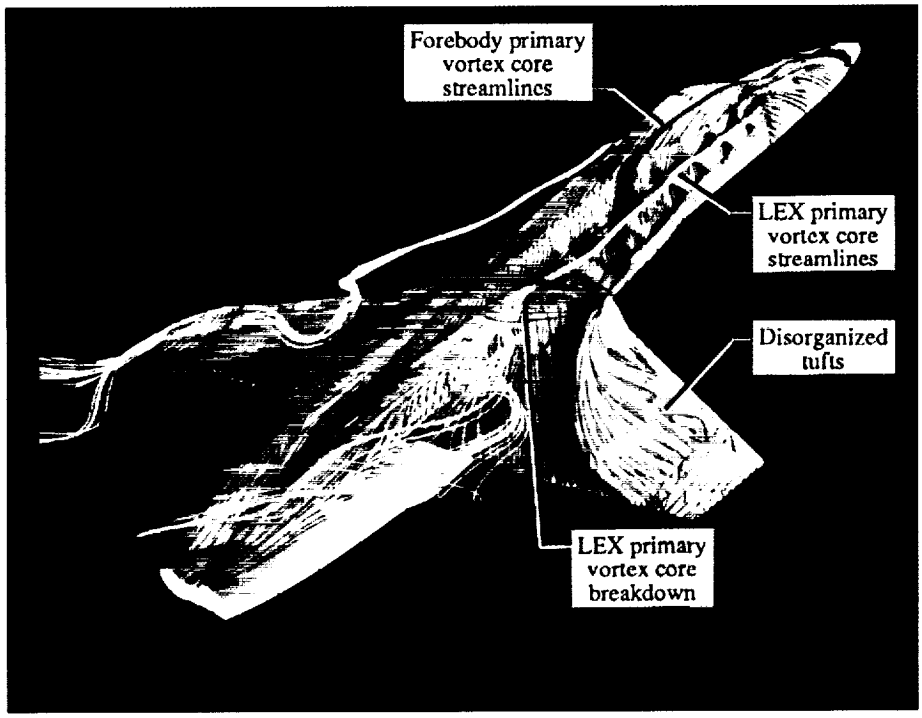

(c) $\alpha = 30.3°; M_\infty = 0.24; R_{\bar{c}} = 10.2 \times 10^6; \delta_f = 25°$.

Figure 15. Concluded.

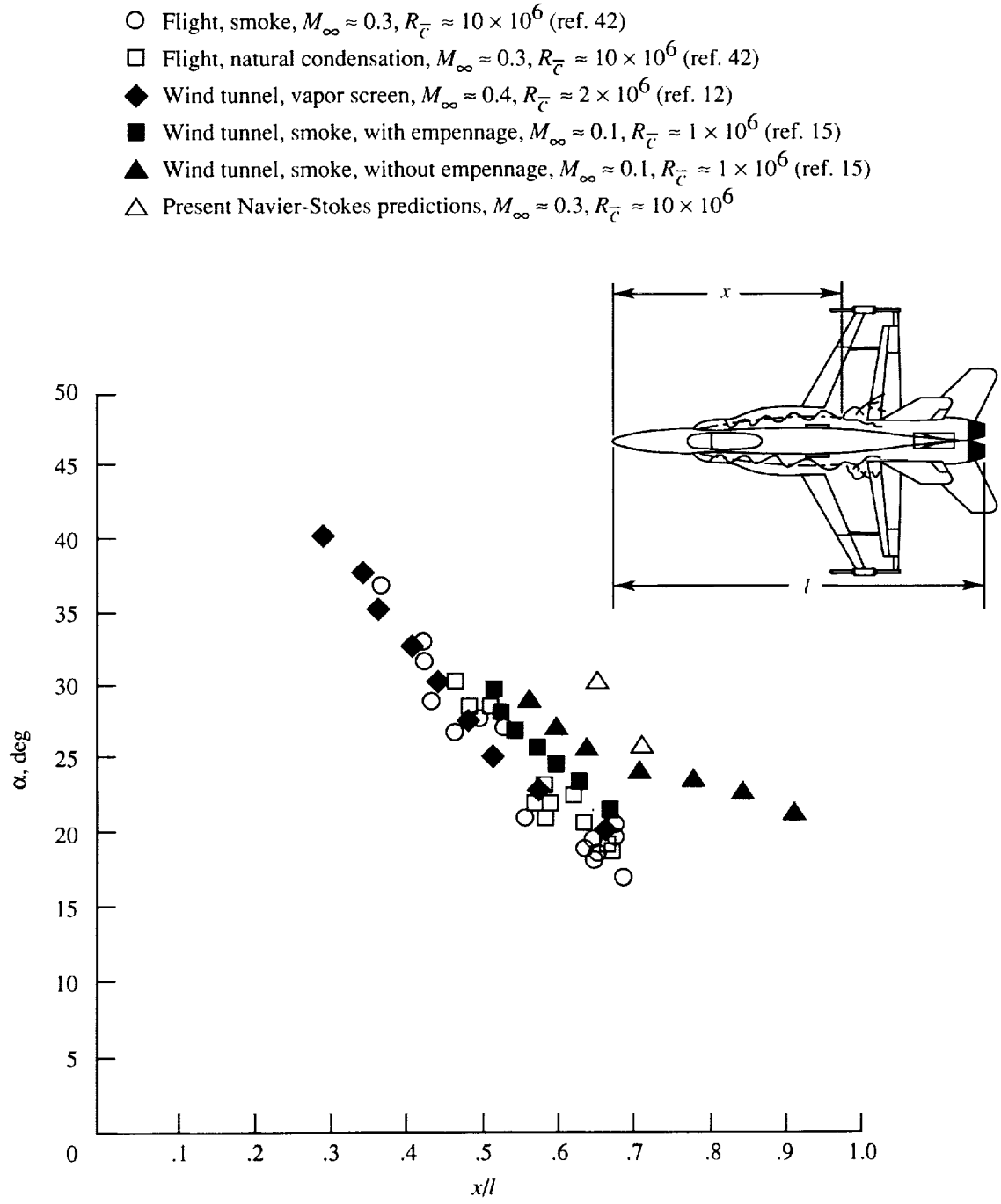

Figure 16. LEX primary vortex-breakdown correlations between flight, wind tunnel, and computational results.

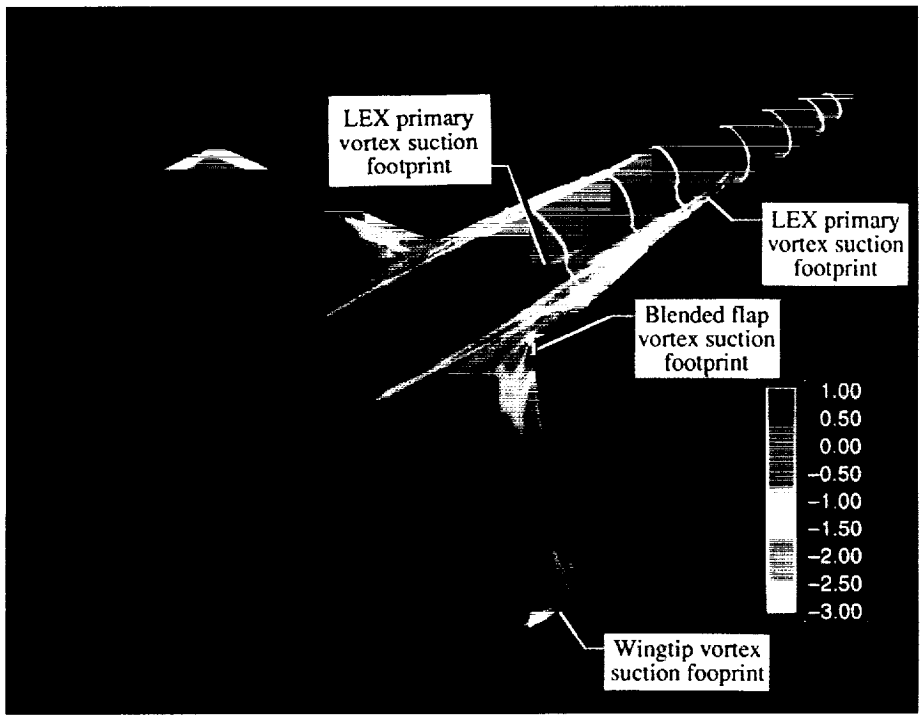

(a) $\alpha = 19°; M_\infty = 0.34; R_{\bar{c}} = 13.5 \times 10^6; \delta_f = 25°$.

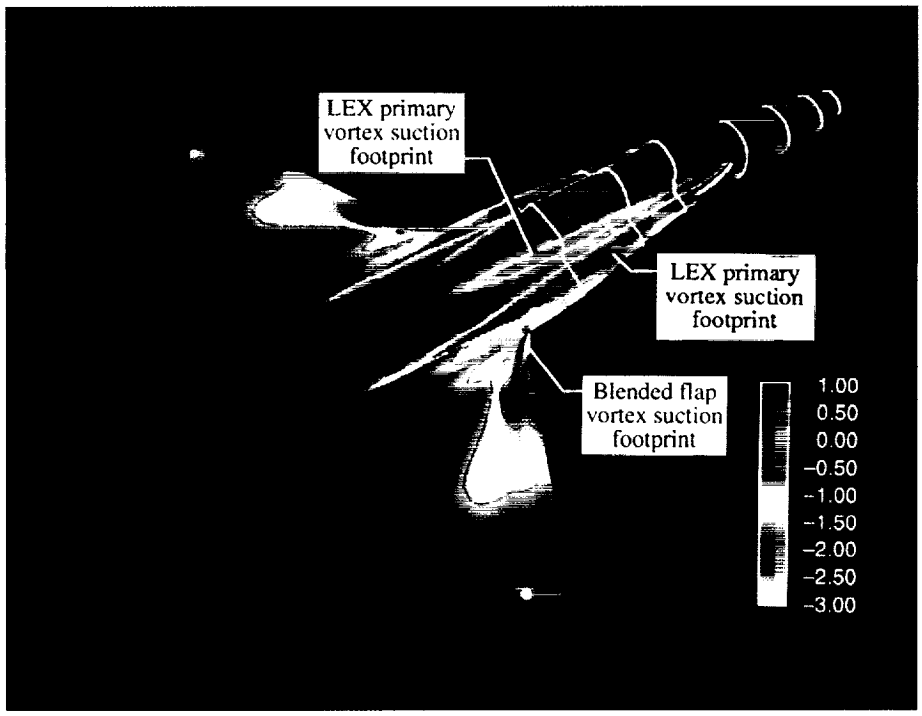

(b) $\alpha = 25.8°; M_\infty = 0.25; R_{\bar{c}} = 10.8 \times 10^6; \delta_f = 25°$.

Figure 17. Computed surface pressure coefficients.

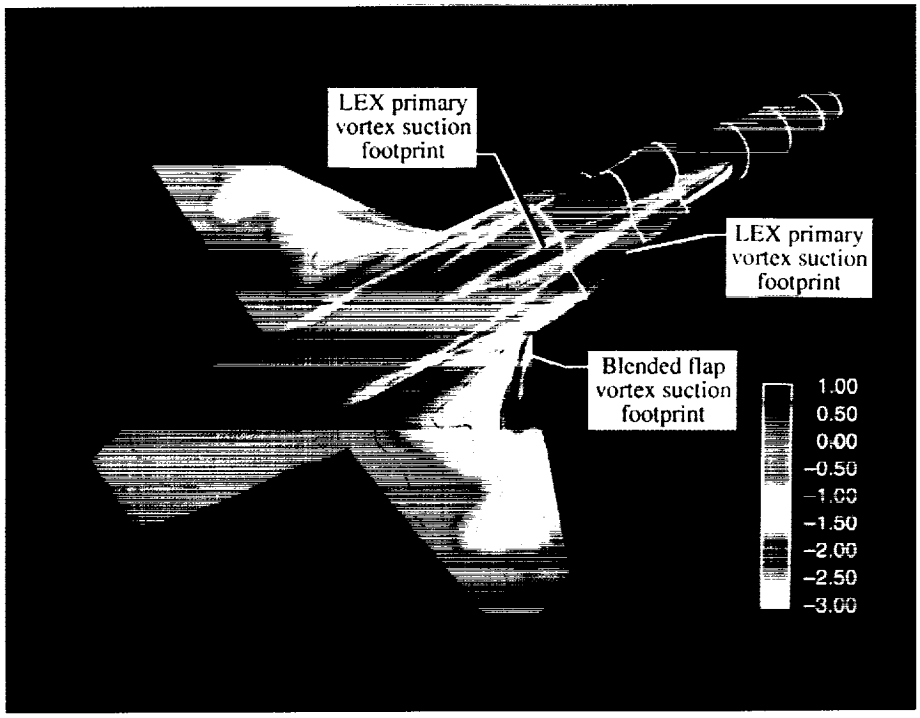

(c) $\alpha = 30.3°$; $M_\infty = 0.24$; $R_{\bar{c}} = 10.2 \times 10^6$; $\delta_f = 25°$.

Figure 17. Concluded.

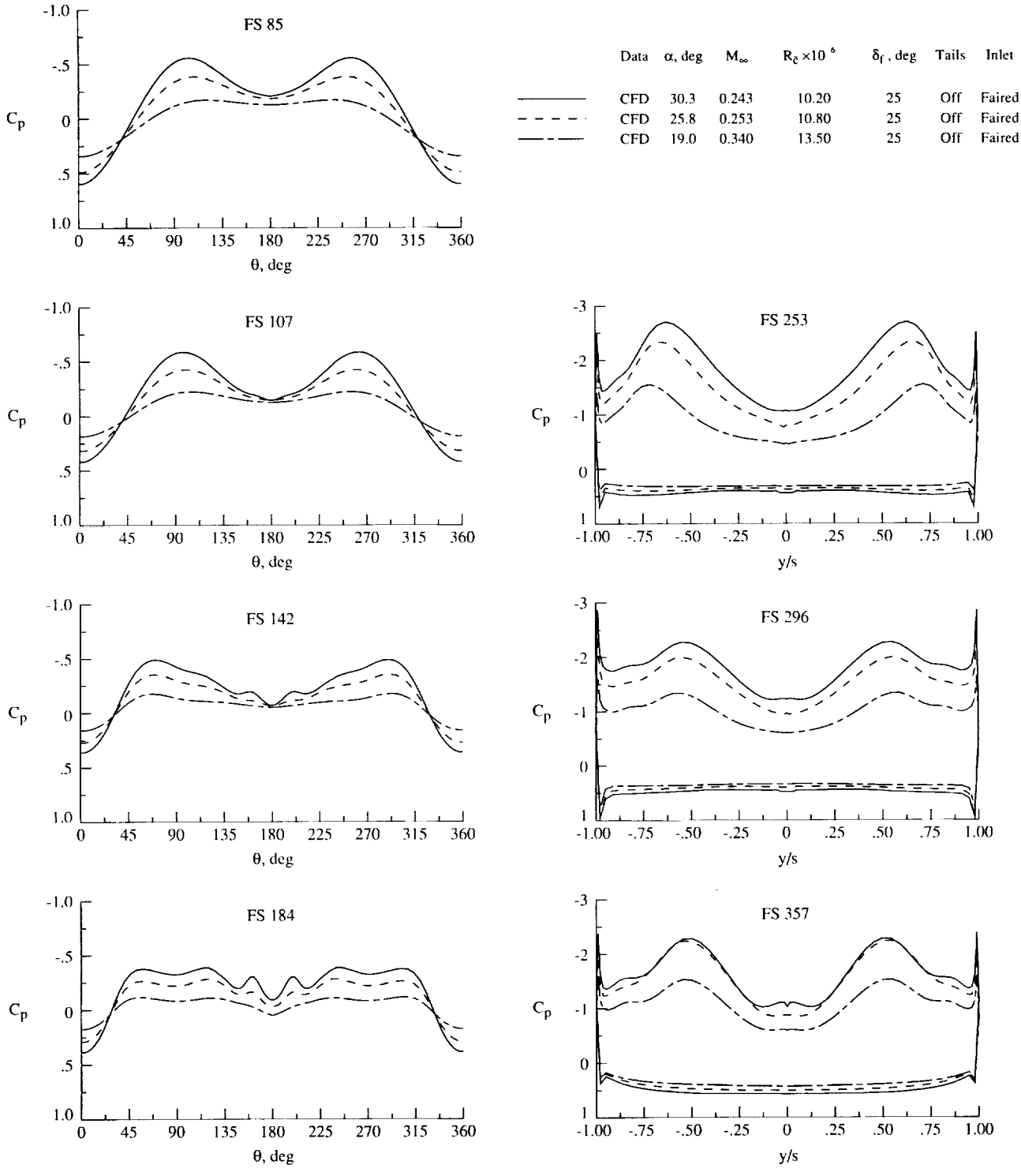

(a) Forebody. (b) LEX.

Figure 18. Effect of angle of attack on computed surface pressure coefficients.

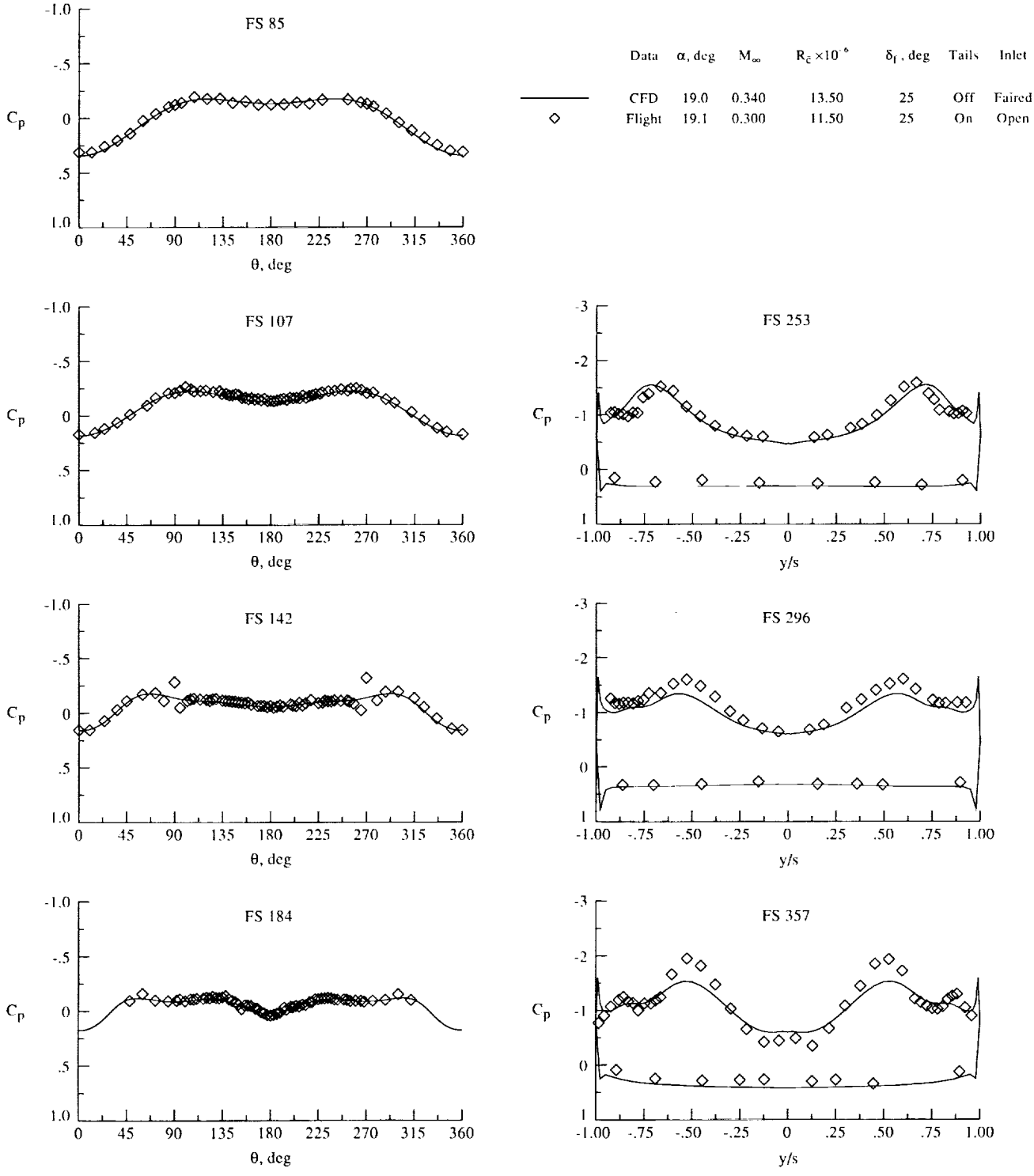

(a) Forebody. (b) LEX.

Figure 19. Correlation of computed surface pressure coefficients with flight data at $\alpha \approx 19°$.

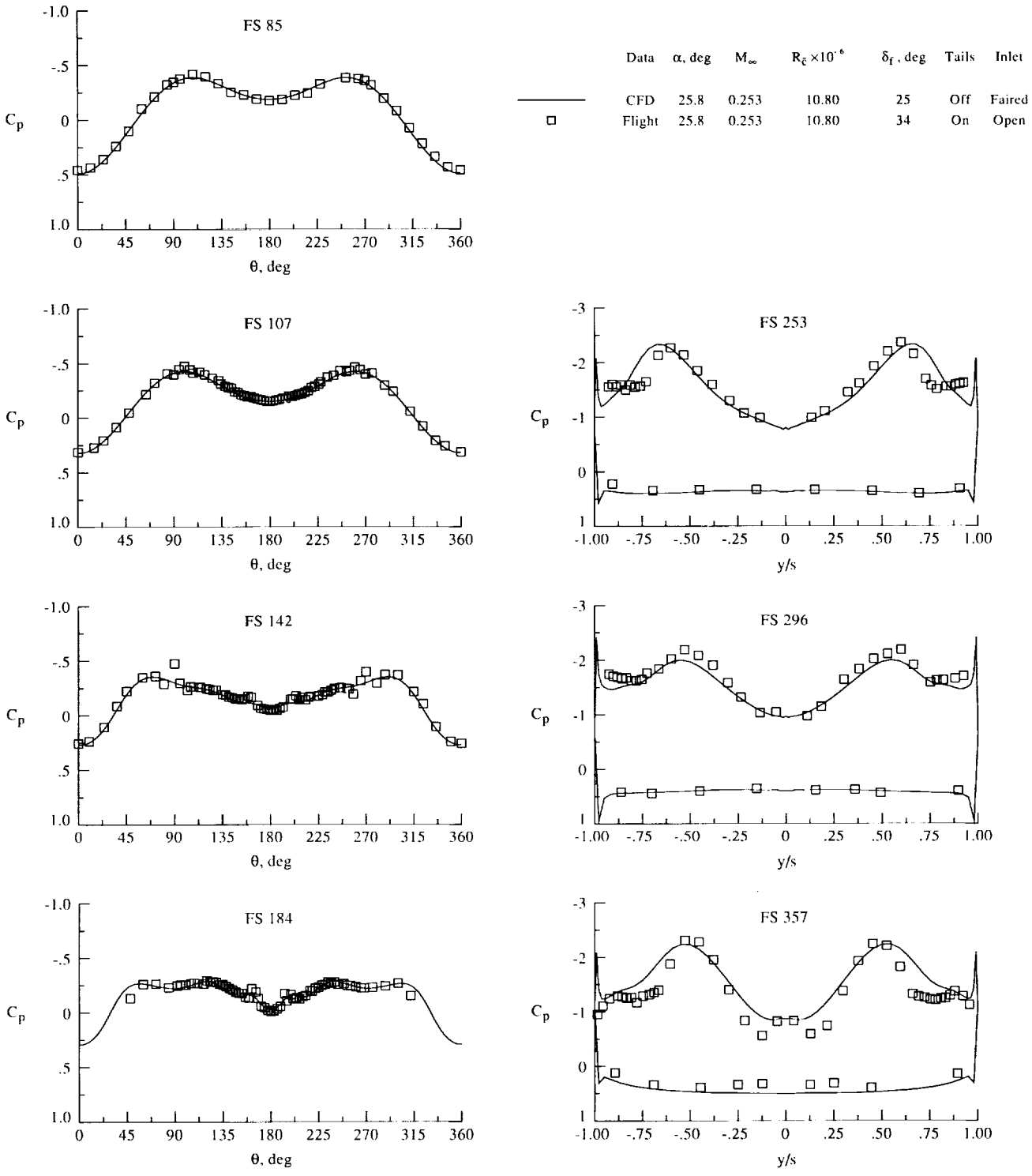

(a) Forebody. (b) LEX.

Figure 20. Correlation of computed surface pressure coefficients with flight data at $\alpha = 25.8°$.

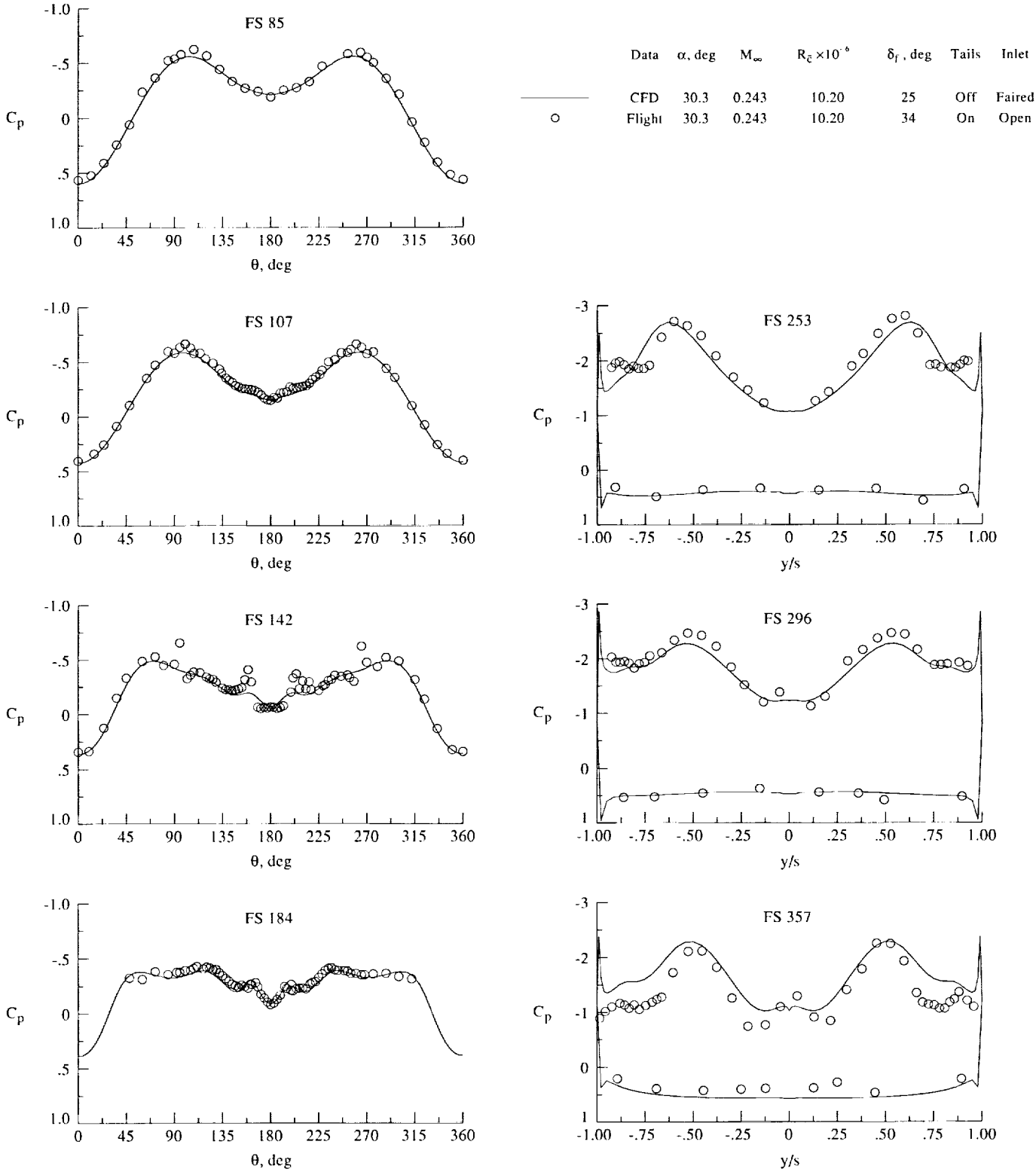

(a) Forebody. (b) LEX.

Figure 21. Correlation of computed surface pressure coefficients with flight data at $\alpha = 30.3°$.

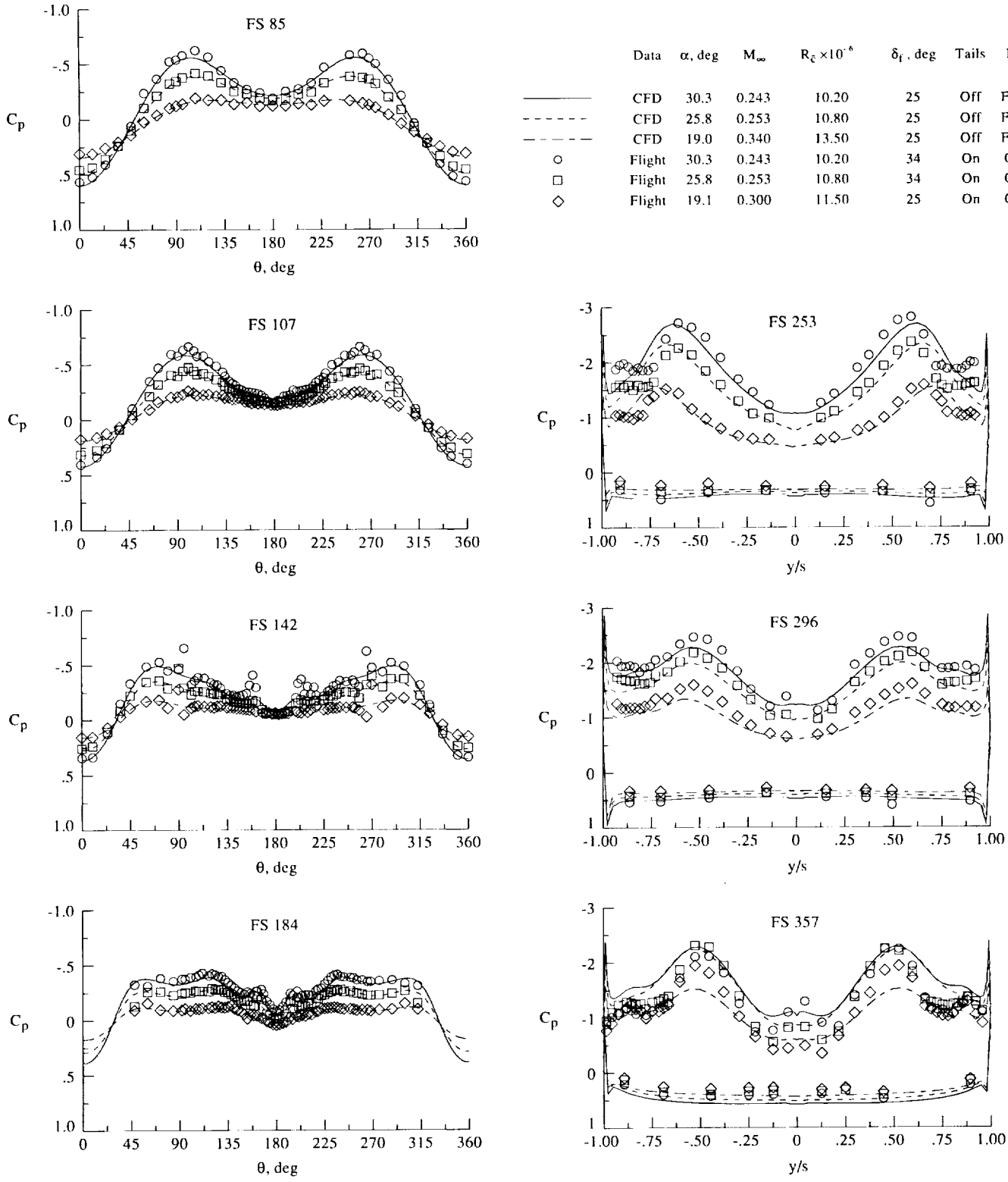

(a) Forebody. (b) LEX.

Figure 22. Effect of angle of attack on computed and measured surface pressure coefficients.

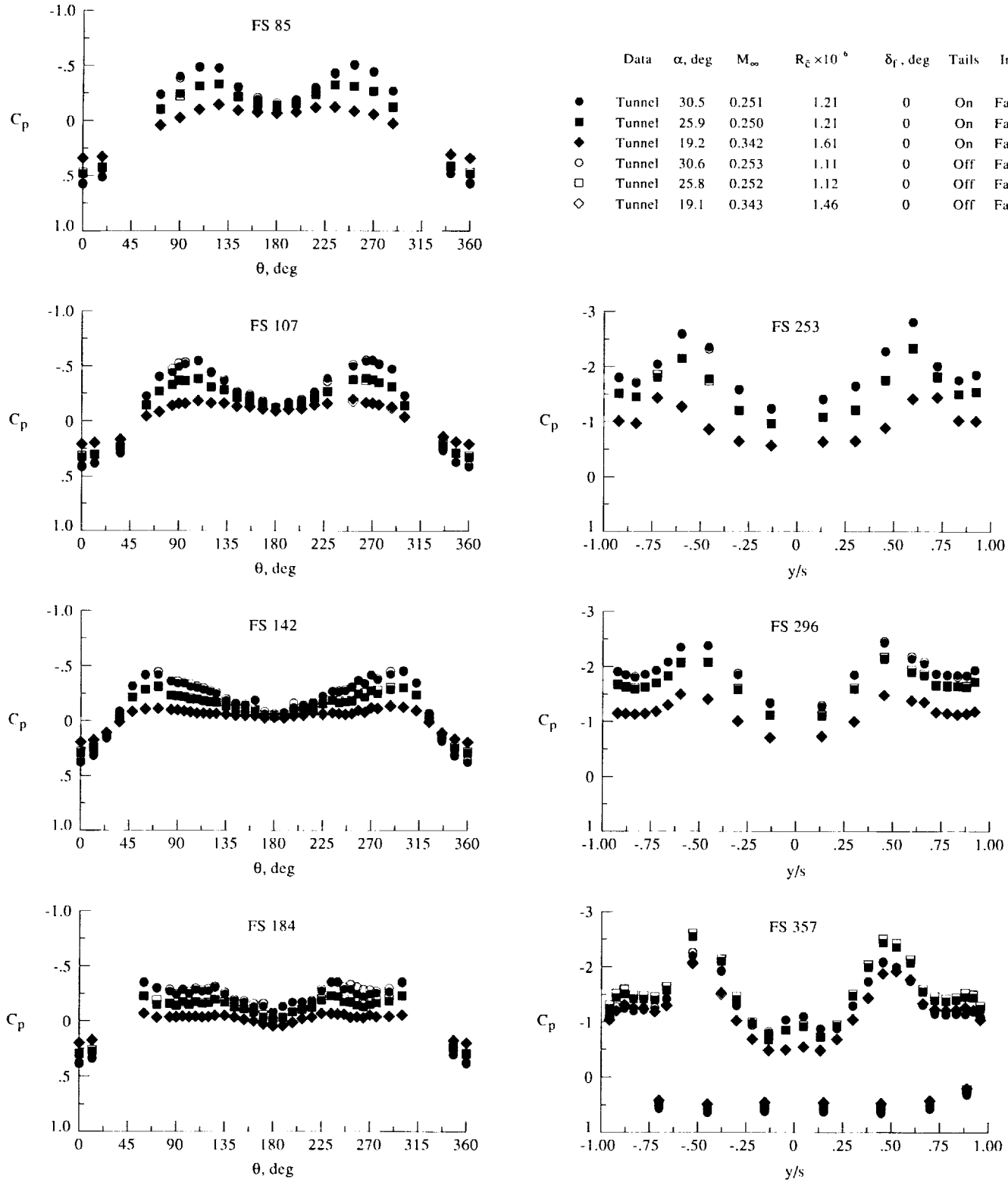

(a) Forebody. (b) LEX.

Figure 23. Effect of empennage on measured forebody and LEX surface pressure coefficients at various values of α with $\delta_f = 0°$.

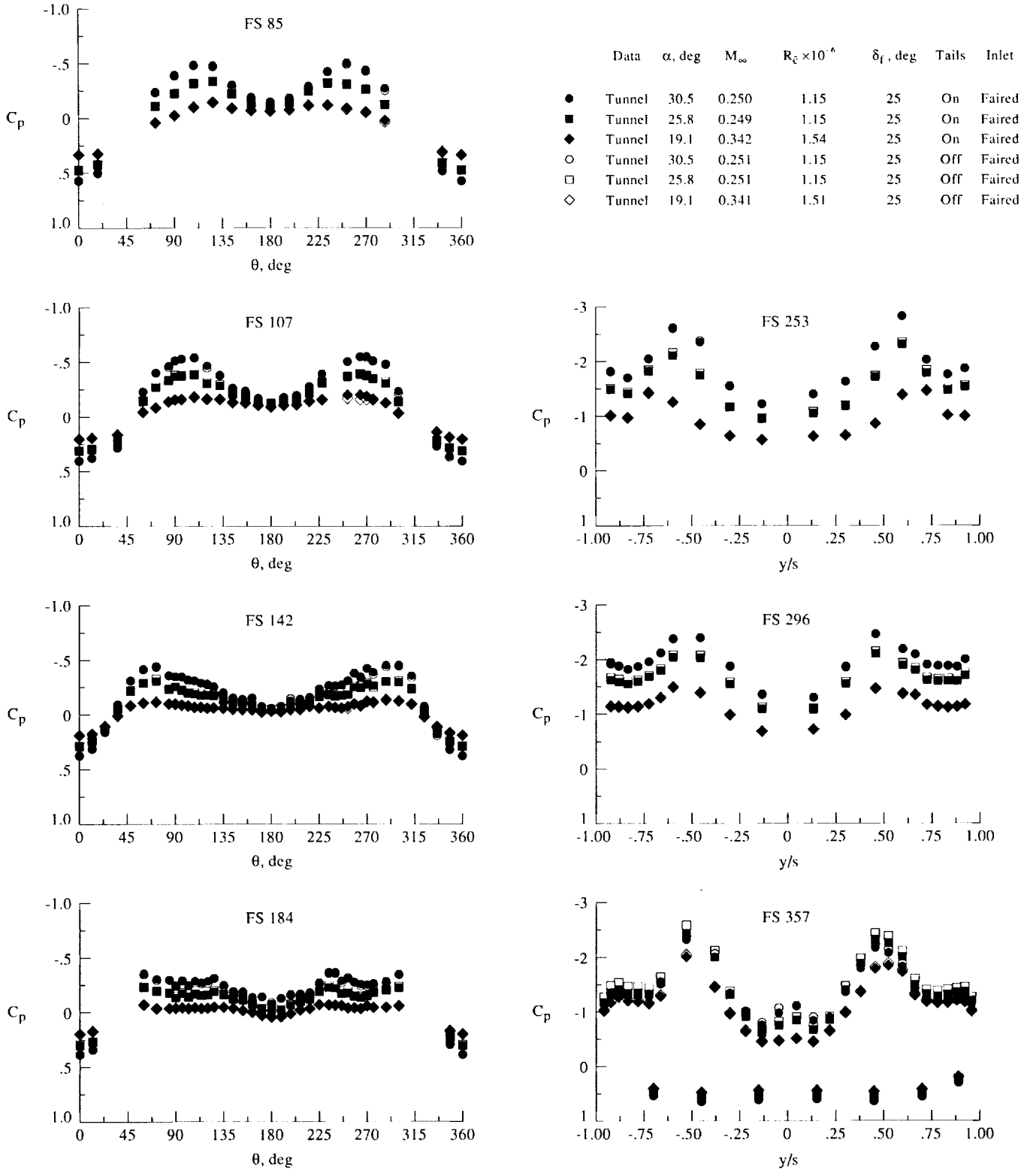

(a) Forebody. (b) LEX.

Figure 24. Effect of empennage on measured forebody and LEX surface pressure coefficients at various values of α with $\delta_f = 25°$.

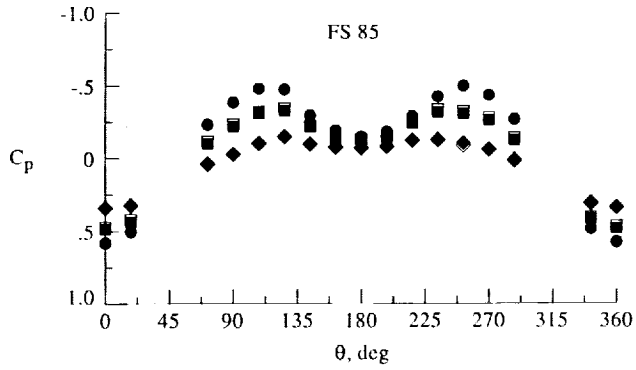

Data		α, deg	M_∞	$R_{\bar{c}} \times 10^{-6}$	δ_f, deg	Tails	Inlet
●	Tunnel	30.6	0.251	1.18	34	On	Faired
■	Tunnel	25.8	0.250	1.17	34	On	Faired
◆	Tunnel	19.2	0.341	1.54	34	On	Faired
○	Tunnel	30.5	0.250	1.21	34	Off	Faired
□	Tunnel	25.8	0.251	1.22	34	Off	Faired
◇	Tunnel	19.1	0.340	1.59	34	Off	Faired

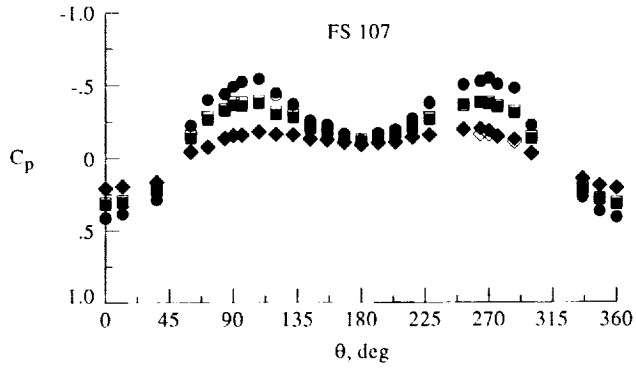

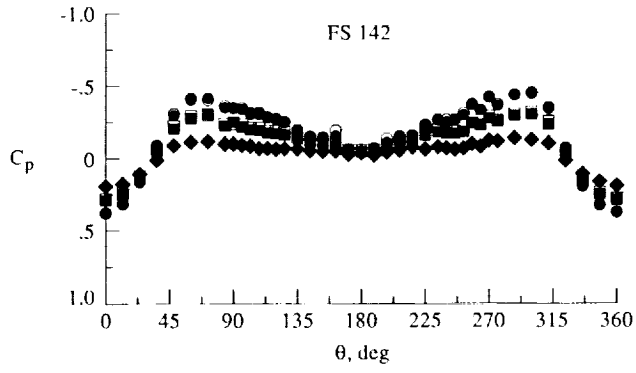

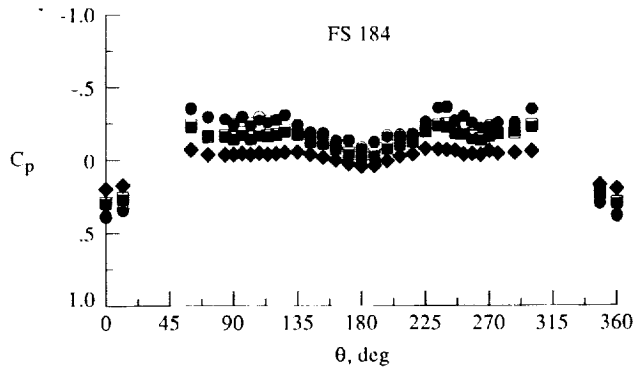

(a) Forebody.

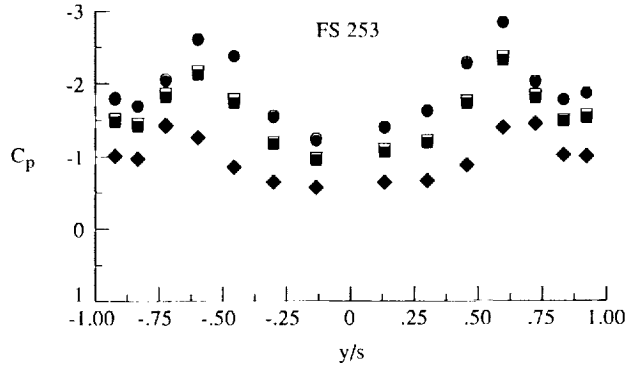

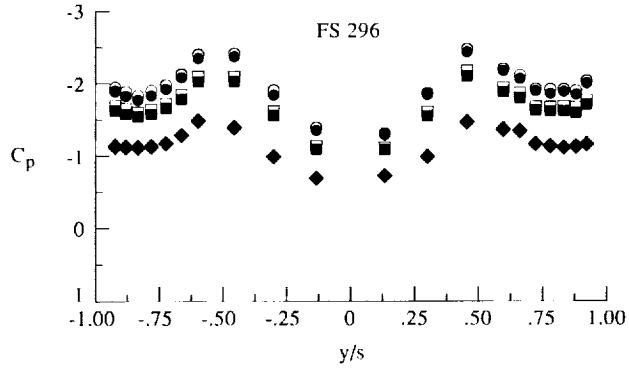

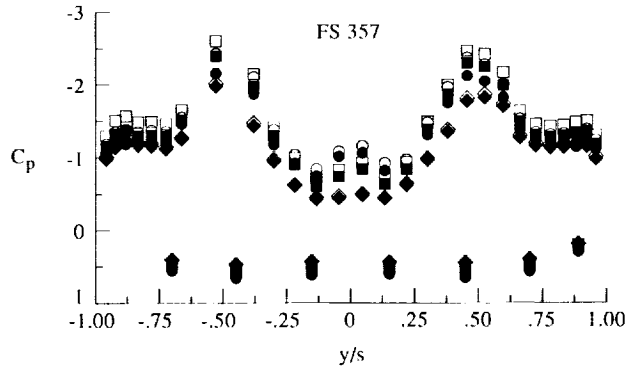

(b) LEX.

Figure 25. Effect of empennage on measured forebody and LEX surface pressure coefficients at various values of α with $\delta_f = 34°$.

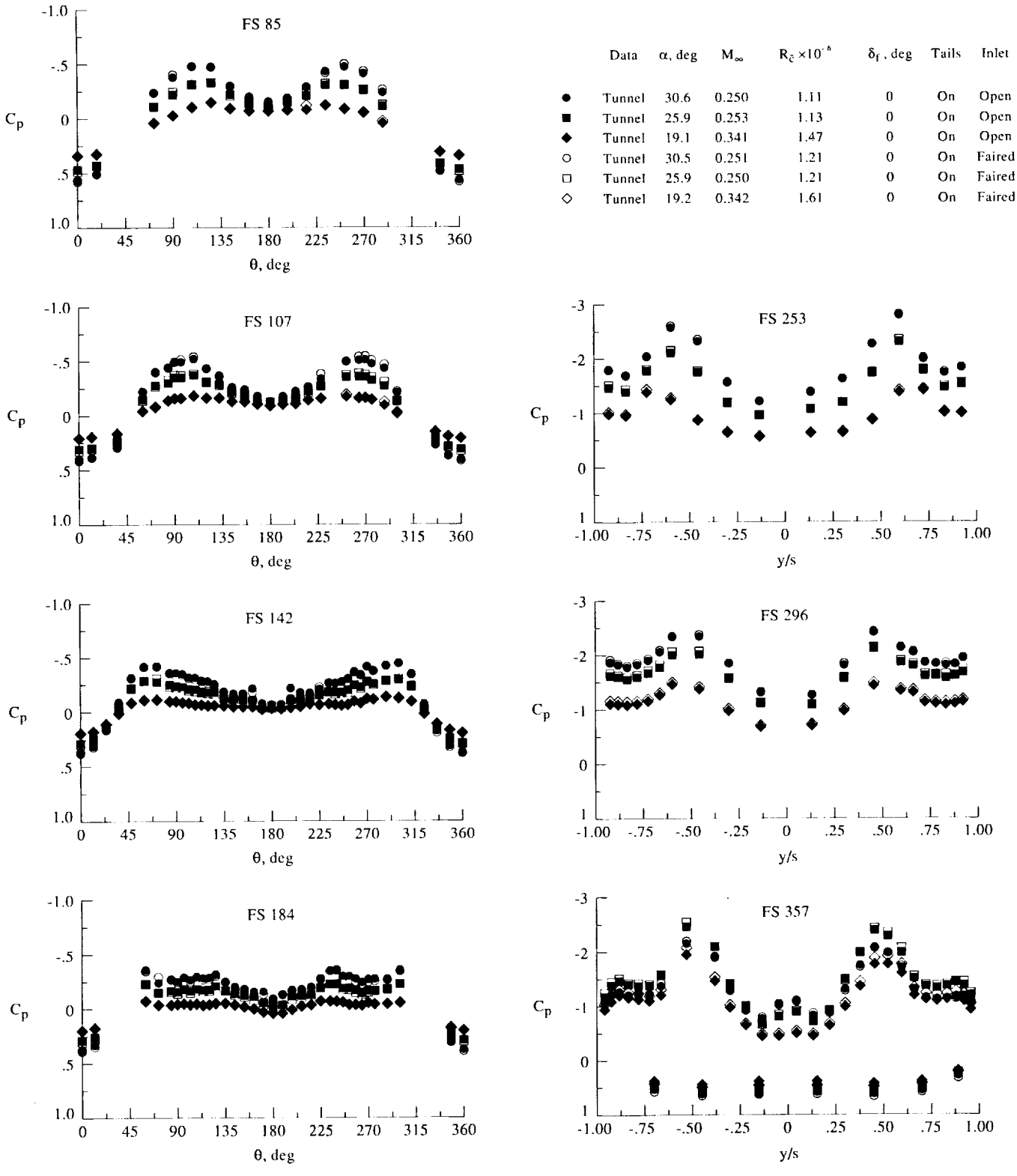

(a) Forebody. (b) LEX.

Figure 26. Effect of inlet fairing on measured forebody and LEX surface pressure coefficients at various values of α with $\delta_f = 0°$.

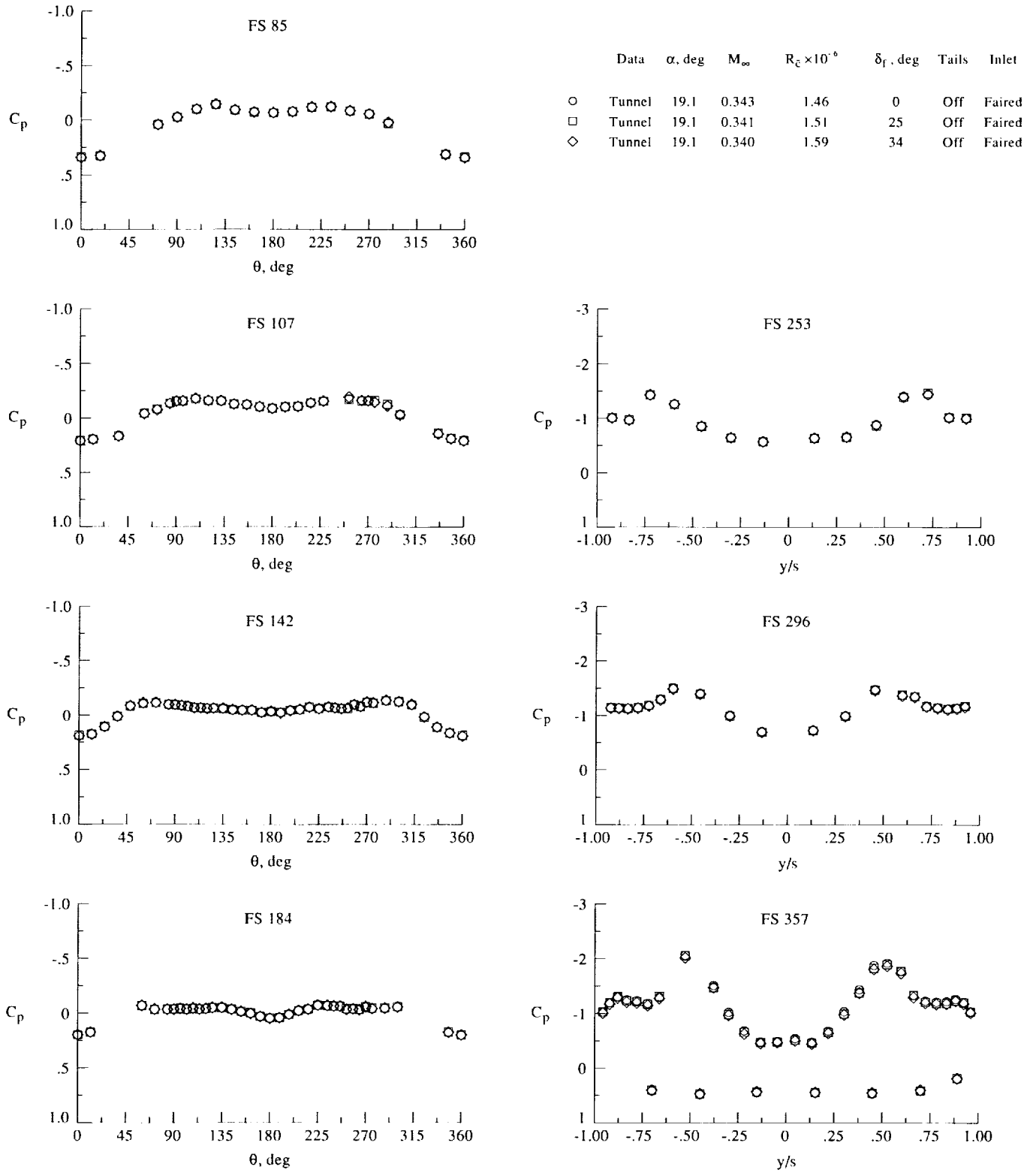

(a) Forebody. (b) LEX.

Figure 27. Effect of wing leading-edge flap deflection on surface pressure coefficients measured on F/A-18 aircraft CFD wind tunnel model at $\alpha \approx 19°$.

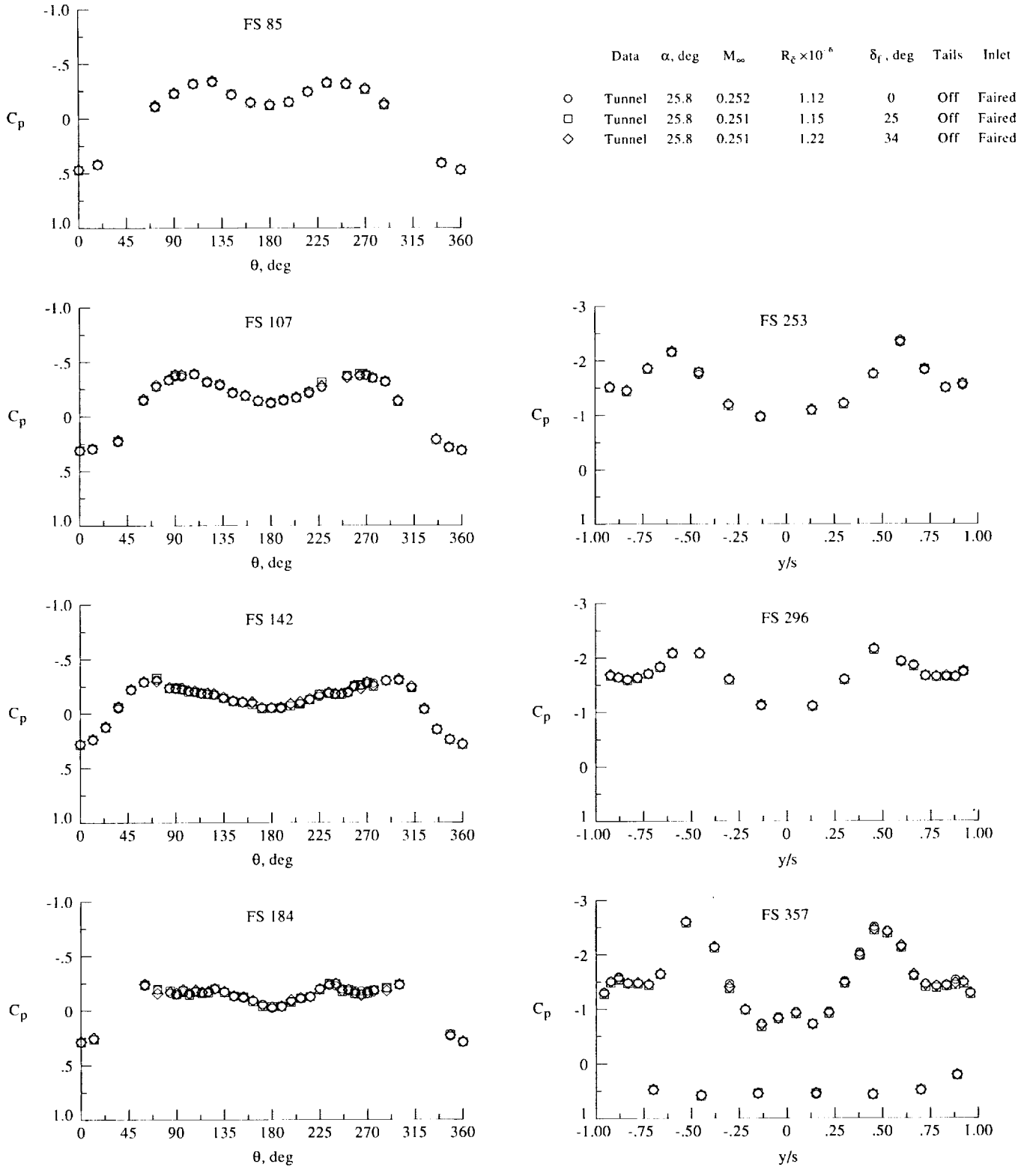

(a) Forebody. (b) LEX.

Figure 28. Effect of wing leading-edge flap deflection on surface pressure coefficients measured on F/A-18 aircraft CFD wind tunnel model at $\alpha \approx 26°$.

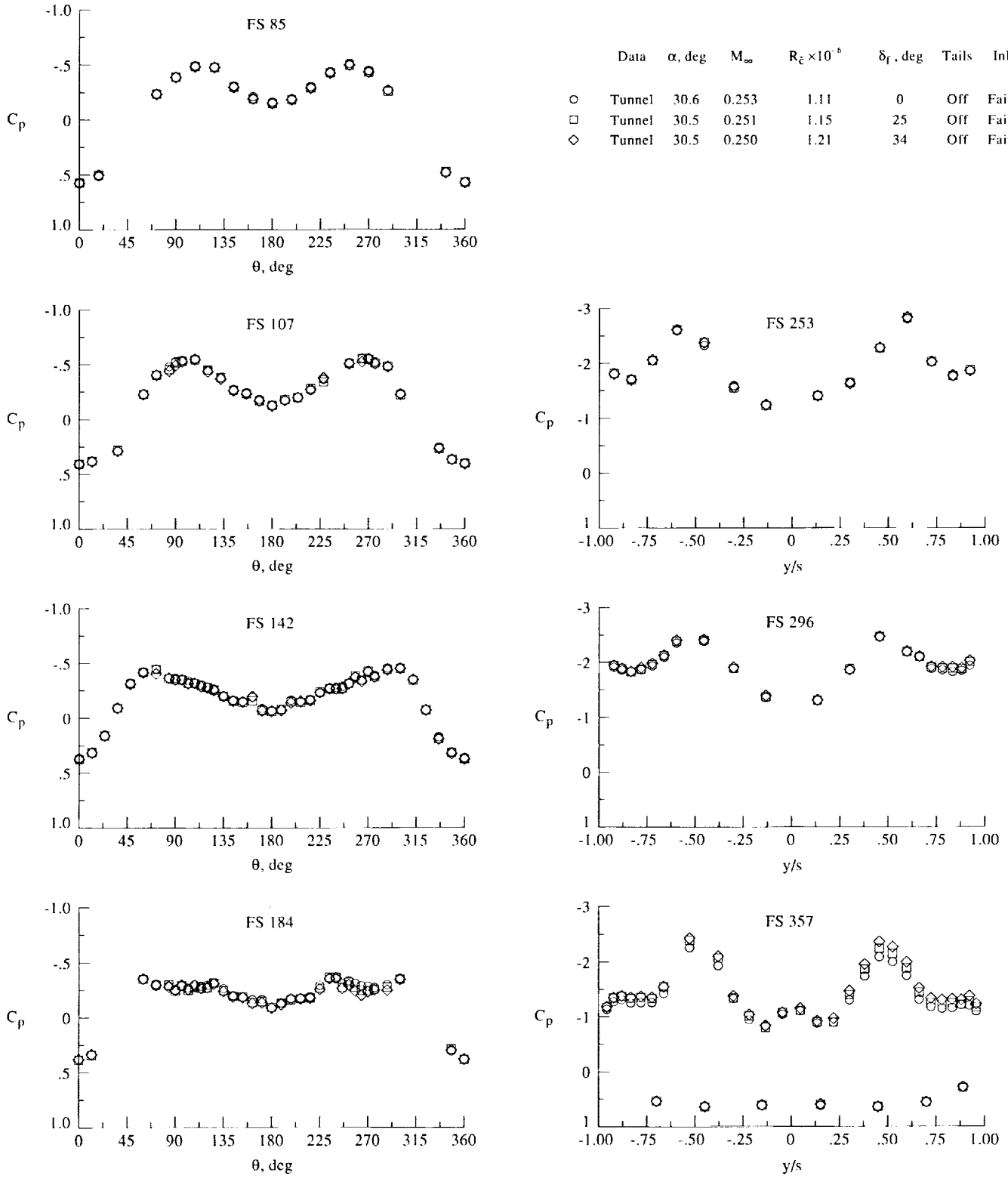

(a) Forebody. (b) LEX.

Figure 29. Effect of wing leading-edge flap deflection on surface pressure coefficients measured on F/A-18 aircraft CFD wind tunnel model at $\alpha \approx 30°$.

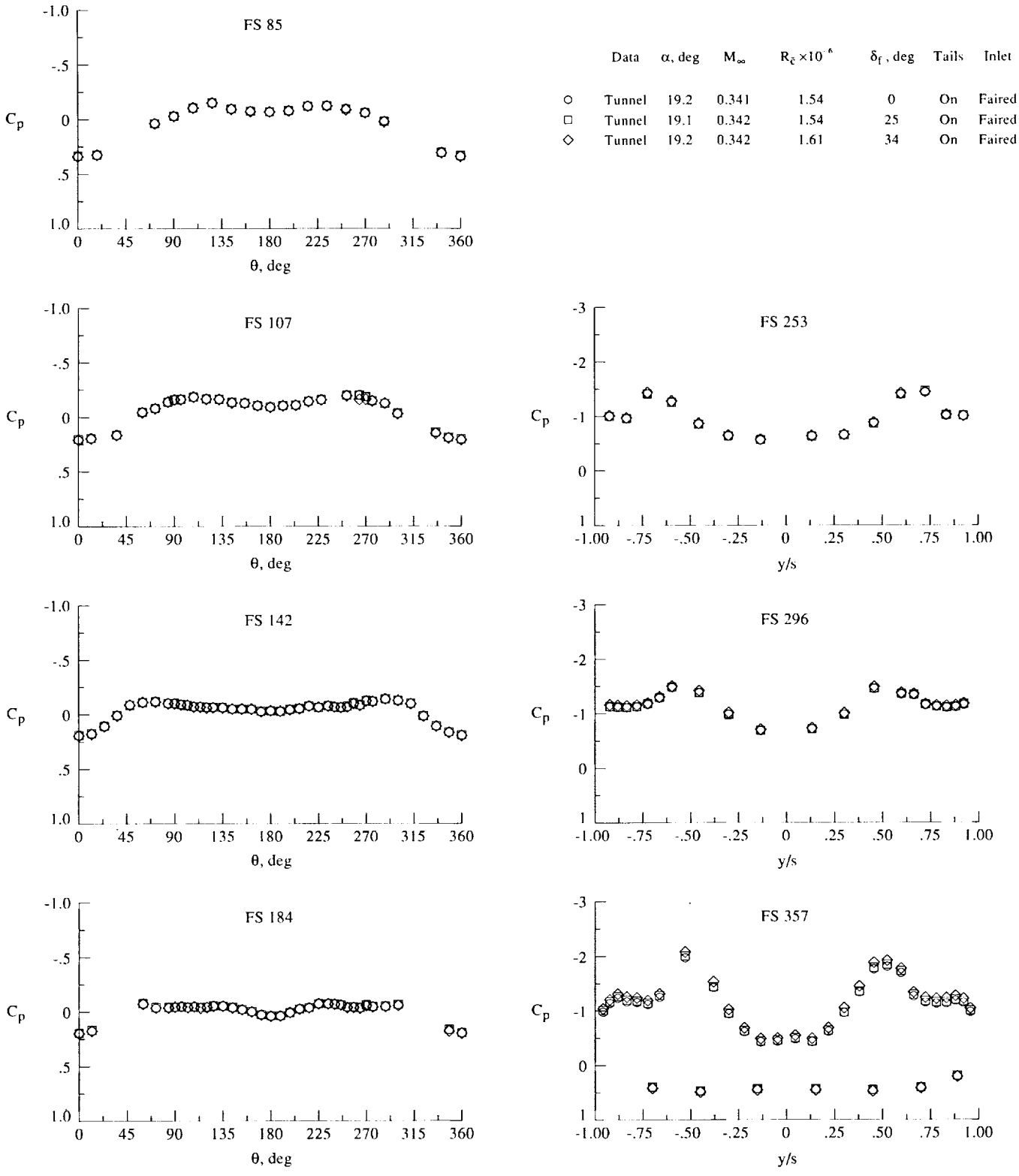

(a) Forebody. (b) LEX.

Figure 30. Effect of wing leading-edge flap deflection on surface pressure coefficients measured on F/A-18 aircraft CFD wind tunnel model with empennage at $\alpha \approx 19°$.

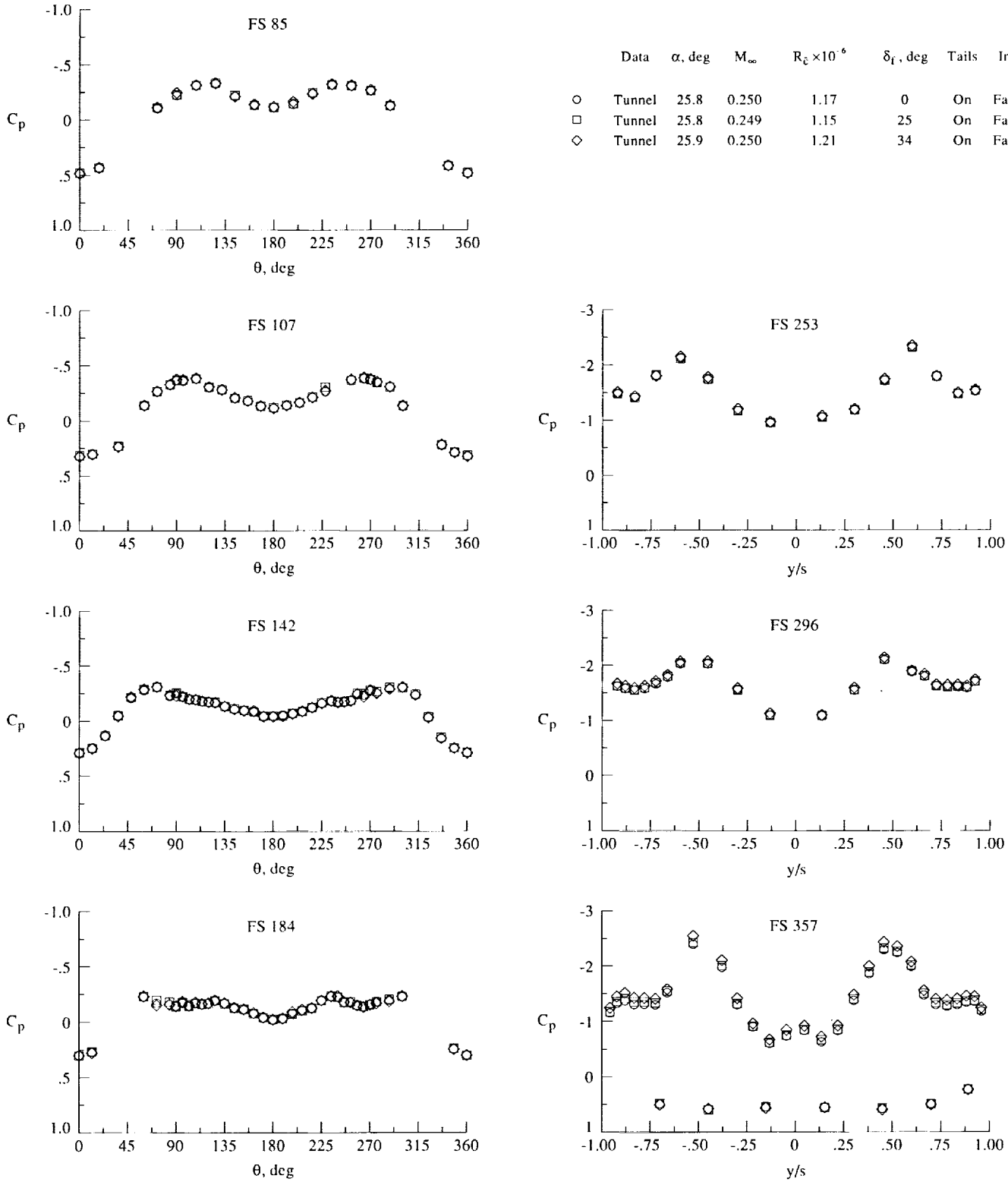

(a) Forebody. (b) LEX.

Figure 31. Effect of wing leading-edge flap deflection on surface pressure coefficients measured on F/A-18 aircraft CFD wind tunnel model with empennage at $\alpha \approx 26°$.

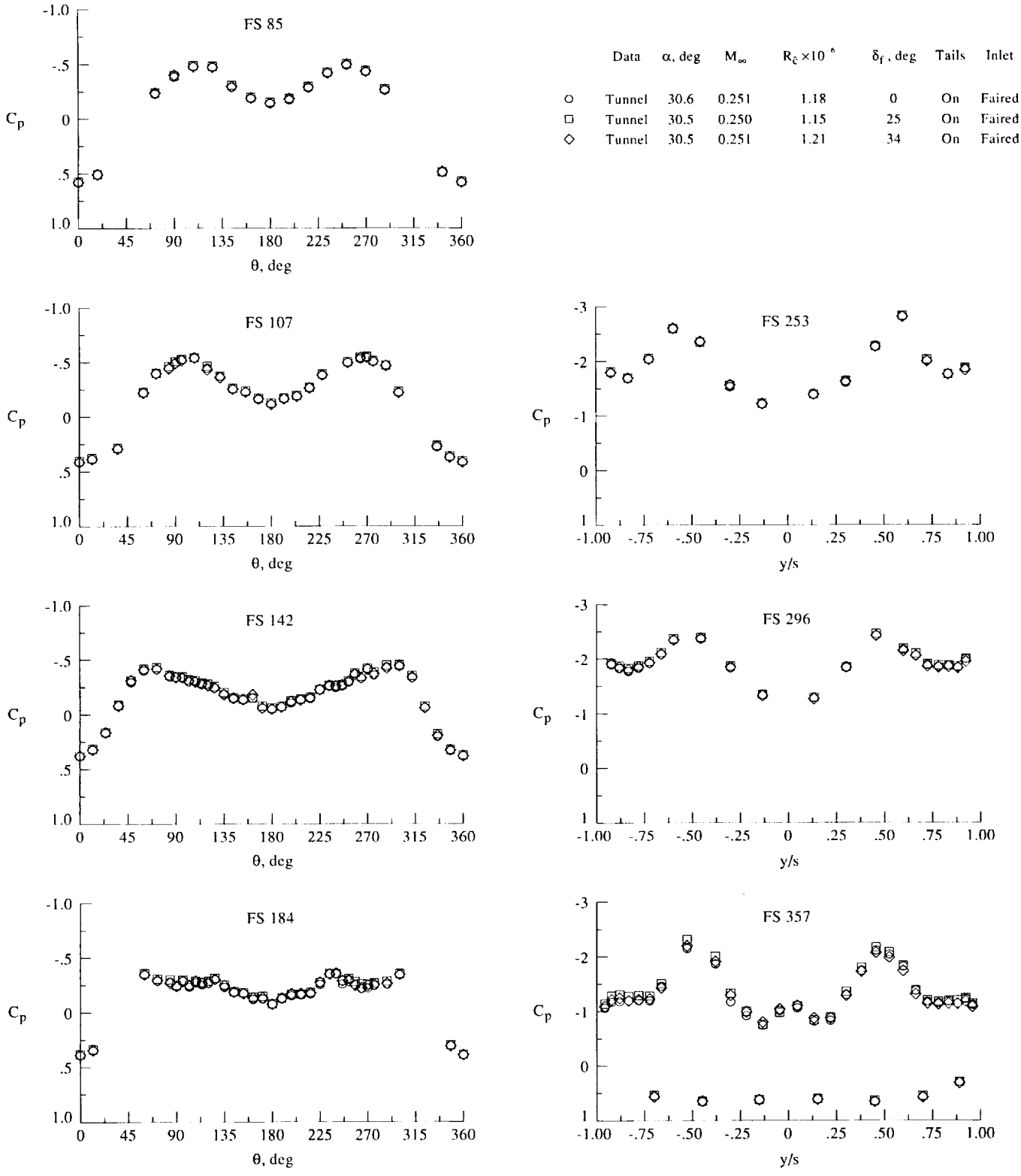

(a) Forebody. (b) LEX.

Figure 32. Effect of wing leading-edge flap deflection on surface pressure coefficients measured on F/A-18 aircraft CFD wind tunnel model with empennage at $\alpha \approx 30°$.

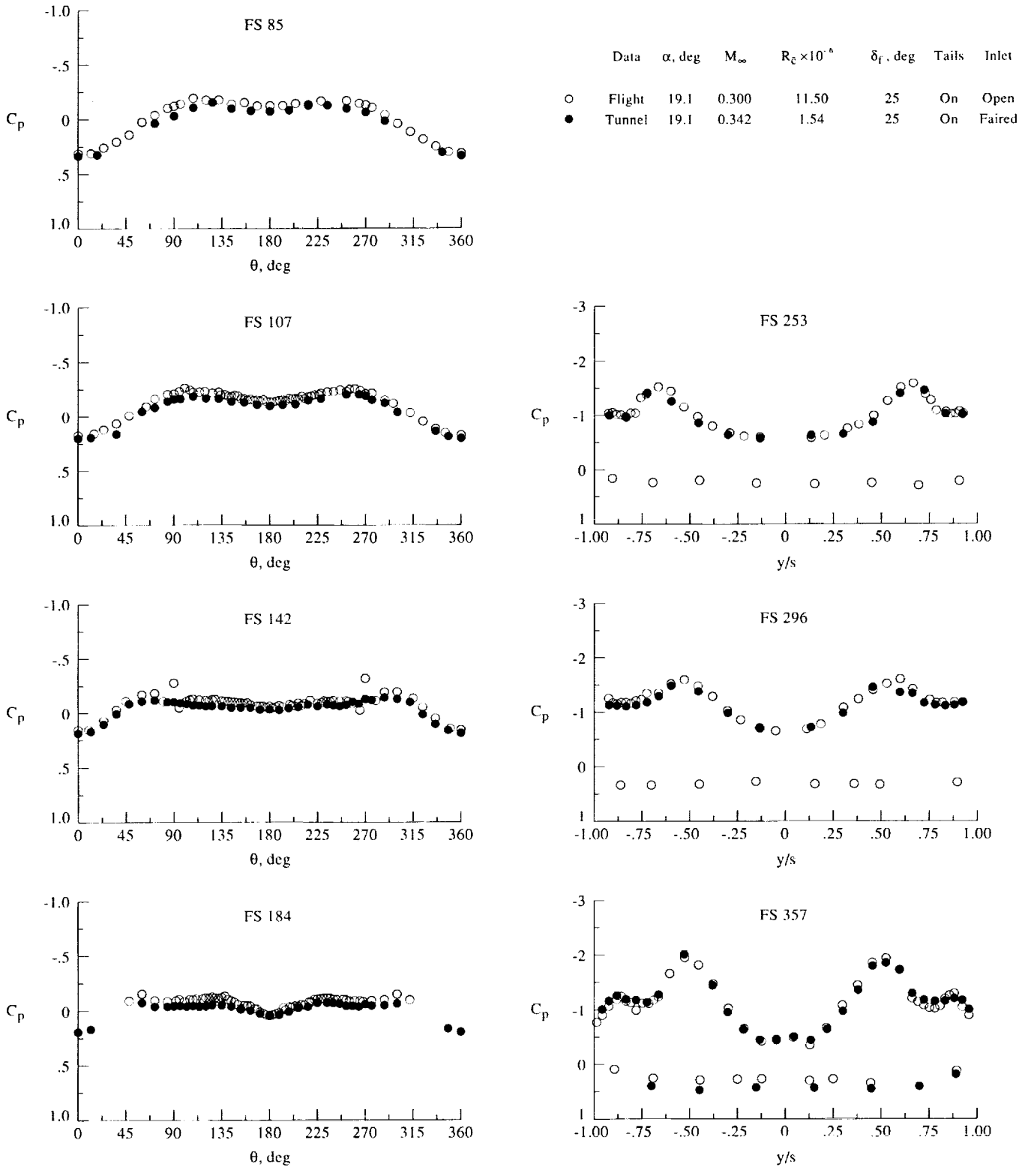

(a) Forebody. (b) LEX.

Figure 33. Correlation of surface pressure coefficients from flight and CFD wind tunnel model tests with empennage at $\alpha \approx 19°$.

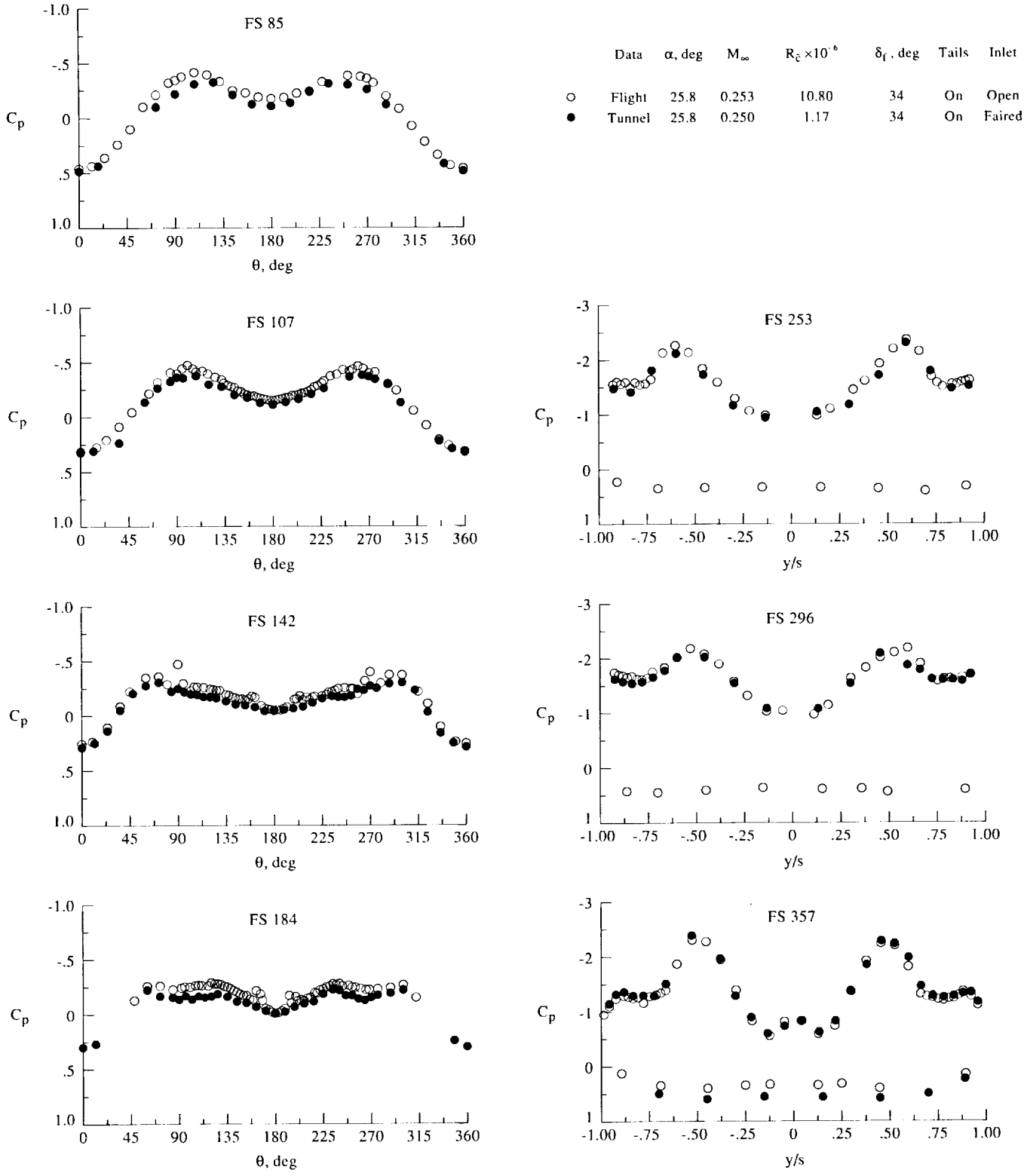

(a) Forebody. (b) LEX.

Figure 34. Correlation of surface pressure coefficients from flight and CFD wind tunnel model tests with empennage at $\alpha \approx 26°$.

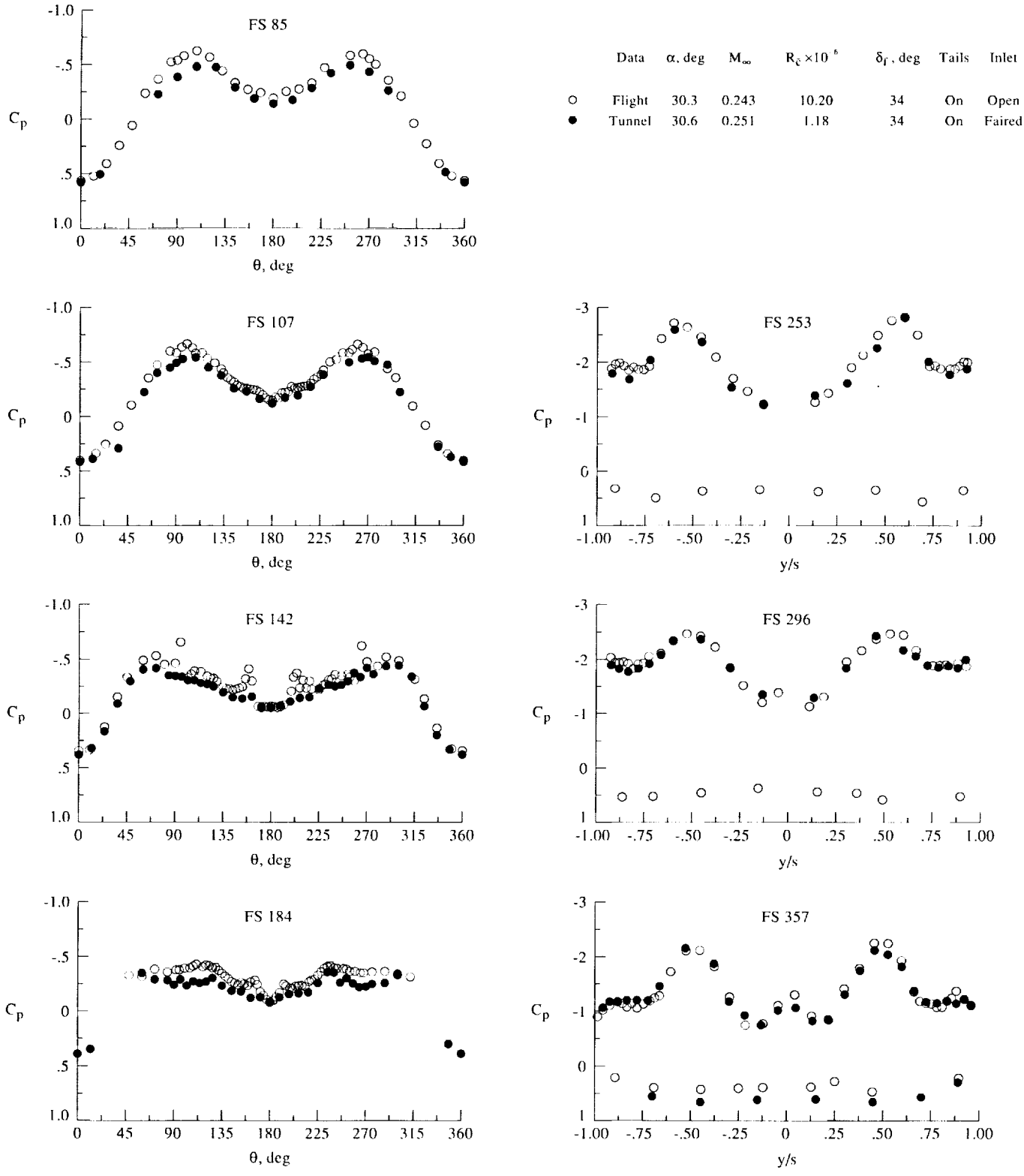

(a) Forebody. (b) LEX.

Figure 35. Correlation of surface pressure coefficients from flight and CFD wind tunnel model tests with empennage at $\alpha \approx 30°$.

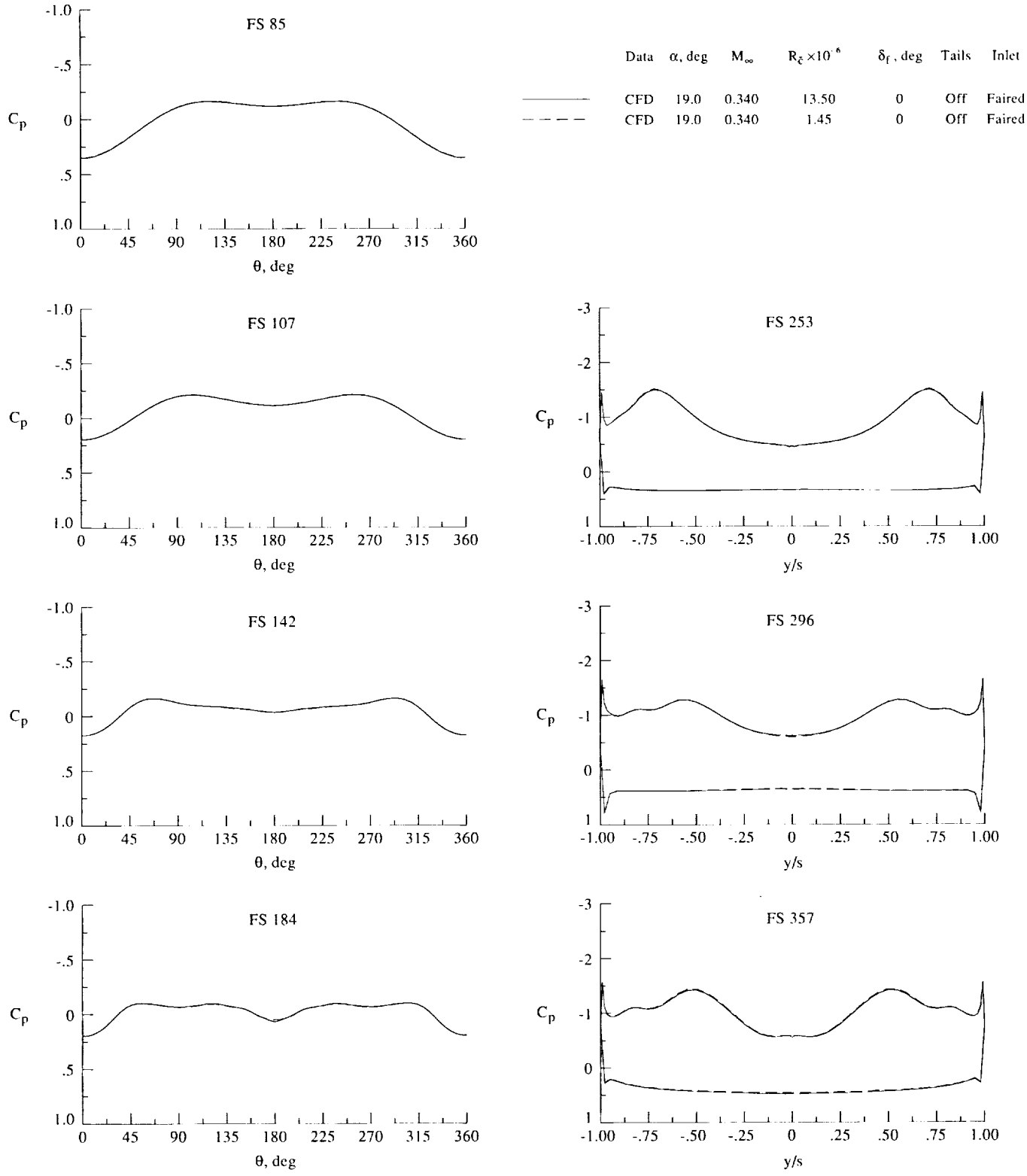

(a) Forebody. (b) LEX.

Figure 36. Effect of Reynolds number on computed surface pressure coefficients at $\alpha \approx 19°$.

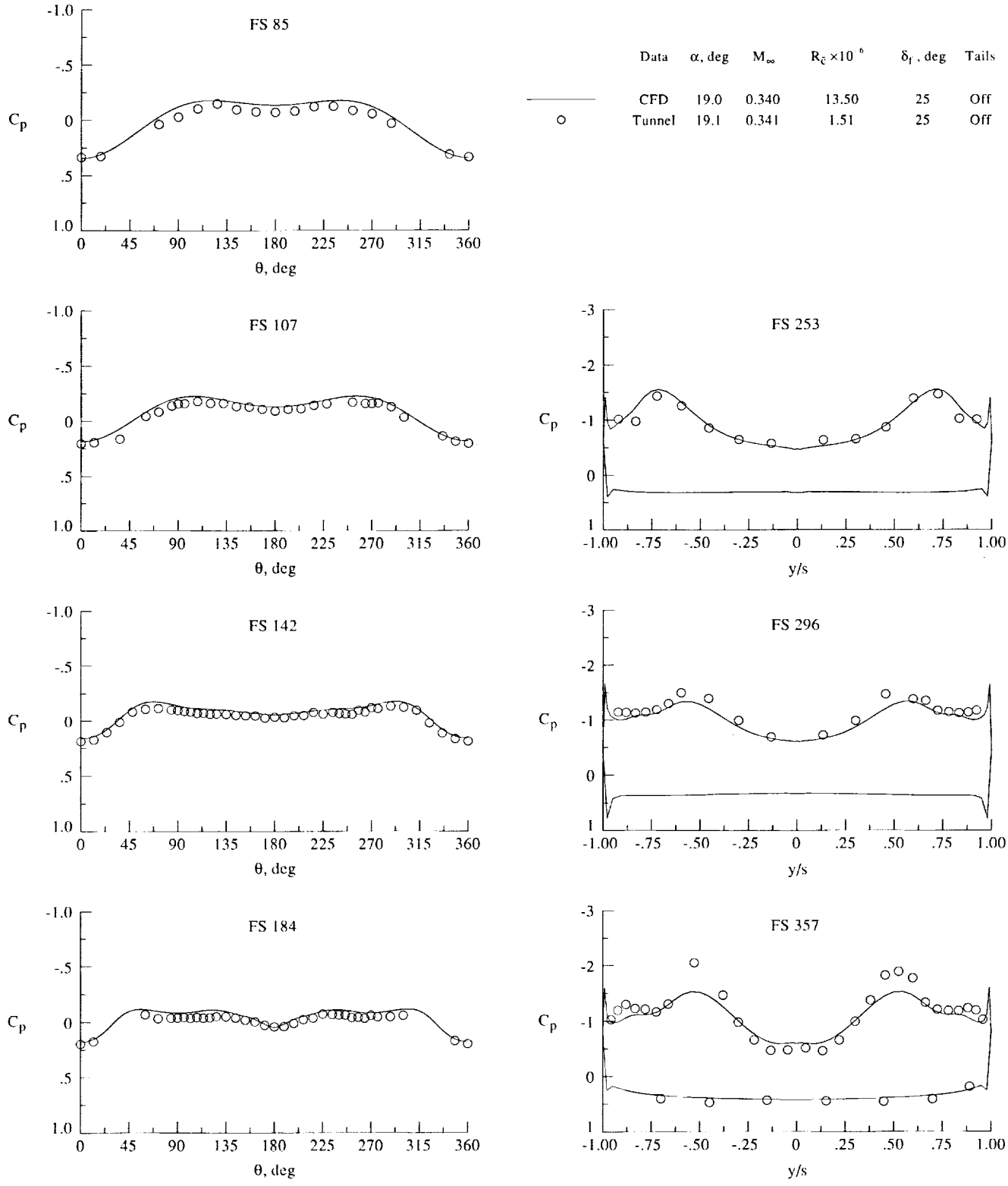

(a) Forebody. (b) LEX.

Figure 37. Correlation of surface pressure coefficients from computed and CFD wind tunnel model tests at $\alpha \approx 19°$.

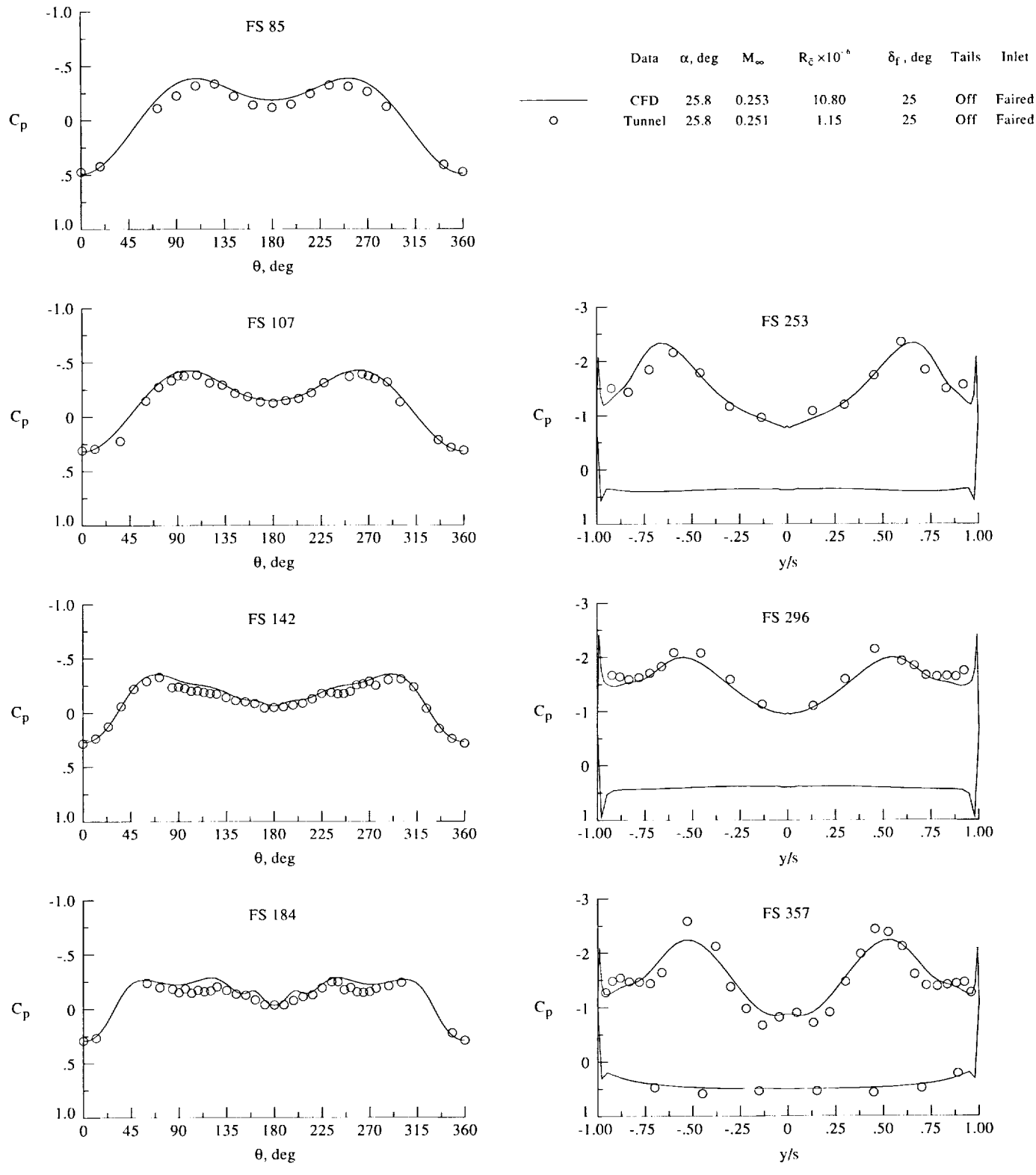

(a) Forebody. (b) LEX.

Figure 38. Correlation of surface pressure coefficients from computed and CFD wind tunnel model tests at $\alpha \approx 26°$.

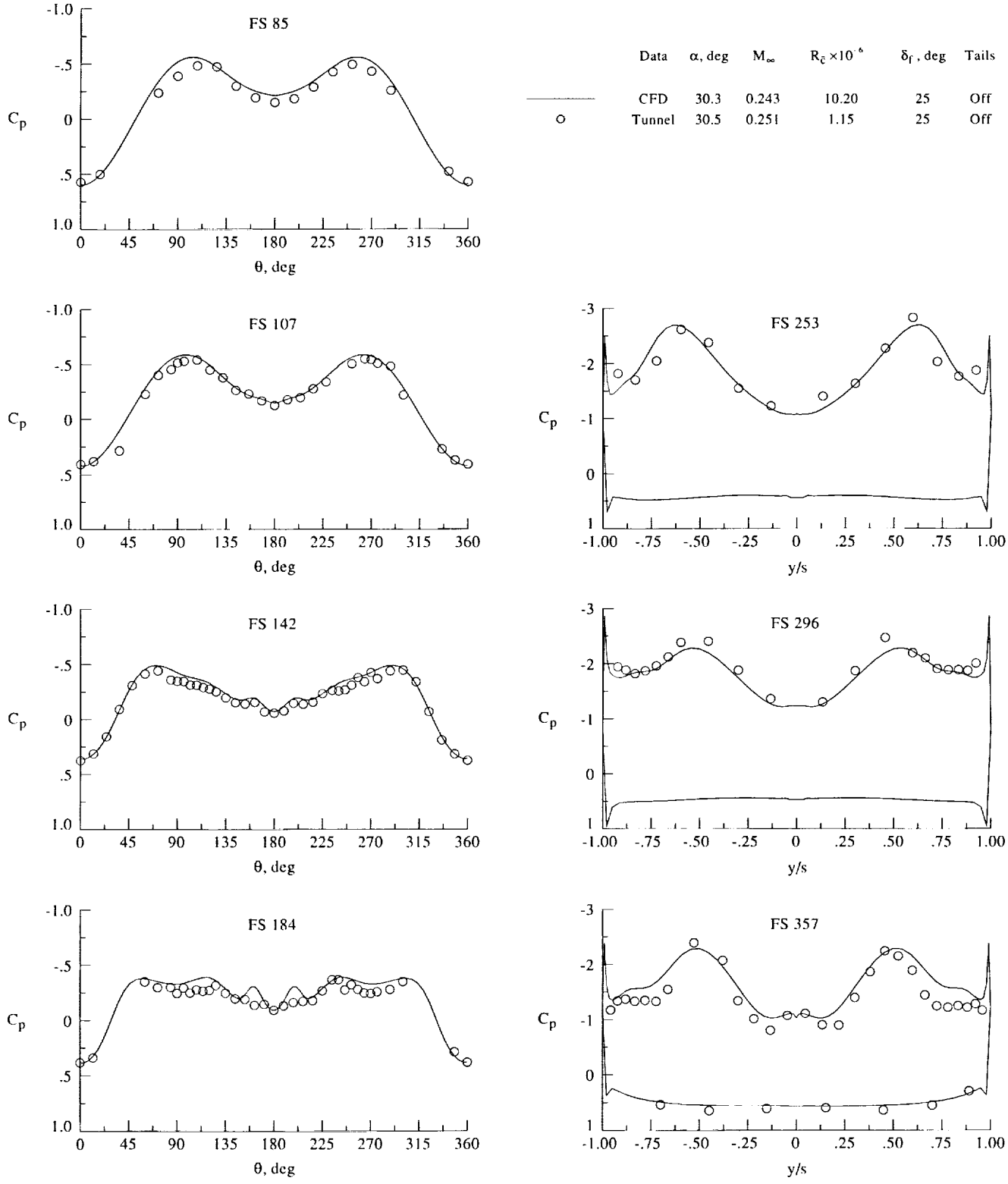

(a) Forebody. (b) LEX.

Figure 39. Correlation of surface pressure coefficients from computed and CFD wind tunnel model tests at $\alpha \approx 30°$.

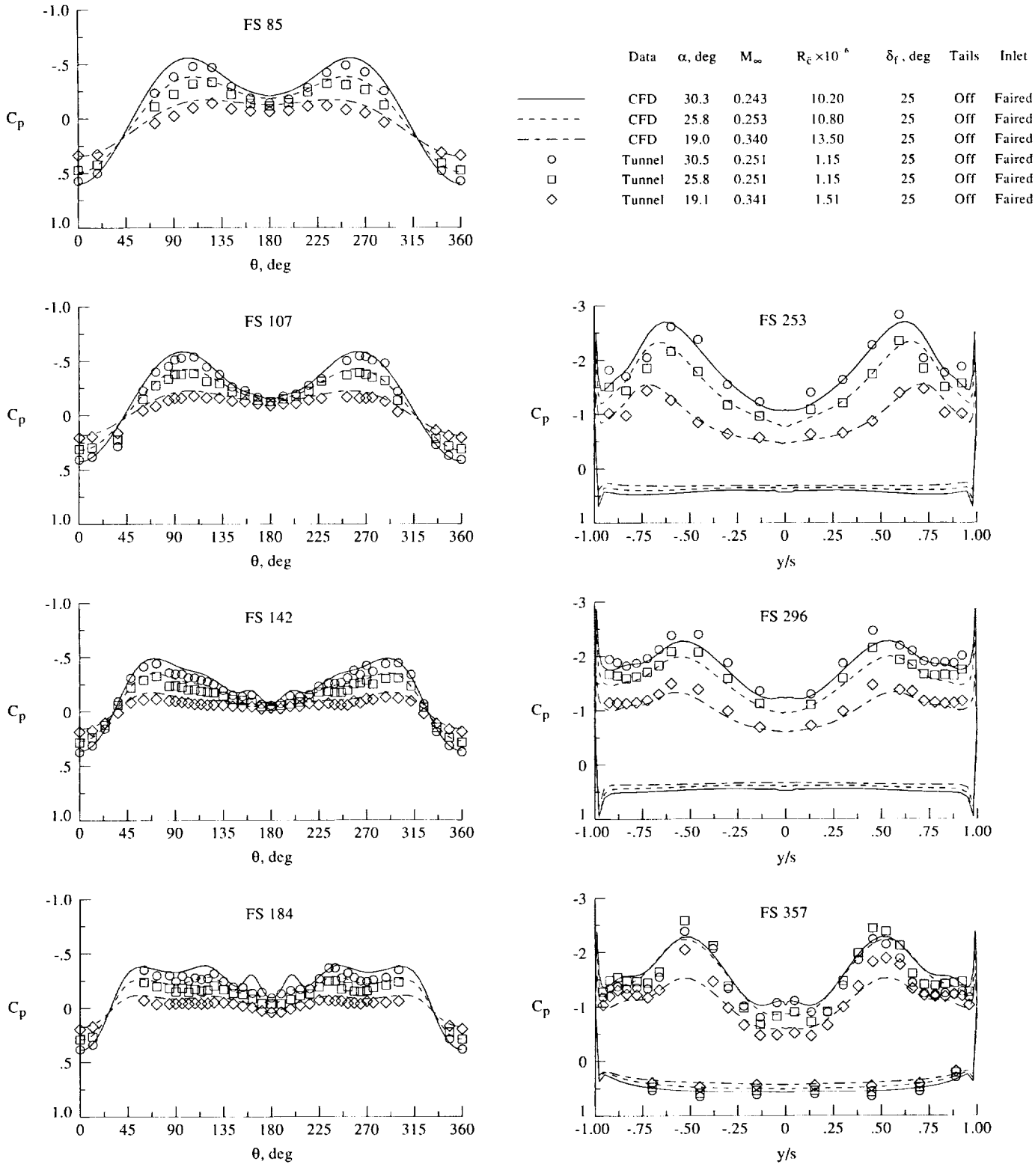

(a) Forebody. (b) LEX.

Figure 40. Effect of angle of attack on computed and measured surface pressure coefficients for CFD wind tunnel model with $\delta_f = 25°$.

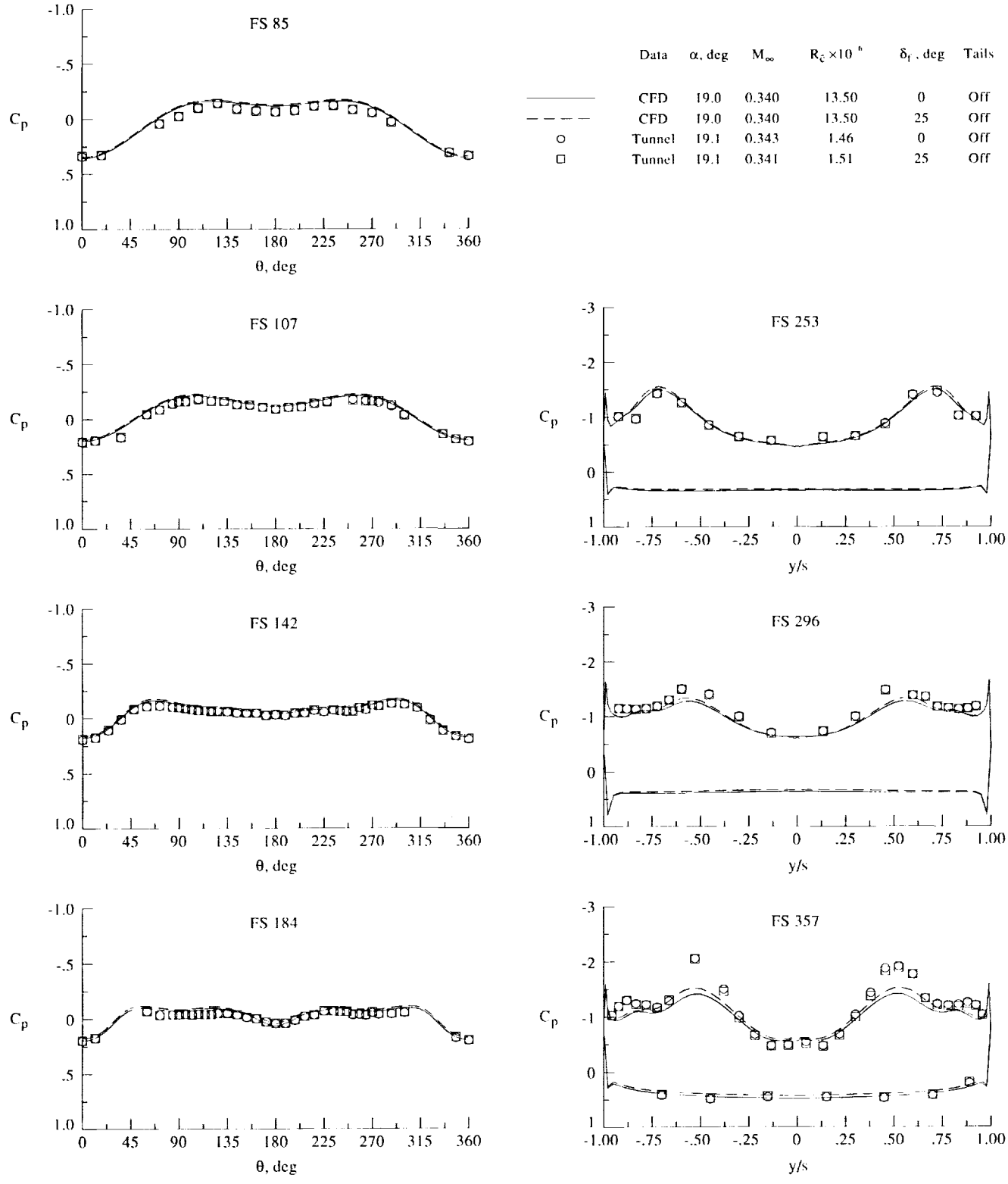

(a) Forebody. (b) LEX.

Figure 41. Effect of wing leading-edge flap deflection on computed and measured surface pressure coefficients for CFD wind tunnel model at $\alpha \approx 19°$.

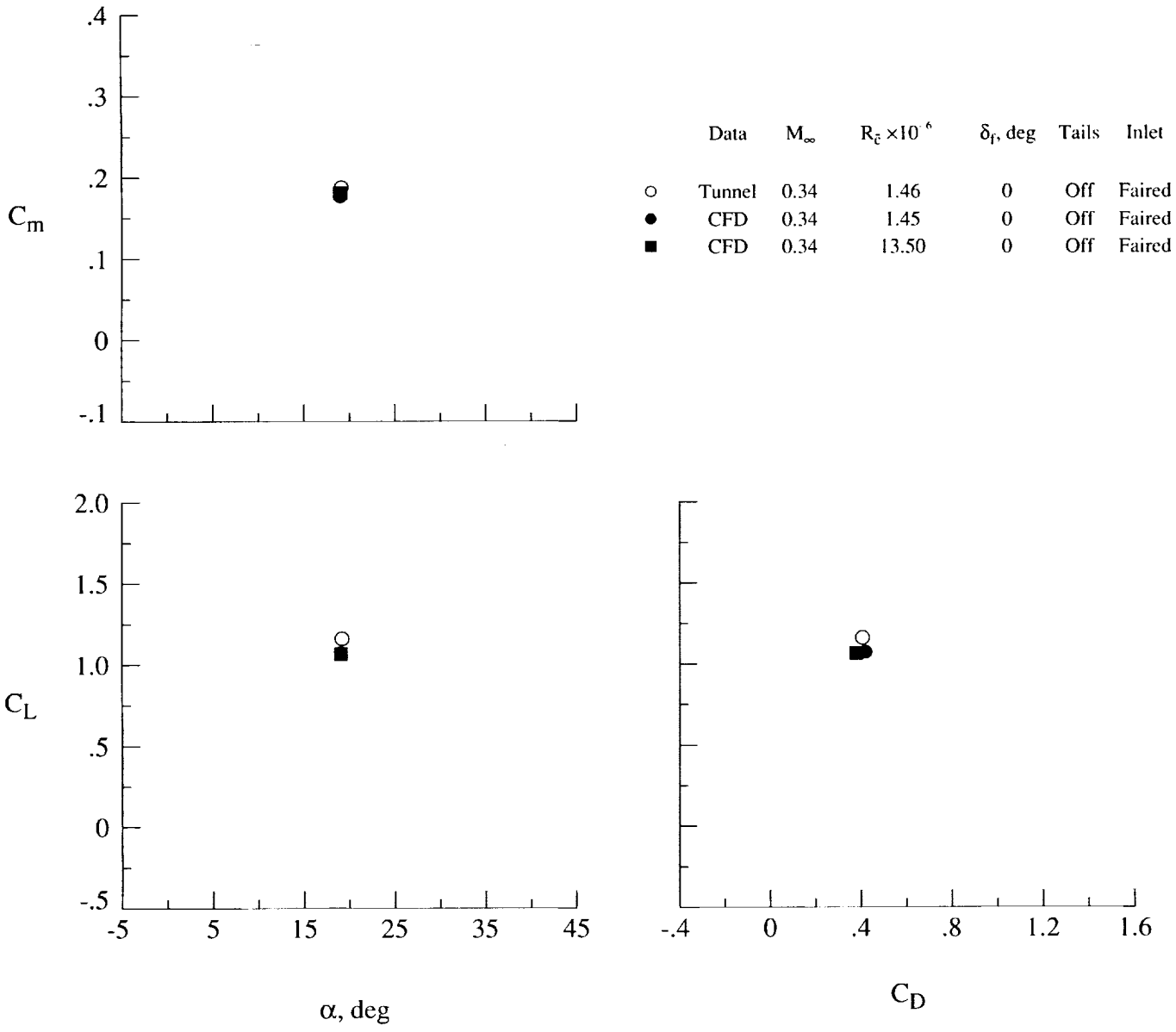

Figure 42. Effect of Reynolds number on computed longitudinal aerodynamic characteristics and correlation with measurements on CFD wind tunnel model at $\alpha \approx 19°$.

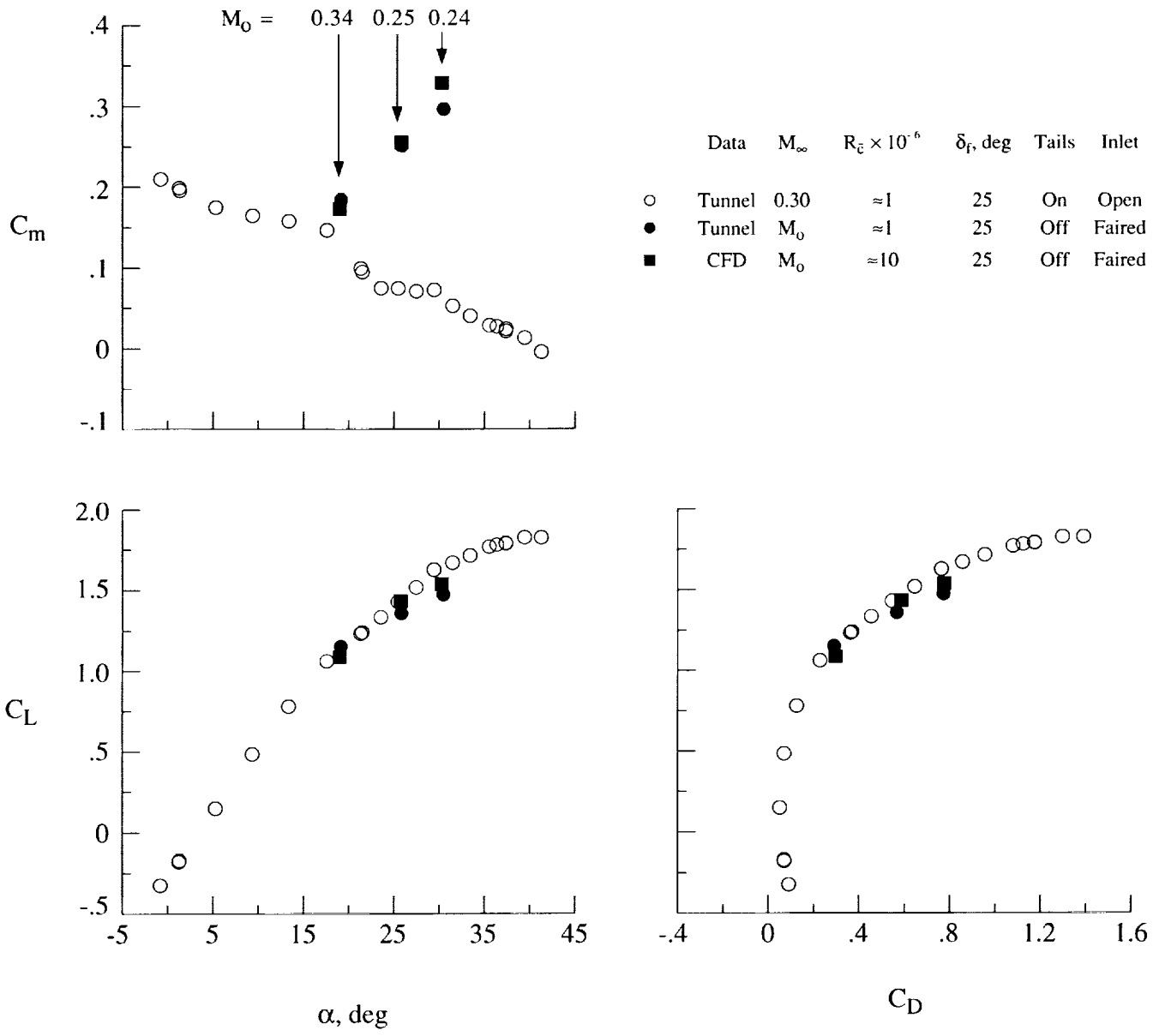

Figure 43. Measured and predicted longitudinal aerodynamic characteristics for baseline F/A-18 aircraft and CFD wind tunnel model.

REPORT DOCUMENTATION PAGE

Form Approved
OMB No. 0704-0188

1. AGENCY USE ONLY *(Leave blank)*	2. REPORT DATE	3. REPORT TYPE AND DATES COVERED
	December 1994	Technical Paper

4. TITLE AND SUBTITLE
Navier-Stokes, Flight, and Wind Tunnel Flow Analysis for the F/A-18 Aircraft

5. FUNDING NUMBERS
WU 505-68-30-03

6. AUTHOR(S)
Farhad Ghaffari

7. PERFORMING ORGANIZATION NAME(S) AND ADDRESS(ES)
NASA Langley Research Center
Hampton, VA 23681-0001

8. PERFORMING ORGANIZATION REPORT NUMBER
L-17336

9. SPONSORING/MONITORING AGENCY NAME(S) AND ADDRESS(ES)
National Aeronautics and Space Administration
Washington, DC 20546-0001

10. SPONSORING/MONITORING AGENCY REPORT NUMBER
NASA TP-3478

11. SUPPLEMENTARY NOTES

12a. DISTRIBUTION/AVAILABILITY STATEMENT
Unclassified Unlimited
Subject Category 02
Availability: NASA CASI (301) 621-0390

12b. DISTRIBUTION CODE

13. ABSTRACT *(Maximum 200 words)*

Computational analysis of flow over the F/A-18 aircraft is presented along with complementary data from both flight and wind tunnel experiments. The computational results are based on the three-dimensional thin-layer Navier-Stokes formulation and are obtained from an accurate surface representation of the fuselage, leading-edge extension (LEX), and the wing geometry. However, the constraints imposed by either the flow solver and/or the complexity associated with the flow-field grid generation required certain geometrical approximations to be implemented in the present numerical model. In particular, such constraints inspired the removal of the empennage and the blocking (fairing) of the inlet face. The results are computed for three different free-stream flow conditions and compared with flight test data of surface pressure coefficients, surface tuft flow, and off-surface vortical flow characteristics that included breakdown phenomena. Excellent surface pressure coefficient correlations, both in terms of magnitude and overall trend, are obtained on the forebody throughout the range of flow conditions. Reasonable pressure agreement was obtained over the LEX; the general correlation tends to improve at higher angles of attack. The surface tuft flow and the off-surface vortex flow structures compared qualitatively well with the flight test results. To evaluate the computational results, a wind tunnel investigation was conducted to determine the effects of existing configurational differences between the flight vehicle and the numerical model on aerodynamic characteristics. In most cases, the geometrical approximations made to the numerical model had very little effect on overall aerodynamic characteristics.

14. SUBJECT TERMS
F/A-18 aircraft; Computational fluid dynamics; Navier-Stokes analysis; Flight data; Wind tunnel data; High angles of attack; Vortical flows; Vortex breakdown

15. NUMBER OF PAGES
65

16. PRICE CODE
A04

17. SECURITY CLASSIFICATION OF REPORT	18. SECURITY CLASSIFICATION OF THIS PAGE	19. SECURITY CLASSIFICATION OF ABSTRACT	20. LIMITATION OF ABSTRACT
Unclassified	Unclassified	Unclassified	